DISORDER AND NANOPATTERNING IN ORDERED BINARY ALLOYS: *IN SITU* ION IRRADIATION AND KINETIC MONTE CARLO SIMULATION

BY

CALVIN ROBERT LEAR

DISSERTATION

Submitted in partial fulfillment of the requirements
for the degree of Doctor of Philosophy in Materials Science and Engineering
in the Graduate College of the
University of Illinois at Urbana-Champaign, 2016

Urbana, Illinois

Doctoral Committee:

Professor Robert S. Averback, Co-Chair
Professor Pascal Bellon, Co-Chair
Professor Jian-Min Zuo
Assistant Professor Robert Maass
Assistant Professor Yang Zhang

ABSTRACT

We study the effects of temperature and disordering rate on the ordered microstructures of real and simulated binary alloys. The behavior of Cu_3Au, an alloy with $L1_2$ chemical order, is investigated experimentally through *in situ* electron diffraction and dark-field transmission electron microscopy. Under irradiation with 500 keV Ne^+ ions, our diffraction analysis reveals a similar, but steeper, trend in disordering rate as previously reported by resistivity. Further investigations by superlattice, dark-field imaging lead to the discovery of temperature and dose rate dependent alterations to the ordered microstructure of the alloy. The process appears to be driven by the nucleation of small, highly ordered domains within the existing microstructure. We attempt to simulate these and other disordering behaviors through a kinetic Monte Carlo method. For simplicity, we focus these investigations on two-dimensional, ordered AB alloys featuring various first and second neighbor ordering energies. Disorder is imposed in these simulated alloys through manipulation of vacancy-atom exchange rates and forced atomic replacement. For certain disordering-temperature conditions and ordering energies $J_2/J_1 \lesssim 0.5$, a previously unreported patterning of order is observed, dividing the ordered microstructure into competing, highly ordered domains. This behavior is rationalized in terms of decreased anti-phase boundary energies at the given ordering energies, and a physical picture of the patterning reaction is presented. The application of this picture to Cu_3Au is deemed plausible and future work proposed.

ACKNOWLEDGEMENTS

This work was only possible through the help and kindness of a great many people. First and foremost, I would like to thank my advisors and co-chairs, Professor Robert Averback and Professor Pascal Bellon. Without your guidance, persistence, and – yes – hard questions, I would be a worse person and a worse scientist. I would also like to thank the researchers of Argonne National Laboratory's Intermediate Voltage Electron Microscope for their time and helpful discussions, particularly on the preparation and alignment of our diffraction experiments. Mark, Meimei, Ed, and Pete, I could not have done this without you. In that same vein, I am forever indebted to the assistance of my fellow graduate research assistants, Andrew Long and Rebecca McAuliffe, whose help developing a MATLAB digitization script and expertise with prolonged heat treatments meant the world for this project.

I would also like to extend my thanks to the members of my research group and the staff of the Center for Microanalysis of Materials, who put up with me on a daily basis for five and a half years. To Doctors Stumphy, Ekiz, Zhang, Shu, Lach, and Lee, I apologize for never realizing just how much you meant until we were no longer coworkers. To those who are still there in the Materials Research Laboratory, I wish you all the best – especially John Beach, who will be inheriting my laboratory safety and maintenance jobs. And to Doug, Wacek, Mauro, Ernie, Dawn, and Chris, I hope you all survive the present renovations and enjoy many years to come.

Lastly, I want to thank all the people who did not know me in the lab, the friends who kept me sane, who played board games, who ran through corn mazes and put on fancy dinner parties because we could. Most of all, I want to thank my mother, father, and sister for their undying love and patience, without which I would not be the man I am today.

To my parents, Paul and Bobbi.

TABLE OF CONTENTS

CHAPTER 1

INTRODUCTION

Materials under irradiation act as dissipative systems, exchanging energy and often matter continuously with their surroundings [1]. Often described as external forcing, this exchange can produce chemical and structural defects, chemically mix multi-component systems, and generally lead to non-equilibrium behavior. In particular, in materials under irradiation, defect production creates supersaturations of vacancy and interstitial defects which, at high temperatures, results in radiation enhanced diffusion (RED). The migration and annihilation of these defects at dislocations, grain boundaries, and other such sinks can further produce persistent fluxes of defects and solute atoms through a material. In contrast to these thermal effects, chemical mixing involves the displacement and relocation of atoms throughout the material because of recoil events within collision cascades. Because such mixing is not dependent on the energetics of the material, it can play an important role in the evolution of chemically ordered materials, by introducing disorder, and of immiscible phase systems, through homogenization. Moreover, the interaction of this mixing and RED can lead to a dynamical competition between the two processes, resulting in self-organization behavior. Compositional patterning, for instance, has been observed in several binary and ternary alloys under high-temperature irradiation [2-6]. Although these concepts of self-organization in irradiated alloys are generally acknowledged, our understanding remains basic for systems with even the barest complexity. Here, we use the alloy Cu_3Au to investigate the disordering and patterning of chemical order under ion irradiation, as ordered alloys have been studied for decades to illuminate processes of chemical mixing and RED.

This work was motivated in no small part by past observations of anomalous disordering in Cu_3Au under ion irradiation. As an approximation and ignoring the role of short lived interstitial defects, the rate of disordering under irradiation is,

$$\frac{dS}{dt} = -\varepsilon K S + \frac{C_v^{irr}}{C_v^{eq}} \frac{\partial S}{\partial t}\Big|_{th} (S,T) \tag{1.1}$$

where S is the long range order parameter, t is the irradiation time, ε is the chemical ("anti-site") defect production rate per collision event, K is the rate of collision events in time, C_v^{eq} and C_v^{irr} are the vacancy concentrations at thermal equilibrium and induced by irradiation, and $\frac{\partial S}{\partial t}\Big|_{th}$ is the thermally driven recovery rate. Equation 1.1, in short, describes the balance between the loss of long range order to collision events and the acceleration of recovery due to RED of vacancy defects. Despite proving accurate for many types of irradiation conditions (see Section 1.3.2), measurements of resistivity under light-ion irradiation by Lee [7] and Lang [8] have recently shown an anomalous rise in the initial rate of disordering for Cu_3Au for experiments conducted near the thermal order-disorder transition at $T = T_c$. Because S and $\frac{\partial S}{\partial t}\Big|_{th}$ are well known to decrease and increase on approaching T_c, this finding is counter to the change, if any, would be expected from Equation 1.1. We note, however, the rigor used in these resistivity measurements, including: 1) the use of single crystal molecular beam epitaxy to grown stoichiometric and sink-free films; and 2) the use of He^+ and Ne^+ beams at several currents to remove ion and dose rate effects. Lee, *et al.* hypothesized that the 2 to 5 times increase seen in Figure 1.1 may arise from unbalanced fluxes of vacancies from collision events to the film surfaces. While their free energy calculations, comparing the excess energy of vacancy supersaturation at the event site to that of

the produced disorder, supported such a coupling between defect fluxes and disorder, no specific mechanisms were offered.

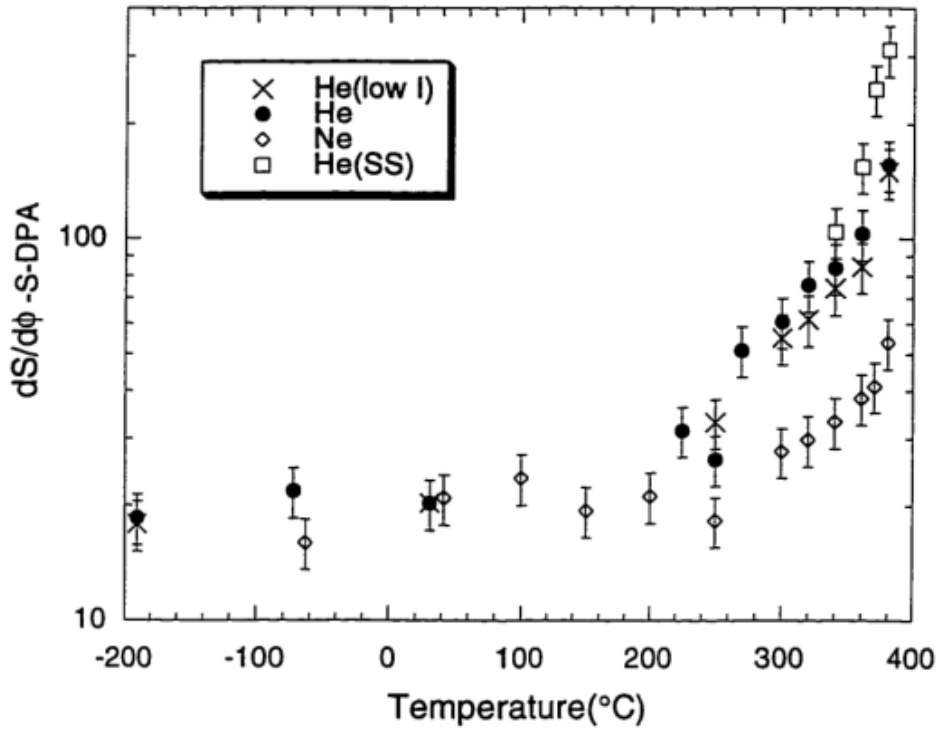

Figure 1.1: Initial disordering rates measured by electrical resistivity as a function of. irradiation temperature, with values normalized by the defect production rates of the respective ions. Here, "low I" markers indicate He^+ irradiations conducted at lower beam currents (i.e. lower dose rates), and "SS" markers indicate He^+ irradiations carried out from one steady state to another. All ion species display a marked increase in disordering above 250 °C. After [7].

The work presented here focused on creating a physical picture of the radiation induced disordering described above, using *in situ* transmission electron microscopy and electron diffraction of Cu_3Au for direct characterization of the ordered microstructure and atomistic simulation of ordered alloys to investigate the energetic and dynamical aspects of the disordering phenomena. This chapter will provide essential background on radiation damage to materials in general and on the behavior chemically ordered alloys specifically, in order to best convey the fundamental points of this dissertation:

1. Is the anomalous disordering rate near T_c verifiable using another experimental technique? Is there a connection between this behavior and the corresponding microstructures?

2. What irradiation conditions, in terms dose rate and temperature, are necessary for this anomalous disordering?

3. What process(es) are responsible for the anomalous disordering rate near T_c? Does the disordering strongly depend on thermodynamic and kinetic parameters of the alloy? Can it occur only in Cu_3Au, or should it be seen in other chemically ordered alloys?

4. How does disorder propagate under irradiation, and how does the propagation couple with the defects diffusion and the ordered microstructure?

1.1. BASICS OF RADIATION DAMAGE

Radiation-solid interactions have been subject to intense study for the better part of a century, with most important aspects understood by the 1970's. Basic observations on the distribution of irradiation defects and collision cascade structure made by Brinkman, *et al.* [9] as early as 1954. Initial theories for defect behavior and production following damage events followed from Seitz and Koehler [10] in 1954 and from Kinchin and Pease [11] in 1955, respectively. Seeger [12] created an oft reproduced sketch of damage processes, shown in Figure 1.2, in 1958, and Vinyard, *et al*. [13] reproduced these same effects – along with demonstrating the shared site form of radiation induced interstitials – in the first simulations of radiation damage in 1960.

While the early years of the field provided a solid theoretical understanding of radiation damage, a great amount of computational and experimental work remain. Particularly lacking was a precise understanding of defect behavior: how many are created per event, what is the

arrangement of these defects in space, and how do defect populations evolve with time? Further, how do the tremendous energy and disorder present within collision cascades affect complex alloys, driving phase transformations or allowing access to metastable states? Computationally, these questions pose difficult multi-scale problems in time and space, ranging from picoseconds to years and from Angstroms to centimeters. Experimentally, they push the bounds of spatial and temporal resolution, requiring near impossible observation of atomic-scale behavior over infinitesimally short times. The basics of radiation damage in metals will presented in the following section, linking those concepts introduced to the effects studied in this work.

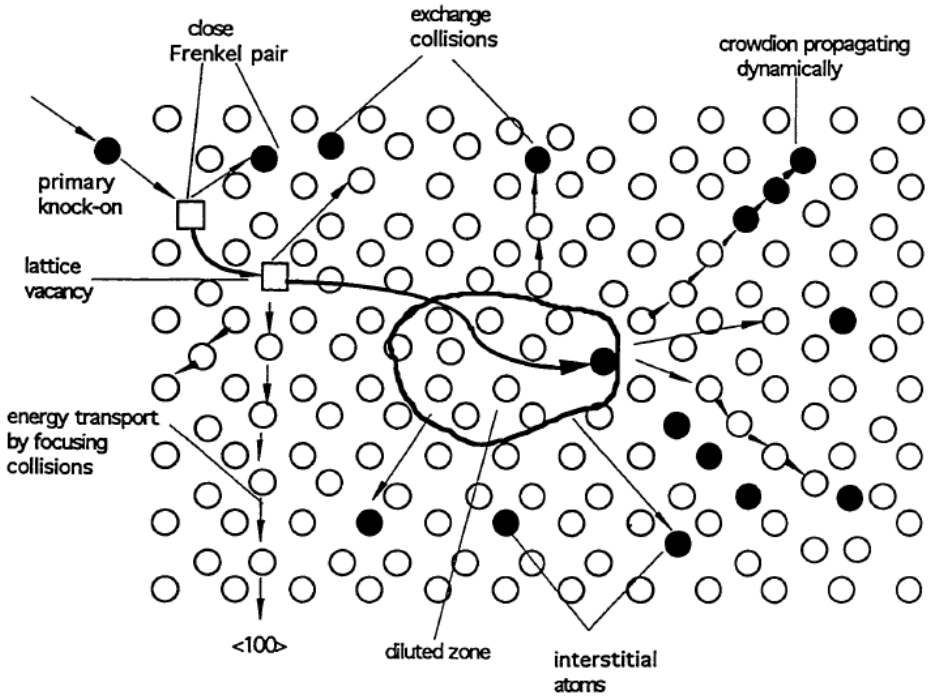

Figure 1.2: A schematic depiction of damage mechanisms at work for a collision cascade in Cu due to fast neutron bombardment. After [12].

1.1.1. Transfer of Energy to Solids

Understanding the forms and consequences of radiation damage begins with the ways in which energetic particles impart energy to solid materials. This exchange is customarily divided into electronic and nuclear stopping mechanisms, which is roughly equivalent to dividing inelastic

and elastic processes [14]. During electronic stopping, incident particles are gradually slowed by the loss of energy to electrons of the solid. This does not alter the trajectories of particles, due to the large difference in mass, and produces no damage in metals. In fact, the primary impact of electronic stopping on the irradiation of metals is the reduction of energy that might otherwise have gone to displacement damage. In contrast, nuclear stopping involves large, discrete transfers of energy through collisions of incident particles with atoms of the solid. These collisions can result in large deflections of incident particles and are responsible for the defect production and disordering discussed throughout this chapter. The relative strengths of electronic, S_e, and nuclear, S_n, stopping are shown in Figure 1.3 as a function of the reduced energy, $\epsilon \propto E$. In brief, S_n dominates when the particle energy is low or the target atom heavy, while S_e is dominant at high energies and low target mass. For irradiation of metals, we therefore concern ourselves primarily with the loss of energy to elastic, nuclear collisions.

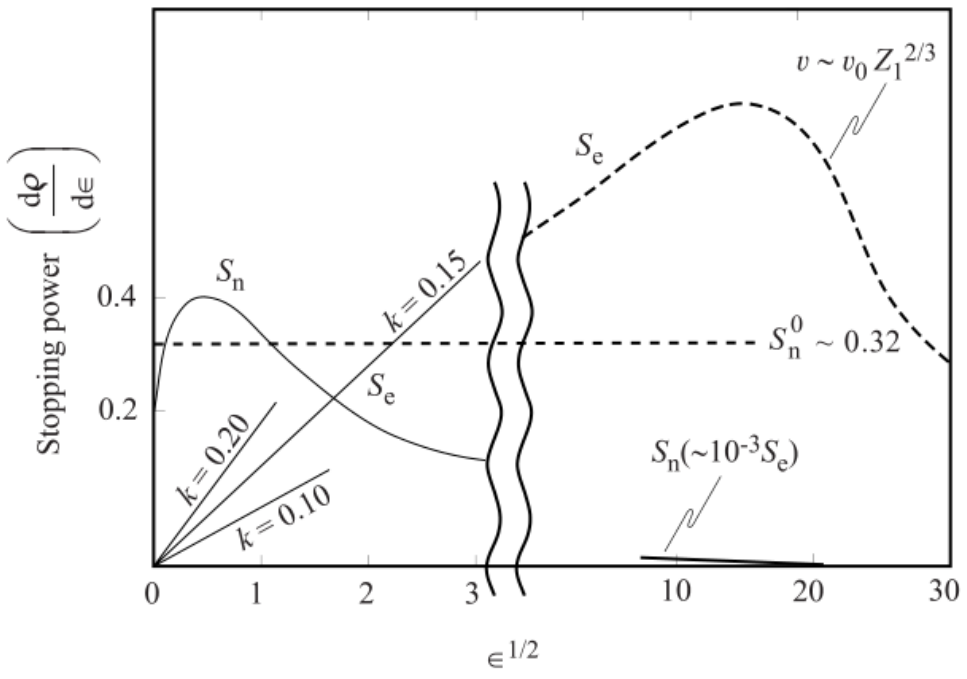

Figure 1.3: Trends in stopping power with normalized energy. Note the change in dominance from electronic, S_e, to nuclear, S_n, stopping power as ions slow. After [15].

Before exploring the specific processes by which energy loss becomes damage, it is worth noting the importance of particle selection. Many of the relevant details become apparent when comparing the weighted recoil spectrum, $W(T)$, of various incident particles, where $W(T)$ represents the fraction of damage energy created by recoils with energies at or below T [16, 17]. (Note: it is convention to represent the energy lost to a nuclear collision, or recoil, with the symbol T. We will take care in this section to emphasis the meaning of T whenever it appears.) Example spectra are shown in Figure 1.4 for 1 MeV particles into Ni. Perhaps the most striking feature of the spectra is the large difference between those of protons and neutrons, equally massed particles. The difference then must be due to the cross sections (i.e. probabilities) of Coulomb versus hard-sphere scattering. Because we often aim to emulate neutron damage in reactor environments, only at higher speed and without radioactivity, it is common to define a parameter, $T_{1/2}$, such that $W\left(E, T_{1/2}\right) = \frac{1}{2}$. The relative values of $T_{1/2}$ can then be used to compare incident particles.

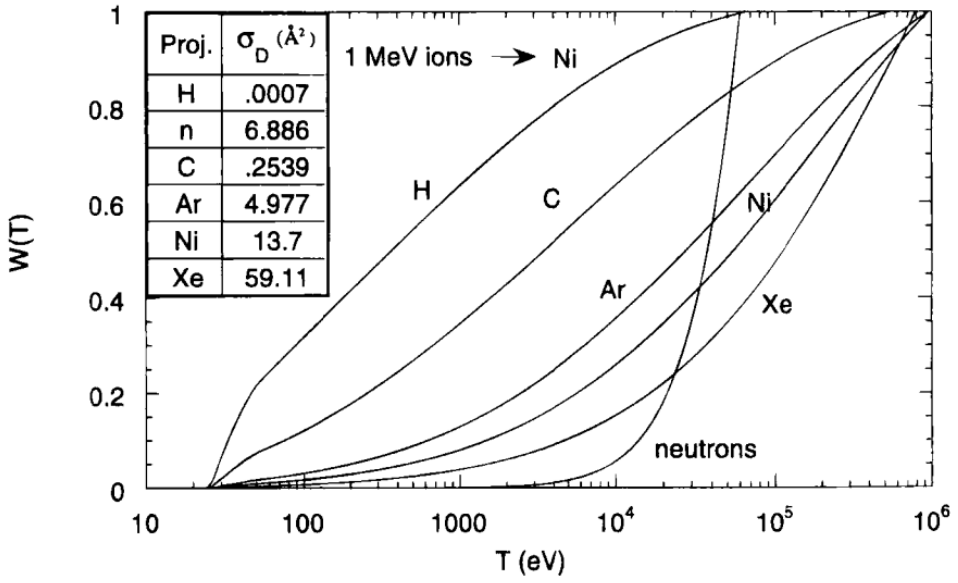

Figure 1.4: The weighted recoil spectrum, $W(E,T)$, for various 1 MeV particles incident on Ni, showing the fraction of damage energy from recoils below T. Note the large difference in spectra between protons and neutrons, caused by their differing cross sections in spite of having equal mass. After [16].

The way in which transferred energy becomes damage also varies with the chosen incident particle. For electron irradiation, the low particle mass relative to the target atom, usually called the "primary knock-on atom" (PKA), leads to transfers of energy on the order of 100 eV, and only a small number of atoms can be displaced by a single recoil. Surviving defects from such collisions are commonly formed through replacement collision sequences (RCS), in which atoms are repeatedly displaced by and then displace their own neighbors along close-packed rows of the lattice. These RCS events result in an isolated Frenkel pair and represent a form of forced atomic transport, which can lead to chemical disordering in ordered alloys [11] and non-equilibrium mixing in others. Irradiation with neutrons or heavier ions, by contrast, can produce energy transfers above ~1000 eV, allowing the formation of the collision cascades (also known as displacement or damage cascades) described in the following text. In either case, the number of Frenkel defects formed per event can be roughly estimated using the method proposed by Norgett, Robinson, and Torrens (NRT) [18],

$$\upsilon(E_0) = \int_{E_d}^{E_0} \frac{dE}{S_e(E) + S_n(E)} \int_{E_d}^{T_{max}} dT \frac{d\sigma(E,T)}{dT} \times \upsilon^{KP}(T) \tag{1.2}$$

where E_0 is the initial energy of the incident particle, E_d is the energy, typically ~25 eV for metals, necessary to displace an atom from its lattice site, T_{max} is the maximum transferrable energy between particle and PKA based on their masses and atomic numbers, and $\sigma(E,T)$ is the scattering cross section for collisions of the given particle. The production term, $\upsilon^{KP}(T)$, used in this NRT model is a modified version of the formula described by Kinchin and Pease [19] for Frenkel pair production,

$$\upsilon^{KP}(T) = \begin{cases} 0, & T < E_d \\ 1, & E_d < T < 2.5E_d \\ \dfrac{0.8E_D}{2E_d}, & T > 2.5E_d \end{cases} \tag{1.3}$$

where E_D is the damage energy deposited in the PKA.

1.1.2. Evolution of Collision Cascades

When recoils transfer sufficient energy to the PKA, secondary knock-ons may occur as the PKA collides with neighboring atoms. This process, known as a collision cascade, continues through a rapid succession of ballistic events until the energy transferred between recoiling atoms falls below E_d. Lasting on the order 0.1 ps [20], such ballistic damage produces an inhomogeneous and unstable distribution of atoms [17, 21], rich in vacancies at its core and surrounded in its periphery by excess interstitial defects. Most of these initial defects are lost to spontaneous pair recombination during the subsequent relaxation of the cascade over ~1 ps. Although many defects are lost, a large portion of the initial knock-on energy is trapped in the cascade as heat. This thermal spike is characterized by liquid-like density and temperature and has been well-studied by molecular dynamics (MD) simulation [22-25]. The size and lifetime of these "melted" regions depend on the heat capacity and thermal conductivity of a given material, and MD simulations of Au, for example, have shown that temperatures can reach several times the melting temperature, T_m [21]. The sequence of ballistic, relaxation, and thermal spike stages is shown in Figure 1.5. While the chemical disordering effects of thermal spikes will be discussed further in Section 1.3, several of their structural effects are noteworthy as well. Thompson and others [26, 27] have shown that intersections between thermal spikes and the surface of a material can release atoms by ejection and evaporation with sufficient heat and life-time. Moreover, the role of thermal spikes in ion beam mixing has been modeled [28, 29] as an additional effect to ballistic mixing.

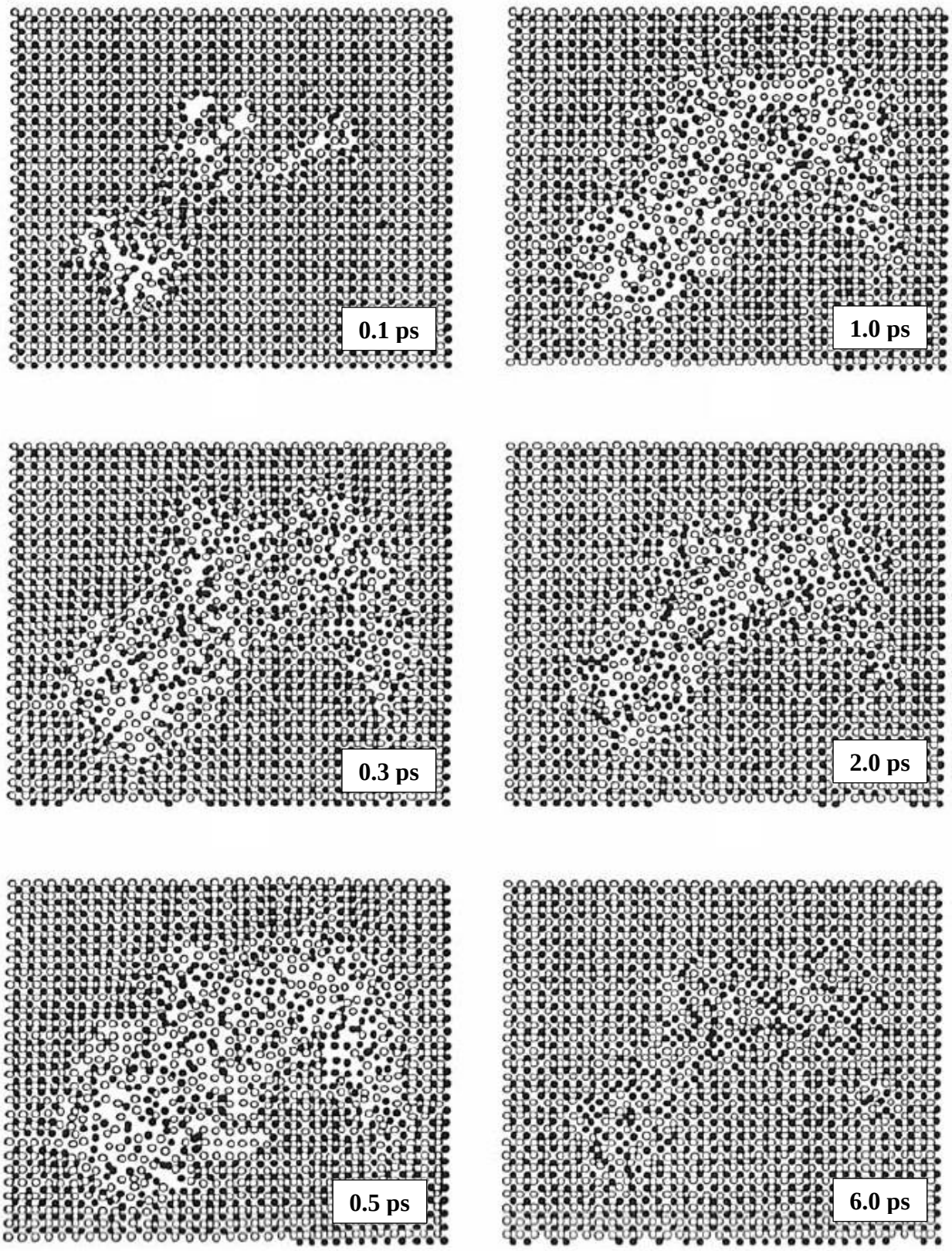

Figure 1.5: Cross-sectional slabs, two (100) *planes deep, showing the evolution of a simulated thermal spike in NiAl. Filled and empty circles represent Ni and Al atoms, respectively. After [30]*

Because so many radiation-induced changes to materials are driven by point defects, accurate predictions of their production by collision cascades is especially important. Experimental [31] and simulation [16, 32] studies, however, have shown that the Kinchin-Pease model overestimates the actual production of Frenkel pairs by a factor between 2 and 10, depending on the irradiating particle, and of mobile defects by a factor of ~2 further. This discrepancy is attributed by Averback [33] to: 1) the shortening of RCS's initialed within collision cascades by thermal and structural disruptions of the lattice [34]; 2) the spontaneous recombination of defects formed within the melt zone of cascades [35]; and 3) the collapse of defects into the solidifying cascades, forming defect clusters and dislocation loops [22]. Such losses are commonly discussed in terms of a defect production efficiency (i.e. simulated divided by predicted yield), which varies with irradiation condition. This efficiency was found by simulation [25, 36-38] to decrease quickly from 1 to ~0.3 as the transferred energy, T, was increased from a few E_d to several keV, reflecting the transition from the production of a few Frenkel pairs to full cascades and supporting previous experiments [31, 39]. Similar variations in efficiency were experimentally observed for increasing ion mass by Wei, *et al.* [40], with the efficiency relative to He^+ irradiation decreasing to 0.4 for Ne^+ and 0.2 for Ar^+.

1.1.3. Point Defect Populations

The structural evolution of metals under various service conditions and the resulting changes to their mechanical properties are a central focus in the field of physical metallurgy. Because such changes are most often products of point defect diffusion, an understanding of these defects under equilibrium and non-equilibrium conditions is essential. In this section, we will provide an understanding of: 1) defect concentrations with and without irradiation; 2) the roles

played by temperature and defect sinks; and 3) the basic enhancements to material behavior from non-equilibrium defect populations.

As described above, point defects in simple metals consist of vacancy and interstitial defects formed as pairs when an atom is removed from its site in the crystal lattice. While this removal results in broken bonds with the former neighbors of the atom, increasing the internal energy, the addition of randomness to the system leads to greater configurational entropy. These opposing energies lead to changes in the free energy, G, with defect concentration. In following equations, we will consider these effects in terms of only the vacancy concentration, C_v, but an identical derivation exists for the interstitial concentration, C_i. Under equilibrium conditions, C_v will be determined by the minimization of the free energy,

$$\frac{dG}{dC_v}\left(C_v^{eq}\right) = 0 \tag{1.4}$$

where C_v^{eq} is the equilibrium vacancy concentration.

Because $C_v^{eq} \ll 1$ even near T_m, we can ignore the role of vacancy-vacancy interactions and determine the change in enthalpy, ΔH, directly from the added vacancy concentration,

$$\Delta H \approx \Delta H_f C_v \tag{1.5}$$

where ΔH_f is the enthalpy of formation for a vacancy. The accompanying change in entropy, ΔS, however, comes from two sources. First is the change in vibrational entropy, ΔS_v, from alterations to the vibrational frequencies of atoms neighboring the now empty site. This contribution is small compared to the changes in configurational entropy, and the total change is given by,

$$\Delta S = C_v \Delta S_v - k[C_v \log(C_v) + (1 - C_v)\log(1 - C_v)] \tag{1.6}$$

where k is Boltzmann's constant. (Throughout this work, the function "log" will denote the natural logarithm, not the base 10.) Combining changes in enthalpy and entropy, we find that the free energy of the crystal with vacancies is,

$$G = G_0 + \Delta H_f C_v + C_v T \Delta S_v - kT[C_v \log(C_v) + (1 - C_v)\log(1 - C_v)] \tag{1.7}$$

where G_0 is the free energy of the vacancy-free lattice. Using the derivative of Equation 1.7 and our assumption $C_v^{eq} \ll 1$ with Equation 1.4 leads to,

$$C_v^{eq} = \exp\left(\frac{-\Delta G_f}{kT}\right) \tag{1.8a}$$

$$\Delta G_f = \Delta H_f - T\Delta S_f \tag{1.8b}$$

With the addition of irradiation, however, the point defect concentrations evolve according to a competition between production by irradiation, recombination with opposite defects, and annihilation at sinks in the lattice. The latter two effects occur by diffusion of surviving, mobile defects following thermal spikes, and are thus dependent on temperature, defect mobility in the lattice, and the density of sinks such as dislocations, interfaces, and surfaces. The evolution of point defect concentrations can thus be described by the rate equations [15, 41],

$$\begin{aligned} \frac{dC_v}{dt} &= K_0 - K_{iv} C_i C_v - K_{vs} C_v C_s \\ \frac{dC_i}{dt} &= K_0 - K_{iv} C_i C_v - K_{is} C_i C_s \end{aligned} \tag{1.9}$$

where K_0 is the rate of defect production with irradiation, K_{iv} is the rate coefficient for recombination, and K_{vs} and K_{is} are the rate coefficients for annihilation of vacancies and interstitials at sinks, respectively. These rate coefficients are generally given by,

$$\begin{aligned} K_{iv} &= 4\pi r_{iv}(D_i + D_v) \\ K_{is} &= 4\pi r_{is} D_i \\ K_{vs} &= 4\pi r_{vs} D_v \end{aligned} \tag{1.10}$$

where r_{iv}, r_{iv}, and r_{iv} are the interaction radii for reactions between the subscript species; and D_i and D_v are the interstitial and vacancy diffusion coefficients. Equation 1.9 makes several important assumptions about the system under irradiation, including that: 1) the distribution of point defects is homogeneous (i.e. $\nabla C_x \approx 0$); 2) defect clustering is nonexistent after the initial thermal spike; 3) the population of sinks is unchanging, unbiased with respect to defect type, and has infinite capacity for absorbing defects; and 4) that thermal defects are negligible. While these assumptions, #3 in particular, represent significant limitations, better modeling of such effects is beyond the scope of this work. Some insight, however, can still be gained by examining analytical solutions to Equation 1.9 for the steady state defect concentrations under extremes of temperature or sink density.

Steady state defect concentrations, C_v^{irr} and C_i^{irr}, are found by solving Equation 1.9 for the defect concentrations when $\frac{dC_v}{dt} = \frac{dC_i}{dt} = 0$,

$$\begin{aligned} C_v^{irr} &= -\frac{K_{is}C_s}{2K_{iv}} + \left[\frac{K_0 K_{is}}{K_{iv}K_{vs}} + \left(\frac{K_{is}C_s}{2K_{iv}}\right)^2\right]^{1/2} \\ C_i^{irr} &= -\frac{K_{vs}C_s}{2K_{iv}} + \left[\frac{K_0 K_{vs}}{K_{iv}K_{is}} + \left(\frac{K_{vs}C_s}{2K_{iv}}\right)^2\right]^{1/2} \end{aligned} \tag{1.11}$$

When irradiation takes place at low temperatures, defect diffusion is greatly reduced. If this limited mobility is combined with a low sink density, mutual recombination will have a much greater limiting effect on the defect populations than annihilation at sinks. The steady state defect concentrations in this "recombination dominated regime" can then be approximated by,

$$C_v^{irr} \approx \left(\frac{K_0 K_{is}}{K_{iv} K_{vs}}\right)^{1/2}$$
$$C_i^{irr} \approx \left(\frac{K_0 K_{vs}}{K_{iv} K_{is}}\right)^{1/2} \quad (1.12)$$

At high temperatures and in the presence of a high sink density, on the other hand, the concentration of faster diffusing interstitial defects is kept low, limiting recombination. In this "sink dominated regime", the steady state defect concentrations are approximately,

$$C_v^{irr} \approx \frac{K_0}{K_{vs} C_s}$$
$$C_i^{irr} \approx \frac{K_0}{K_{is} C_s} \quad (1.13)$$

The transition between these regimes is particularly important for alloys under irradiation, as point defects under the sink dominated regime will diffuse further and therefore be more active in diffusive forms structural evolution (e.g. segregation, coarsening). The critical irradiation conditions for this transition can be found following the derivations of Was [15],

$$K_0^* = 2 D_v C_s^2 K'_{is} K'_{vs} / K'_{iv} \quad (1.14)$$

where K'_{iv}, K'_{is}, and K'_{vs} are the quantities given in Equation 1.8 without the relevant diffusion coefficients. For thin films with especially low densities of sink, $C_s \approx 0$, Lee, *et al.* [42] defined a new sink loss term, $K_{xs} C_v = (\pi/2L)^2 D_x C_x$, for use in place of $K_{xs} C_x C_s$ in Equation 1.9, where x can be v or i. While we will not reproduce the full derivation of the above equations with this new term, we note their description of a parameter, X, for the relative strengths of recombination and annihilation at sinks, which then determines the critical vacancy concentration, C_v^*, for the onset of the recombination regime according to,

$$X = \frac{K_{iv} C_i^{eq} C_v^{eq}}{K_{is} C_i^{eq}} \tag{1.15}$$

$$C_v^* \approx \begin{cases} 2C_v^{eq}, & X > 1 \\ C_v^{eq}/X, & X < 1 \end{cases} \tag{1.16}$$

1.2. CHEMICAL ORDER IN ALLOYS

The behavior of chemically ordered alloys with temperature has been the focus of much study, and there exist several excellent reviews [43-46] of the theoretical and experimental literature. As the experimental studies of this work focus on the alloy Cu_3Au, we will use its behavior throughout this section as an example of the points discussed and as a benchmark for comparing systems. In metal alloys, chemical order is expressed through the arrangement of atoms into short and long range patterns according to species. On the crystalline lattice, these patterns create distinct sublattices populated by only one species. The "$L1_2$" type ordered structure of Cu_3Au, shown in Figure 1.7a, is divided into four such sublattices, with one for each of the atomic positions in the face centered cubic (fcc) primitive cell. The assignment of species to particular sublattices gives rise to distinct ordered variants, shown in Figure 1.7b. Because distant regions of the lattice may take on different variants during ordering, chemically ordered alloys are divided

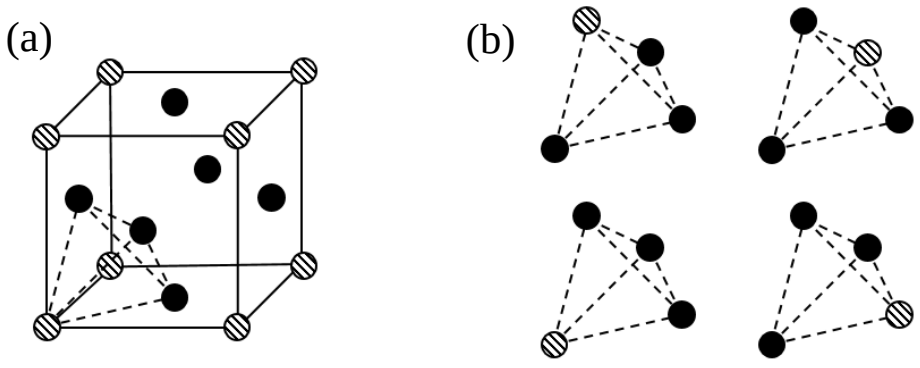

Figure 1.6: (a) The $L1_2$ ordered structure common for A_3B alloys. (b) The four ordered variants of the $L1_2$ structure, shown through their primitive cells. For the Cu_3Au studied here, Cu and Au atoms would occupy filled and hatched sites, respectively.

into domains similarly to magnetic materials. Defects in the order of these domains and the interfaces between them make up a kind of "ordered microstructure" and will be central to the present work.

1.2.1. Order Parameters

The concept of long range order in alloys was first suggested by Tammann [47] in 1919. Combined with odd resistivity measurements of Cu-Au alloys [48] and the observation of new diffraction lines in powder X-ray diffraction (XRD) [49, 50] – all temperature dependent, this new idea fueled theoretical discussion throughout the 1920's. The problem took real shape in 1934 and 1935, with the publication of a model by Bragg and Williams [51-53]. Based on statistical thermodynamics, this Bragg-Williams model represented a "zeroth-order" approximation of chemical order and assumed both random disordering and an ordering force derived from a mean field of order, $W = W_0 S$. Although simple, the model reproduced important features of order-disorder behavior for AB (CuZn) and A_3B (Cu_3Au) cubic systems. Long range order in alloys is described according to an order parameter, S, introduced in the Bragg-Williams model and based on the fraction of A and B atoms occupying their respective α and β sublattices,

$$S = \frac{P_a^\alpha - X_a}{X_\beta} = \frac{P_b^\beta - X_b}{X_\alpha} \tag{1.17}$$

where P_a^α and P_b^β are the fractions of α and β sites "correctly" occupied; X_a and X_b are the fractions of atoms with species A and B; and X_α and X_β are the fractions of α and β sublattice sites in the lattice. By this definition, the order parameter is $S = 1$ for the fully ordered lattice and $S = 0$ for a random solution, with intermediate states between.

This formulation of the order parameter is especially powerful as an analysis tool, because both diffraction and resistivity measurements are known to vary with S^2. For diffraction, the method was developed by Wilchinsky [54] for powder XRD analysis and is commonly used according to,

$$S^2 = \left(\frac{I_s}{I_f}\right)_S \Big/ \left(\frac{I_s}{I_f}\right)_{S=1} \tag{1.18}$$

where the I_f terms are diffracted intensities for a "fundamental" reflection (e.g. 200 in fcc); the I_s terms are diffracted intensities for a "superlattice" reflection (e.g. 100 in fcc); and the $S = 1$ fraction has been added to the original form because absorption effects are not easily calculated from single patterns in most techniques. (For a more detailed explanation of superlattice reflections, see Section 1.2.4 below.) For resistivity, Muto [55] extended existing theory for electron scattering by substitutional impurities [56] to variations with partial order, showing that the resistivity, ρ, after accounting for thermal vibrations, is related to S by,

$$S^2 = 1 - \frac{\rho - \rho_{S=1}}{\rho_{S=0} - \rho_{S=1}} \tag{1.19}$$

Although the Bragg-Williams model was a major advancement in our understanding of chemical order, the absence of short range order from the approximation is a defect. As pointed out by Bethe [57], the local configuration of atoms determines the forces of ordering on individual lattice sites, and the long range order of an alloy only reflects such configurations on average. Bethe thus proposed an alternative statistical thermodynamic model for chemical order based on pair interactions, in essence expanding the Bragg-Williams model from single atoms in a mean field to pairs in a mean field. While this chapter will not survey the details of every energetic model, the new short range order parameter, s, introduced by Bethe is noteworthy. This parameter

is determined by the fraction, q, of "unlike" (i.e. A-B) nearest neighbor pairs in the alloy and is written as,

$$s = \frac{q - q_r}{q_m - q_r} \tag{1.20}$$

where q_m is the maximum q for the system and q_r is the average q for a random solution. By definition, systems with perfect long range order ($S = 1$) must also have perfect short range order ($s = 1$), but there are many situations in which an alloy may have no long range order while retaining considerable short range order.

This type of order parameter was popularized through the XRD studies of Warren and Cowley, the latter of whom [58] defined short range order parameters, s_i, for neighbor shells of B atoms as,

$$\begin{aligned} \alpha_i &= 1 - \frac{q_i}{X_a} \\ s_i &= \frac{\alpha_i}{\alpha_i^0} \end{aligned} \tag{1.21}$$

where i denotes the neighbor shell being considered, α_i and α_i^0 are the unnormalized short range orders of the current and perfect alloys, respectively, q_i is the fraction of unlike ith neighbor pairs, and X_a is the atomic fraction of A atoms in the alloy. With time, "Warren-Cowley" order parameters of the type given in Equation 1.21 have become more widely used than the Bethe form. This stems from oscillations in the values of α_i^0 with i which are characteristic to given ordered structures. In a perfect $L1_2$ structure, for example, $\alpha_i^0 = -\frac{1}{3}$ for odd i and $\alpha_i^0 = 1$ for even i. Fourier analysis can used to compute α_i values for experimental XRD data, allowing for identification of the type and strength of short range order [59]. Further, trends in α_i with

temperature can be used to fit the effective ordering energies at each neighbor shell, as Cowley did for his own model [58] of chemical order in Cu_3Au.

1.2.2. Equilibrium Order-Disorder Transition

The study of chemical order in alloys began with the effects of temperature, because this parameter is easily controlled in the laboratory and its role in statistical thermodynamic models was established early on. The energetics of such models are based on the concept of ordering energies, V, which encourage the "correct" occupancy of sublattice sites (i.e. α sites with A atoms). For simplicity, the cohesive energy in these models is treated as a sum of pure species interaction energies (a somewhat poor choice for approximating metals). The common form for the ordering energies is written as,

$$V_i = E_{ab}^{(i)} - \frac{E_{aa}^{(i)} + E_{bb}^{(i)}}{2} \tag{1.22}$$

where i denotes the neighbor shell and the E terms are the energies of A-B, A-A, and B-B pairs at that distance. V will usually be negative for chemically ordering alloys, and the long range order at thermal equilibrium can be found by minimizing a free energy of mixing,

$$F_{mix} = E_{mix} - TS_{mix} \tag{1.23}$$

where E_{mix} is the internal energy of mixing, T is again the temperature, and S_{mix} is the configurational entropy of mixing. (Note: to minimize confusion between the symbol conventions for long range order and entropy, we will consistently refer to the latter as S_{mix}. All other uses of S will refer to order.)

By incorporating a nearest neighbor ordering energy, V_1 as written in Equation 1.22, into the Bragg-Williams approximation, E_{mix} and S_{mix} can be written for $L1_2$ systems as,

$$E_{mix} = \frac{N z_1 V_1}{16}[3 + S^2] \tag{1.24a}$$

$$\begin{aligned} S_{mix} &= k \log\left[\frac{\left(\frac{3N}{4}\right)!\left(\frac{N}{4}\right)!}{(N_a^\alpha)!\,(N_b^\alpha)!}\right] \\ &= -\frac{Nk}{16}\left[3(1-S)\log\left(\frac{1-S}{4}\right) + 3(3+S)\log\left(\frac{3+S}{4}\right)\right. \\ &\quad \left. +(1+3S)\log\left(\frac{1+3S}{4}\right) + 3(1-S)\log\left(\frac{3-3S}{4}\right)\right] \end{aligned} \tag{1.24b}$$

where N is the total number of atoms, z_1 is the coordination number of the nearest neighbor shell, k is the Boltzmann constant, and N_a^α and N_b^α are the number of A and B atoms on α sublattice sites, respectively. Setting $\frac{\partial F_{mix}}{\partial S} = 0$ then gives the equilibrium value of S through the transcendental equation,

$$\log\left[\frac{(1+3S)(3+S)}{3(1-S)^2}\right] = -\frac{2 z_1 V_1}{3kT} S = 4.87 \frac{T_c}{T} S \tag{1.25}$$

where T_c is the "critical temperature" above which chemical order in the alloy vanishes. Although the present work focuses exclusively on the behavior of Cu_3Au, among real alloys, it is instructive to compare this $L1_2$ ordered alloy with a common body centered cubic (bcc) ordered structure, "B2". This structure is the ordered state of the alloy CuZn (β-brass), and the variation of its equilibrium S, based on a similar mathematical analysis, can be written as,

$$\log\left[\frac{(1-S)}{(1+S)}\right] = \frac{z_1 V_1}{kT} S = -2 \frac{T_c}{T} S \tag{1.26}$$

As shown in Figure 1.7, the order-disorder transitions at T_c are very different for B2 and $L1_2$ ordered alloys. B2 systems, on one hand, experience a continuous loss of long range order all

the way to $S = 0$ at T_c. This phase transition displays no latent heat and only a finite discontinuity in heat capacity at the transition. By contrast, the $L1_2$ order parameter is discontinuous ($S = S^* \leftrightarrow S = 0$) at T_c, changing from partial to complete disorder with an accompanying latent heat. Using the Ehrenfest [60] classifications of phase transformations, we can clearly label the B2 transition as "second order" and the $L1_2$ as "first order". In practical terms, this distinction means that the order-disorder transition for B2 systems occurs homogeneously at T_c, while the transition in $L1_2$ systems proceeds by nucleation and growth of one phase ($S = S^*$ or $S = 0$) from the other and requires some degree of heating or cooling beyond T_c to drive the transition. The predicted transition for the $L1_2$ system also highlights the defect in the Bragg-Williams approximation, with neglect of short range order effects leading to a large underestimation of S^*. Cowley [58] corrected for this inaccuracy by describing an infinite series of equations relating ith neighbor short range order parameters, α_i to ith neighbor ordering energies, V_i. Fitting these ordering energies from XRD data for Cu_3Au and rewriting the limiting form of the even i equations in terms of S, Cowley showed that long range order in $L1_2$ systems can be more accurately predicted as,

$$\log\left[\frac{(1+3S^2)(3+S^2)}{3(1-S^2)^2}\right] = \frac{8(V_1 - 3/2V_2 + \cdots)}{kT}S^2 = \frac{16}{3}\frac{T_c}{T}S^2 \qquad (1.27)$$

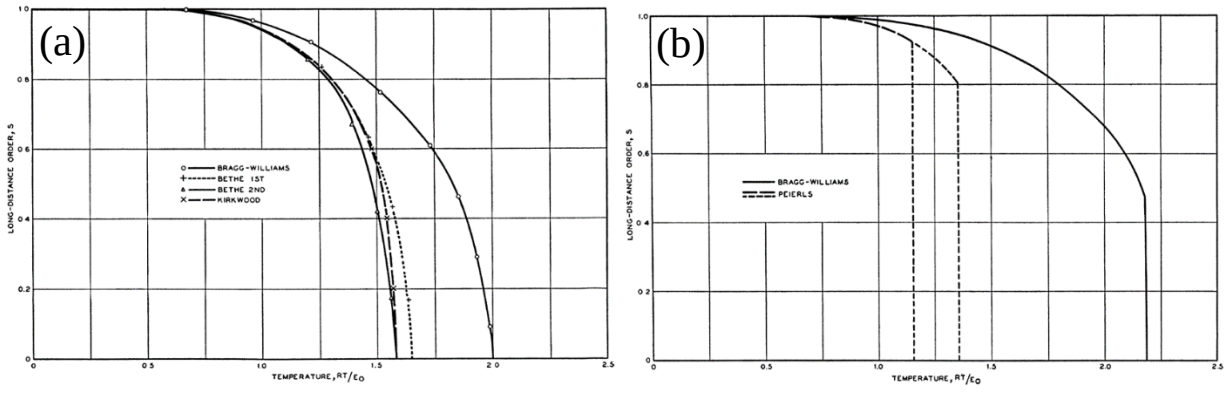

Figure 1.7: Comparison of the equilibrium order-disorder transition in (a) AB (B2) and (b) A_3B ($L1_2$) ordered alloys, where temperature is scaled by the nearest neighbor ordering energy. After [44].

1.2.3. Atomistic Simulation of Order-Disorder Behavior

In the preceding section, our discussion focused on order-disorder behavior in terms of statistical thermodynamic models, demonstrating their ability to reproduce variations in equilibrium long range order, S, with temperature. For problems where the behavior or state of individual particles is of interest, rather than simply the mean field, atomistic simulations are a common alternative. In the case of Monte Carlo (MC) techniques, such as that used in Chapter 3 of the present work, the simulations take on a form similar to that described by Ising [61] for ferromagnetism: a rigid lattice with atoms in place of spins. The energetics of these systems are typically written in terms of pair energies (see Equation 1.22), with the equilibrium state determined by a balance between elementary transitions (e.g. vacancy jumps) [62]. The accuracy of this method can be seen through the early MC work of Fosdick [63], which matched the equilibrium behavior of the Cowley model well.

MC methods have been used to study the equilibrium and non-equilibrium order-disorder behavior of many structures and conditions. In ordered fcc systems alone, these simulations have been used to: 1) build phase diagrams [64, 65] and study phase transitions [66, 67] in terms of ordering energies, composition, and external magnetic fields; 2) measure the effects of the degree of order on diffusion [68]; and 3) explore the kinetics of ordering [69] and of domain coarsening [70] on quenching across the equilibrium transition. (Radiation induced phenomena will be discussed as a whole in Section 1.3, and are thus excluded from this list.) This last point is particularly interesting, as the kinetics of ordering are intimately connected with formation of the ordered microstructure. While the MC literature is divided on the coarsening rate and role of domain anisotropy once this microstructure forms, there is agreement that the prominent anti-phase boundary for the $L1_2$ structure is a low energy, conserved (100) plane which migrates slowly

compared to anti-site ordering processes or the formation of domains on cooling below T_c. This is consistent with experimental results in Cu_3Au, including resistivity measurements of Jones and Sykes [71] and later XRD analysis by Wilson [72] in Cu_3Au.

1.2.4. Electron Microscopy of Chemical Order

In terms of diffraction analysis, electron techniques are largely interchangeable with the X-ray methods mentioned in preceding sections, including Equation 1.18. Electrons do offer a significant advantage in terms of imaging, however, and this section will be devoted to describing how chemical order can be observed by transmission electron microscopy (TEM) [73].

The organization of sublattices during chemical ordering has a marked effect on diffraction. Taking Cu_3Au as our example for this process, we write the structure factor for diffraction as,

$$F = f_\beta + f_\alpha\left[e^{\pi i(h+k)} + e^{\pi i(h+l)} + e^{\pi i(k+l)}\right] \tag{1.28}$$

where f_α and f_β are the average atomic scattering factors on the α and β sublattices of the $L1_2$ structure; and h, k, and l are the Miller indices of the diffracting plane. The structure factor must then be either $f_\beta + 3f_\alpha$, when h, k, and l are all even, or $f_\beta - f_\alpha$, when h, k, and l are all odd or mixed. In the disordered state, $f_\alpha = f_\beta$ and the same reflections are forbidden as in a pure fcc metal. In the fully ordered state, however, $f_\alpha = f_{Cu}$ and $f_\beta = f_{Au}$. This means that reflections with all odd or mixed indices will have a non-zero F, and therefore some intensity. These "superlattice" reflections thus contain information about ordered regions of the alloy and can be just for dark-field microscopy of the ordered microstructure.

In very broad terms, dark-field images are formed by placing a limiting aperture in the diffraction plane of the TEM. This allows only reflections within the aperture to contribute to the final image, and regions of the sample which strongly diffract from those planes are thus bright on

a dark background. Dark-field imaging with superlattice reflections can thus be used to characterize the ordered microstructure, namely the order within its domains and the anti-phase boundaries between them.

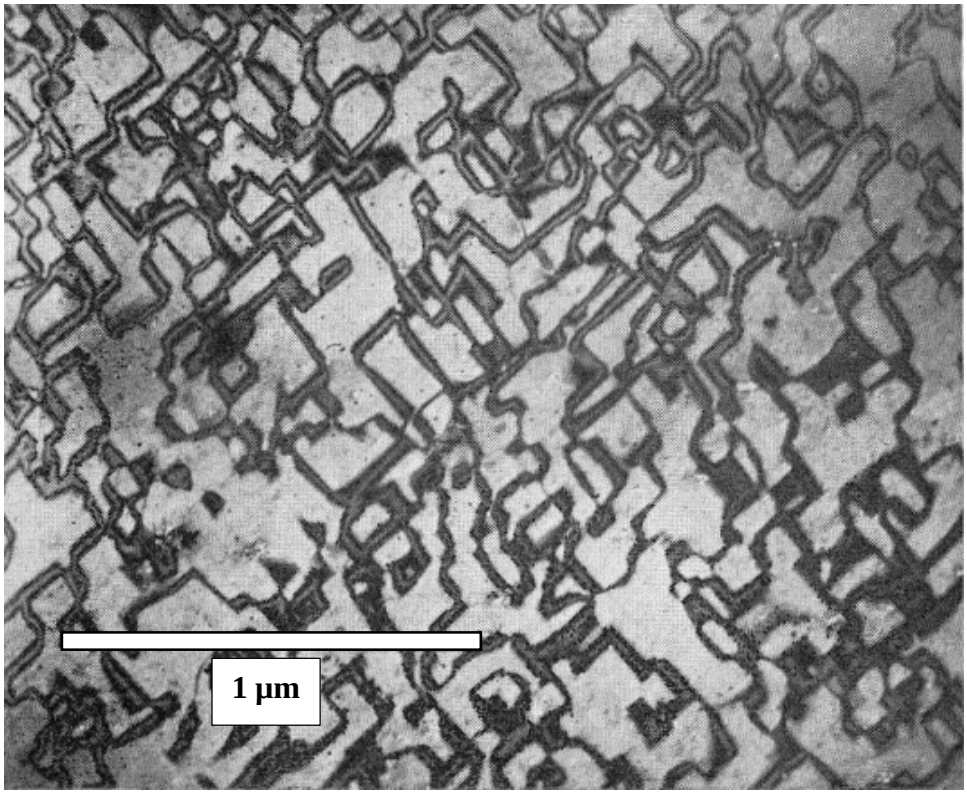

Figure 1.8: Dark-field, superlattice micrograph of ordered domains in Cu3Au. After [74, 75].

First directly observed for CuAu by Owaga, *et al.* [76] in 1958 and for Cu_3Au by Fisher and Marcinkowski [74] in 1961, anti-phase boundary contrast is caused by the displacement, $\boldsymbol{R}$, across the boundary between ordered variants. In Cu_3Au, these displacement vectors are $\frac{1}{2}[110]$, so the phase difference for diffracted electrons, $\alpha = 2\pi \boldsymbol{g} \cdot \boldsymbol{R}$, will be an even multiple of π (i.e. invisible) for fundamental reflections and an odd multiple of π or 0 for superlattice reflections. These $\alpha = 0$ conditions for superlattice $\boldsymbol{g}$-$\boldsymbol{R}$ pairs ultimately mean that one third of anti-phase boundaries will be invisible in dark-field micrographs, regardless of the imaging condition chosen, and lead to the "maze" patterns shown in Figure 1.8. Visible anti-phase boundaries have a fringed

contrast similar to other inclined planer defects (e.g. stacking faults), but the long extinction distances for superlattice reflections ($\xi_g \propto F_g^{-1}$) result in a low number of fringes. The extinction distances for 100 or 110 superlattice reflections at 200 kV are similar, taking values on the order of 750 Å and 1,500 Å for CuAu and Cu_3Au, respectively [75].

1.3. RADIATION INDUCED ORDER-DISORDER

The irradiation of chemically ordered alloys naturally leads to alterations of the ordered state beyond the production of Frenkel pairs. Anti-site defects, in which atoms of one species "incorrectly" occupy a sublattice site of the other, may be created by several mechanisms: random point defect recombination [77], RCS events [19], thermal spikes [78], and the collapse of cascades to vacancy loops [79]. These effects do not always lead to net rates of disorder, however, and thermally activated reordering by irradiation produced point defects can lead to a strong, if initially counterintuitive, recovery of order. In this section, we will explore the ways in which the damage processes discussed in Section 1.1 may result in ordering or disordering of the ordered structures described in Section 1.2.

1.3.1. Disordering Mechanisms

The relative importance of the disordering mechanisms listed above has been found to depend strongly on the nature of the incident particle, with Schulson [80] giving a detailed review of the irradiation of common $L1_2$ ordered alloys. For electron irradiations, collision cascades are not produced due to low relative mass and energy transfer. This leads to increased importance for RCS events and recombination, but variations in the disordering efficiency and length of RCS events makes the dominant factor difficult to determine. In contrast, collision cascades form at most appreciable energies of fast neutron or ion irradiations, making thermal spikes and RCS events the dominant mechanisms for disorder. Recombination is still a factor for such irradiations,

but it is thought to be relatively inefficient at creating disorder with an estimated efficiency, ε, of ~3 replacements per displacement. Cascade collapse is similarly considered to be unimportant, as dislocation loops are not observed following irradiations of most $L1_2$ alloys. This may be an artifact of annealing loss following *ex* situ experiments and the temperature dependence of cascade collapse, however, as proposed by the recent, *in situ* work of Daulton, *et al.* [81] in pure metals.

Given their relative importance, we thus limit our focus to the disordering efficiencies of RCS events and thermal spikes. RCS events have been studied in Ni_3Mn experimentally by Kirk, *et al.* [82] using thermal neutrons, for $\varepsilon \approx 20$ replacements per displacement along the $\langle 110 \rangle$ close-packed direction. This is close to efficiencies measured by Lee [7] and calculated by Averback and Diaz de la Rubia [16] for 1 MeV He^+ irradiation of Cu_3Au, 21 and 22 replacements per displacement, respectively, and is on the order of the $\varepsilon \approx 50$ replacements per displacement determined by Seidman, *et al.* [83] by field-ion microscopy of low energy (i.e. RCS dominated) cascades in W. At incident energies beyond a few tens keV, the efficiency of disordering is expected to plateau in the same manner as ion beam mixing per displacement, as higher energy events are seen to split into subcascades [16].

The high number of replacements within individual cascades leads to local disordering and zones of reduced S. Such disordered zones can be seen in dark-field TEM according to the technique described in Section 1.2.4 above, and were studied extensively by Jenkins, *et al.* [79, 84-88] in Cu_3Au and Ni_3Al to gain quantitative information on individual cascade events. In addition to providing evidence for typical cascade sizes (between about 5 nm and 15 nm) Jenkins, *et al.* documented the irregular shapes of cascades with increasing incident energy and documented the lack of correlation between subcascade formation and crystallographic direction. These observations are consistent with MD simulations results for cascades in Cu_3Au and Ni_3Al [89].

1.3.2. Rates of Ordering and Disordering

In this section, we will use the model of Zee and Wilkes [90] to explore the effects of irradiation on ordering and disordering in chemically ordered alloys. This model begins by assuming that replacement, or at least displacement, events occur at random throughout the alloy. The disordering rate can then be written as a function of the instantaneous long range order, S,

$$\left(\frac{dS}{dt}\right)_{irr} = -\varepsilon K S \tag{1.29}$$

where K is the production rate of displacements (s^{-1}). This formula is the same as deduced by Aronin [91] from experimental data in 1954.

The effects of radiation-enhanced defect populations on reordering is not so general, however. Here, Zee and Wilkes borrow the formula derived by Dienes [92] in terms of the Bragg-Williams approximation. They further modify the rate to account for radiation-enhanced defect populations and make a key assumption: that a vacancy mechanism drives reordering and interstitial motion does not affect the order of Cu_3Au. This last point was justified experimentally by Gilbert, *et al.* [93], whose observation of a lack of Stage 1 ordering in Cu_3Au has been taken to mean that interstitial Au defects are unstable and return to the lattice immediately. Modified in this way, the rate of thermal ordering may be written as,

$$\begin{aligned}\left(\frac{dS}{dt}\right)_{thermal} &= \left(Z_\alpha + Z_\beta - 2\right)\frac{\nu}{2}\frac{Z_\beta}{X_b}\exp\left(\frac{-E_m^0}{kT}\right) \\ &\times\left\{X_a X_b(1-S)^2 - [S + X_a X_b(1-S)^2]\exp\left(\frac{-V_0 S}{kT}\right)\right\}\end{aligned} \tag{1.30}$$

where Z_α is the number of α sites around a β site and Z_β is the number of β sites around an α site; ν is the vacancy jump attempt frequency; E_m^0 is the barrier to vacancy double jump; and $V_0 = -V_1/2z_1$ is the Bragg-Williams ordering "force".

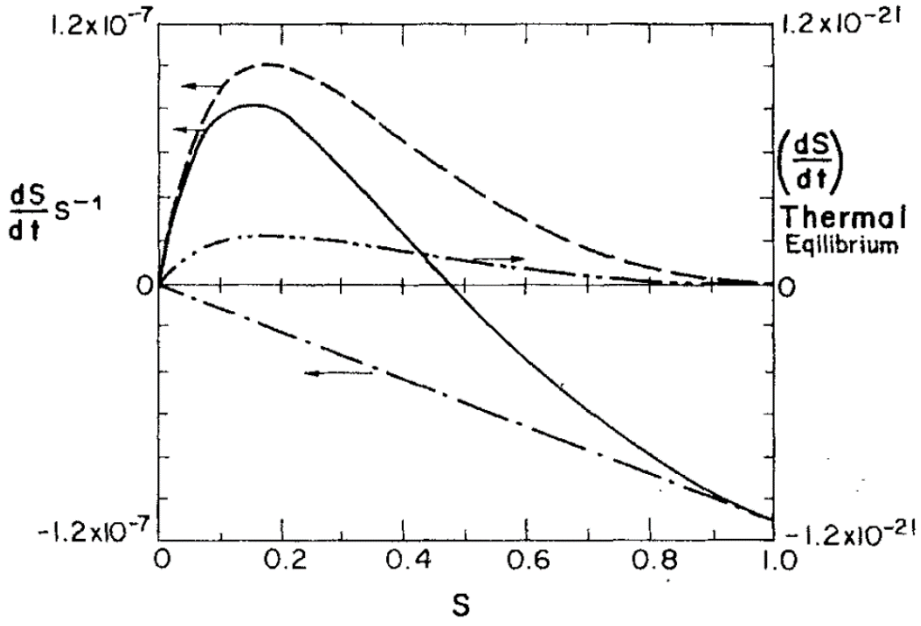

Figure 1.9: Ordering rate as a function of the long range order parameter, S, under fast neutron irradiation at 22 °C. The curves indicate: -·-·-, irradiation disordering; - - -, irradiation-enhanced ordering; ——, the overall rate; and -···-···-, thermal ordering only, for reference. The horizontal arrows indicate the relevant scale. After [90].

The net ordering rate is a balance between the radiation-induced disordering of Equation 1.29 and the thermally driven reordering of Equation 1.30, enhanced by C_v^{irr}

$$\frac{dS}{dt} = \left(\frac{dS}{dt}\right)_{irr} + \frac{C_v^{irr}}{C_v^{eq}}\left(\frac{dS}{dt}\right)_{thermal} \tag{1.31}$$

which is the true form of Equation 1.1. At temperatures near T_c the mobility of vacancy defects is high and the irradiation increase in C_v is small compared to C_v^{eq}, making thermal ordering the dominant rate. If the temperature is then lowered, radiation-enhanced ordering will become the dominant rate and that phenomenon may be observed experimentally. At sufficiently low

temperatures, however, the vacancy mobility decreases to zero, leading to the dominance of radiation-induced disordering. Similar variations in the above rates exists for S at constant temperature, as shown in Figure 1.9 for fast neutron irradiation, and can be used to find the steady state ($dS/dt = 0$) under irradiation.

1.3.3. Patterning in Driven Systems

Much experimental, theoretical, and simulation work has been done in recent decades on self-organization in dissipative systems. Often described as "patterning", this behavior involves the grouping of system components to form fixed size, fixed distribution features in response to external forcing (e.g. irradiation, extreme plastic deformation). These components in one system may be defects, such as vacancies forming small, periodic clusters on specific planes [94] or trapped gas atoms condensing into lattices bubbles [95]. In another system they may be chemical species that would decompose to separate phases at equilibrium, but are forced into a dynamically stable pattern of mixed phases by mixing within collision cascades. This latter example was a central focus for Enrique, *et al.* [96], who described in detail the interplay between thermally-activated decomposition and finite-range forced mixing. Although very different, the above cases highlight the commonly agreed upon requirement for self-organization: a bias in the production, migration, or annihilation of defects [94]. It is the systems attempt to compensate for such a bias thermally which drive the competition and thus patterning.

In the case of chemically ordered alloys, patterning of order has received less interest and only recently has our understanding of this aspect of $L1_2$ alloys begun to grow. Ni-Al alloys offer one such example. Previous studies by Nelson, *et al.* [97] and Schmitz, *et al.* [98] had shown disordering of NiAl(12 at%) and Ni_3Al alloys under room temperature irradiation, as expected. After high temperature irradiations, however, patterns of nanometer scale, ordered precipitates

were observed in the NiAl(12 at%) alloy, with no known mechanism for a patterning reaction. Recent atomistic simulations by Ye, *et al.* [99-101] in the stoichiometric alloy were finally able to identify a likely mechanism for the reaction: thermally driven nucleation of ordered anti-phase domains within sufficiently large disordered zones. Only when such zones are large enough, and their rate of production not too slow or too frequent, can new domains nucleate.

1.4. REFERENCES

[1] G. Martin and P. Bellon, "Driven Alloys," *Solid State Physics,* vol. 50, pp. 189-327, 1996.

[2] S. W. Chee, B. Stumphy, N. Q. Vo, R. S. Averback, and P. Bellon, "Dynamic self-organization in Cu alloys under ion irradiation," *Acta Materialia,* vol. 58, pp. 4088-4099, 2010.

[3] R. A. Enrique, K. Nordlund, R. S. Averback, and P. Bellon, "Nonequilibrium self-organization in alloys under irradiation leading to the formation of nanocomposites," *Nuclear Instruments and Methods in Physics Research Section B: Beam Interactions with Materials and Atoms,* vol. 202, pp. 206-216, 2003.

[4] R. Lokesh, P. Bellon, and R. S. Averback, "Nanostructuring of Cu-TiB_2 induced by ion irradiation," *Journal of Nuclear Materials,* vol. 423, pp. 9-15, 2012.

[5] X. Zhang, J. A. Beach, M. Wang, P. Bellon, and R. S. Averback, "Precipitation kinetics of dilute Cu-W alloys during low-temperature ion irradiation," *Acta Materialia,* vol. 120, pp. 46-55, 2016.

[6] X. Zhang, J. Wen, P. Bellon, and R. S. Averback, "Irradiation-induced selective precipitation in Cu–Nb–W alloys: An approach towards coarsening resistance," *Acta Materialia,* vol. 61, pp. 2004-2015, 2013.

[7] Y. S. Lee, "Atomic transport mechanisms in irradiated Cu_3Au," Doctor of Philosophy, Physics, University of Illinois at Urbana-Champaign, Urbana, Illinois, 1996.

[8] E. A. Lang, "Radiation Damage and Radiation Induced Order-Disorder Transformations in Cu_3Au," Master of Science, Materials Science and Engineering, University of Illinois at Urbana-Champaign, Urbana, Illinois, 2000.

[9] J. A. Brinkman, "On the Nature of Radiation Damage in Metals," *Journal of Applied Physics,* vol. 25, p. 961, 1954.

[10] J. S. Koehler and F. Z. Seitz, "Radiation disarrangement of crystals," *Zeitschrift für Physik,* vol. 138, pp. 238-245, 1954.

[11] G. H. Kinchin and R. S. Pease, "The displacement of atoms in solids by radiation," *Reports on Progress in Physics,* vol. 18, 1955.

[12] A. Seeger, *Proceedings of the 2nd UN International Conference on Peaceful Uses of Atomic Energy,* vol. 6, 1958.

[13] J. B. Gibson, A. N. Goland, M. Milgram, and G. H. Vineyard, "Dynamics of Radiation Damage," *Physical Review,* vol. 120, pp. 1229-1253, 1960.

[14] M. Nastasi, J. Mayer, and J. Hirvonen, *Ion-Solid Interactions: Fundamentals and Applications,* 1996.

[15] G. S. Was, *Fundamentals of Radiation Materials Science*: Springer Science+Business Media, 2007.

[16] R. S. Averback and T. Diaz de la Rubia, "Displacement damage in irradiated metals and semiconductors," *Solid State Physics,* vol. 51, p. 281, 1998.

[17] P. Ehrhart, W. Schilling, and H. Ullmaier, "Radiation Damage in Crystals," in *Encylopedia of Applied Physics,* ed: WILEY-VCH Verlag GmbH & Co KGaA, 2003, pp. 429-457.

[18] M. J. Norgett, M. T. Robinson, and I. M. Torrens, "A proposed method of calculating displacement dose rate," *Nuclear Engineering and Design,* vol. 33, pp. 50-54, 1975.

[19] G. H. Kinchin and R. S. Pease, "The mechanism of the irradiation disordering of alloys," *Journal of Nuclear Energy,* vol. 1, pp. 200-202, 1955.

[20] P. Sigmund, "Energy density and time constant of heavy-ion-induced elastic-collision spikes in solids," *Applied Physics Letters,* vol. 25, p. 169, 1974.

[21] R. S. Averback, M. Ghaly, and H. Zhu, "Defect Production Mechanisms During keV Ion Irradiation: Results of Computer Simulations," *MRS Proceedings,* vol. 373, 1994.

[22] T. Diaz de la Rubia, R. S. Averback, R. Benedek, and W. E. King, "Role of thermal spikes in energetic displacement cascades," *Phys Rev Lett,* vol. 59, pp. 1930-1933, Oct 26 1987.

[23] R. S. Averback, T. Diaz de la Rubia, and R. Benedek, "Dynamics and structure of energetic displacement cascades," *Nuclear Instruments and Methods in Physics Research B,* vol. 33, pp. 693-700, 1988.

[24] T. Diaz de la Rubia, R. S. Averback, H. Hsieh, and R. Benedek, "Molecular dynamics simulation of displacement cascades in Cu and Ni: Thermal spike behavior," *Journal of Materials Research,* vol. 4, pp. 579-586, 1989.

[25] A. J. E. Foreman, W. J. Phythian, and C. A. English, "The molecular dynamics simulation of irradiation damage cascades in copper using a many-body potential," *Philosophical Magazine A,* vol. 66, pp. 671-695, 1992.

[26] M. W. Thompson and R. S. Nelson, "Evidence for heated spikes in bombarded gold from the energy spectrum of atoms ejected by 43 keV A^+ and Xe^+ ions," *Philosophical Magazine,* vol. 7, pp. 2015-2026, 1962.

[27] P. Sigmund, "Mechanisms and theory of physical sputtering by particle impact," *Nuclear Instruments and Methods in Physics Research B,* vol. 27, pp. 1-20, 1987.

[28] J. L. Klatt, R. S. Averback, and D. Peak, "Ion beam mixing in Ag-Pd alloys," *Applied Physics Letters,* vol. 55, p. 1295, 1989.

[29] I. Koponen and M. Hautala, "High energy ion beam mixing in dense collision cascades," *Nuclear Instruments and Methods in Physics Research B,* vol. 69, pp. 182-192, 1992.

[30] H. Zhu, R. S. Averback, and M. Nastasi, "Molecular dynamics simulations of a 10 keV cascade in β-NiAl," *Philosophical Magazine A,* vol. 71, pp. 735-758, 1995.

[31] R. S. Averback, R. Benedek, and K. L. Merkle, "Ion-irradiation studies of the damage function of copper and silver," *Physical Review B,* vol. 18, pp. 4156-4171, 1978.

[32] D. J. Bacon, in *Computer simulation in materials science : nano/meso/macroscopic space & time scales*, H. O. Kirchner, L. P. Kubin, and V. Pontikis, Eds., ed Dordrecht: Kluwer Academic Publishers, 1996, p. 189.

[33] R. S. Averback, "Atomic displacement processes in irradiatied metals," *Journal of Nuclear Materials,* vol. 216, pp. 49-62, 1994.

[34] A. J. E. Foreman, C. A. English, and W. J. Phythian, "Molecular dynamics calculations of displacement threshold energies and replacement collision sequences in copper using a many-body potential," *Philosophical Magazine A,* vol. 66, pp. 655-669, 1992.

[35] R. S. Averback and K. L. Merkle, "Radiation-annealing effects in energetic displacement cascades," *Physical Review B,* vol. 16, pp. 3860-3869, 1977.

[36] T. Diaz de la Rubia and W. J. Phythian, "Molecular dynamics studies of defect production and clustering in energetic displacement cascades in copper," *Journal of Nuclear Materials,* vol. 191-194, pp. 108-115, 1992.

[37] F. Gao and D. J. Bacon, "Molecular dynamics study of displacement cascades in Ni_3Al: I. General features and defect production efficiency," *Philosophical Magazine A,* vol. 71, pp. 43-64, 1995.

[38] F. Gao and D. J. Bacon, "Molecular dynamics study of displacement cascades in Ni_3Al: II. Kinetics, disordering and atomic mixing," *Philosophical Magazine A,* vol. 71, pp. 65-84, 1995.

[39] R. S. Averback, R. Benedek, K. L. Merkle, J. Sprinkle, and L. J. Thompson, "Defect production in ion-irradiated aluminum," *Journal of Nuclear Materials,* vol. 113, pp. 211-218, 1983.

[40] L. C. Wei, E. Lang, C. P. Flynn, and R. S. Averback, "Freely migrating defects in ion-irradiated Cu_3Au," *Applied Physics Letters,* vol. 75, p. 805, 1999.

[41] R. Sizmann, "The Effect of Radiation Upon Diffusion in Metals," *Journal of Nuclear Materials,* vol. 69 & 70, pp. 386-412, 1978.

[42] Y. S. Lee, C. P. Flynn, and R. S. Averback, "Thermal and radiation-enhance diffusion in Cu_3Au," *Physical Review B,* vol. 60, pp. 881-889, 1999.

[43] W. A. Soffa and D. E. Laughlin, "Diffusional Phase Transformations in the Solid State," in *Physical Metallurgy*, D. E. Laughlin and K. Hono, Eds., 5 ed: Elsevier, 2014, pp. 851-1020.

[44] F. C. Nix and W. Shockley, "Order-Disorder Transformations in Alloys," *Reviews of Modern Physics,* vol. 10, pp. 1-72, 1938.

[45] L. Guttman, "Order-disorder phenomena in metals," *Solid State Physics,* vol. 3, pp. 145-223, 1956.

[46] T. Muto and Y. Takagi, "The theory of order-disorder transtitions in alloys," *Solid State Physics,* vol. 1, pp. 193-282, 1955.

[47] G. Tammann, "Die chemischen und galvanischen Eigenscagten von Mischkristallrein und ihre Atomverteilung," *Zeitschrift für anorganische und allgemeine Chemie*, vol. 107, pp. 1-239, 1919.

[48] N. Kurnakow, S. Zemczuzny, and M. Zasedatelev, "The transformations in alloys of gold with copper," *Journal of the Institute of Metals,* vol. 15, pp. 305-331, 1916.

[49] E. C. Bain, "Crystal structure of solid solutions," *Transactions of the American Institute of Mining Engineers,* vol. 68, pp. 625-639, 1923.

[50] C. H. Johansson and J. O. Linde, "X-ray determination of the atomic structure of the Au-Cu and Pd-Cu mixed crystal series," *Annalen der Physik,* vol. 78, pp. 439-460, 1925.

[51] W. L. Bragg and E. J. Williams, "The effect of thermal agitation on atomic arrangement in alloys. I," *Proceedings of the Royal Society of London. Series A: Mathematical, Physical and Engineering Sciences,* vol. 145, pp. 699-730, 1934.

[52] W. L. Bragg and E. J. Williams, "The effect of thermal agitation on atomic arrangement in alloys. II," *Proceedings of the Royal Society of London. Series A: Mathematical, Physical and Engineering Sciences,* vol. 151, pp. 540-566, 1935.

[53] E. J. Williams, "The effect of thermal agitation on atomic arrangement in alloys. III," *Proceedings of the Royal Society of London. Series A: Mathematical, Physical and Engineering Sciences,* vol. 152, pp. 231-252, 1935.

[54] Z. W. Wilchinsky, "X-Ray Measurement of Order in the Alloy Cu_3Au," *Journal of Applied Physics,* vol. 15, p. 806, 1944.

[55] T. Muto, *Scientific Papes of the Institute of Physical and Chemical Research (Tokyo),* vol. 30, 1936.

[56] L. Nordheim, "Zur Elektronentheoric der Metalle. II," *Annalen der Physik,* vol. 401, pp. 641-678, 1931.

[57] H. A. Bethe, "Statistical theory of superlattices," *Proceedings of the Royal Society A: Mathematical, Physical and Engineering Sciences,* vol. 150, pp. 552-575, 1935.

[58] J. M. Cowley, "An Approximate Theory of Order in Alloys," *Physical Review,* vol. 77, pp. 669-675, 1950.

[59] J. M. Cowley, "X-Ray Measurement of Order in Single Crystals of Cu_3Au," *Journal of Applied Physics,* vol. 21, p. 24, 1950.

[60] P. Ehrenfest, "Phasenumwandlungen im ueblichen und erweiterten Sinn, classifiziert nach dem entsprechenden Singularitaeten des thermodynamischen Potentiales," *Verhandlingen der Koninklijke Akademie van Wetenschappen,* vol. 36, pp. 153-157, 1933.

[61] E. Ising, "Contribution to the theory of ferromagnetism," *Zeitschrift für Physik,* vol. 31, 1925.

[62] R. C. Tolman, *The Principles of Statistical Mechanics*. New York: Dover Publications, Inc., 1938.

[63] L. D. Fosdick, "Calculation of Order Parameters in a Binary Alloy by the Monte Carlo Method," *Physical Review,* vol. 116, pp. 565-573, 1959.

[64] K. Binder, J. L. Lebowitz, M. K. Phani, and M. H. Kalos, "Monte Carlo study of the phase diagrams of binary alloys with face centered cubic lattice structure," *Acta Metallurgica,* vol. 29, pp. 1655-1665, 1981.

[65] K. Binder, "Monte Carlo Simulation of Alloy Phase Diagrams and Short-Range Order," in *Atomic Transport and Defects in Metals by Neutron Scattering*, C. Janot, W. Petry, D. Richter, and T. Springer, Eds., ed: Springer-Verlag Berlin Heidelberg, 1986, pp. 12-16.

[66] K. Binder, "Monte Carlo study of entropy for face-centered cubic Ising antiferromagnets," *Zeitschrift für Physik B - Condensed Matter,* vol. 45, pp. 61-69, 1981.

[67] K. Binder, "Monte Carlo simulations of alloy phase transformations," in *Statics and Dynamics of Alloy Phase Transformations*, P. E. A. Turchi and A. Gonis, Eds., ed New York: Plenum Press, 1994, pp. 467-.

[68] M. Athènes and P. Bellon, "Antisite-assisted diffusion in the $L1_2$ ordered structure studied by Monte Carlo simulations," *Philosophical Magazine A,* vol. 79, pp. 2243-2257, 1999.

[69] M. Kessler, W. Dieterich, and A. Majhofer, "Ordering kinetics in an fcc A_3B binary alloy model: Monte Carlo studies," *Physical Review B,* vol. 67, 2003.

[70] C. Frontera, E. Vives, T. Casta`n, and A. Planes, "Monte Carlo study of the growth of $L1_2$-ordered domains in fcc A_3B binary alloy," *Physical Review B,* vol. 55, pp. 212-225, 1997.

[71] C. Sykes and F. W. Jones, "The atomic rearrangement process in the copper-gold alloy Cu_3Au," *Proceedings of the Royal Society of London. Series A, Mathematical and PhysicalSciences,* vol. 157, pp. 213-233, 1936.

[72] A. J. C. WIlson, "The reflexion of X-rays from the 'anti-phase nuclei' of $AuCu_3$," *Proceedings of the Royal Society A: Mathematical, Physical and Engineering Sciences,* vol. 181, pp. 360-368, 1943.

[73] D. B. Williams and C. B. Carter, *Transmission Electron Microscopy: A Textbook for Materials Science,* 2 ed. New York: Springer Science+Business Media, 2009.

[74] R. M. Fisher and M. J. Marcinkowski, "Direct observation of antiphase boundaries in the $AuCu_3$ superlattice," *Philosophical Magazine,* vol. 6, pp. 1385-1405, 1961.

[75] P. B. Hirsch, "Periodic and Ordered Structures," in *Electron Microscopy of Thin Crystals,* ed: Krieger Pub Co, 1965, p. 563.

[76] S. Ogawa, D. Watanabe, H. Watanabe, and T. Komoda, "The direct observation of the long period of the ordered alloy CuAu(II) by means of electron microscope," *Acta Crystallographica,* vol. 11, pp. 872-875, 1958.

[77] G. J. C. Carpenter and E. M. Schulson, "The Disordering of Zr_3Al by 1 MeV Electron Irradiation," *Journal of Nuclear Materials,* vol. 23, pp. 180-189, 1978.

[78] F. Z. Seitz, "On the disordering of solids by action of fast massive particles," *Discussions of the Faraday Society,* vol. 5, pp. 271-282, 1949.

[79] M. L. Jenkins and M. Wilkens, "Transmission electron microscopy studies of displacement cascads in Cu_3Au: II. Experimental investigation of cascades produced by Cu ions," *Philosophical Magazine,* vol. 34, pp. 1155-1167, 1976.

[80] E. M. Schulson, "The ordering and disordering of solid solutions under irradiation," *Journal of Nuclear Materials,* vol. 83, pp. 239-264, 1979.

[81] T. L. Daulton, M. A. Kirk, and L. E. Rehn, "In-situ transmission electron microscopy study of ion-irradiated copper: Temperature dependence of defect yield and cascade collapse," *Philosophical Magazine A,* vol. 80, pp. 809-842, 2000.

[82] M. A. Kirk, T. H. Blewitt, and T. L. Scott, "Irradiation disordering of Ni_3Mn by replacement collision sequences," *Physical Review B,* vol. 15, pp. 2914-2922, 1977.

[83] L. A. Beavan, R. M. Scanlan, and D. N. Seidman, "The defect structure of depleted zones in irradiated tungsten," *Acta Metallurgica,* vol. 19, pp. 1339-1350, 1971.

[84] C. A. English and M. L. Jenkins, "Characterization of displacement cascade damage produced in Cu_3Au by fast-particle irradiation," *Journal of Nuclear Materials,* vol. 96, pp. 341-357, 1981.

[85] C. A. English, M. L. Jenkins, and M. A. Kirk, "Characterization of displacement cascade damage in Cu_3Au produced by fusion-neutron irradiation," *Journal of Nuclear Materials,* vol. 103 & 104, pp. 1337-1342, 1981.

[86] M. L. Jenkins, K.-H. Katerbau, and M. Wilkens, "Transmission electron microscopy studies of displacement cascads in Cu_3Au: I. The diffraction contrast of disordered zones," *Philosophical Magazine,* vol. 34, pp. 1141-1153, 1976.

[87] M. L. Jenkins, N. G. Norton, and C. A. English, "Transmission–electron–microscopy studies of displacement cascades in Cu_3Au Cascades produced by 100–200 keV Cu^{+w} ions," *Philosophical Magazine A,* vol. 40, pp. 131-136, 1979.

[88] T. M. Robinson and M. L. Jenkins, "Heavy-ion irradiation of nickel and nickel alloys," *Philosophical Magazine A,* vol. 43, pp. 999-1015, 2006.

[89] T. Diaz de la Rubia, A. Caro, and M. Spaczer, "Kinetics of radiation-induced disordering of A_3B intermetallic compounds: A molecular-dynamics-simulation study," *Physical Review B,* vol. 47, 1993.

[90] R. Zee and P. Wilkes, "The radiation-induced order-disorder transformation in Cu_3Au," *Philosophical Magazine A,* vol. 42, pp. 463-482, 1980.

[91] L. R. Aronin, "Radiation Damage Effects on Order-Disorder in Nickel-Manganese Alloys," *Journal of Applied Physics,* vol. 25, p. 344, 1954.

[92] G. J. Dienes, "Kinetics of order-disorder transformations," *Acta Metallurgica,* vol. 3, pp. 549-557, 1955.

[93] J. Gilbert, H. Herman, and A. C. Damask, "Electron irradiation of Cu_3Au," *Radiation Effects,* vol. 20, pp. 37-42, 1973.

[94] W. Jäger, P. Ehrhart, and W. Schilling, "Microstructural evolution in metals during helium and proton irradiations," *Radiation Effects and Defects in Solids,* vol. 113, pp. 201-211, 1990.

[95] P. B. Johnson, *Fundamental Aspects of Inert Gases in Solids*. New York: Plenum Press, 1991.

[96] R. A. Enrique and P. Bellon, "Compositional patterning in systems driven by competing dynamics of different length scales," *Physical Review Letters,* vol. 84, pp. 2885-2888, 2000.

[97] R. S. Nelson, J. A. Hudson, and D. J. Mazey, "The stability of precipitates in an irradiation environment," *Journal of Nuclear Materials,* vol. 44, pp. 318-330, 1972.

[98] G. Schmitz, J. C. Ewert, F. Harbsmeier, M. Uhrmacher, and F. Haider, "Phase stability of decomposed Ni-Al alloys under ion irradiation," *Physical Review B,* vol. 63, 2001.

[99] J. Ye and P. Bellon, "Nanoscale patterning of chemical order induced by displacement cascades in irradiated alloys. I. A kinetic Monte Carlo study," *Physical Review B,* vol. 70, 2004.

[100] J. Ye and P. Bellon, "Nanoscale patterning of chemical order induced by displacement cascades in irradiated alloys. II. Analytical modeling," *Physical Review B,* vol. 70, 2004.

[101] J. Ye, Y. Li, R. Averback, J.-M. Zuo, and P. Bellon, "Atomistic modeling of nanoscale patterning of $L1_2$ order induced by ion irradiation," *Journal of Applied Physics,* vol. 108, p. 054302, 2010.

CHAPTER 2

IN SITU IRRADIATION OF Cu_3Au

As discussed in the preceding chapter, *in situ* resistivity studies of Lee [1] and Lang [2] indicate surprising and yet unexplained variation in the initial disordering of Cu_3Au under light ion irradiation as temperatures approach the thermal order-disorder transition at $T_c \approx 390$ °C. The significance of these variations, however, is obscured by systematic underestimation of order by resistivity over the same range of temperatures. A mathematical examination of this behavior, detailed in the following text, predicts overestimation of disordering comparable in size to the observed variations and requiring verification by an alternative technique. In this chapter, we thus investigate the effect by *in situ* electron diffraction and microscopy, gauging the efficacy of the methods for analysis of chemical order and radiation damage. This approach presents a number of advantages through direct observation of microstructural evolution of specimens under increasing radiation damage dose, in particular the size and behavior of anti-phase ordered domains and boundaries. The approach required the use of electron transparent Cu_3Au foils, the thickness of which was optimized to balance needs for large thinned areas, mechanical stability under irradiation, and clear imaging contrast from order. Such foils were prepared on campus at the Center for Microanalysis of Materials (CMM) [3] at the Frederick Seitz Materials Research Laboratory and then irradiated and characterized *in situ* at the Intermediate Voltage Electron Microscope – Tandem Accelerator Facility (IVEM) [4] at Argonne National Laboratory according to two plans of study: 1) to examine rates of disordering through electron diffraction analysis; and 2) to observe the nature of damage and the evolution of the ordered microstructure by dark-field imaging.

2.1. MICROSCOPY SPECIMEN PREPARATION

Due to concerns with damage artifacts [5], implanted gallium, reduced thermal conductivity, and mechanical instability in focused ion beam produced lift-out specimens, the foil specimens for the present work were produced from bulk by traditional transmission electron microscopy (TEM) preparation techniques. Raw material disks 3 mm in diameter and 0.25 mm in thickness were cut from bulk Cu_3Au of known stoichiometric composition using electrical discharge machining (EDM). Following EDM, these disks were heat treated to improve their microstructures, mechanically thinned to remove mechanical damage, and ion milled for electron transparency.

2.1.1. Heat Treatment

A pair of heat treatments were carried out to better adapt the specimens to the needs of the present work, before reducing the raw specimen disks to electron transparent foils. As discussed in the previous chapter, the quality of diffraction contrast from ordered domains declines with increasing overlap of grains through the foil thickness. The specimen disks were thus annealed at a high temperature to reduce such overlap and increase the number of visible ordered domains per grain studied. Consideration was paid, in particular, to the potential limiting of testable sites if overly large grains resulted in the final electron transparent area containing only a small number of grains. Consequently, the as prepared samples, with 0.2-1.0 μm grain size, were annealed at 800 °C for 60 minutes. This resulted in a final grain sizes of 5 μm and beyond. All high temperature heat treatments were carried out in a tube furnace pressurized with Ar-H(5 at%) forming gas to 1 atm; the H_2 component is used to reduce any formation of CuO_2.

The second heat treatment was employed to prevent overlap between ordered domains in the final specimen foils; this required ordered domain sizes in excess of 200 nm diameter. As

discussed in the previous chapter, the coarsening of ordered domains in Cu_3Au is dominated by the movement of flat, conserved anti-phase boundaries, once the disordered phase has been fully consumed, and is thus significantly slowed. This made reducing the population of initial ordered nuclei essential to achieve well-ordered specimen foils without extreme annealing times. The specimen disks were first heated to 400 °C to erase the ordered microstructure formed on cooling from the previous heat treatment. After a short soak to stabilize the furnace temperature, the specimen disks were cooled to 385 °C over a 10 day period in order to minimize undercooling at the onset of nucleation and thus reduce the final population of ordered domains. The treatment was found to produce anti-phase domains on the order of 0.1-0.5 μm. Practical limitations on time and forming gas supply prevented use of the tube furnace for the ordering heat treatment. Instead, specimen disks were sealed in glass ampules filled to 0.3 atm of the same Ar-H(5 at%) mixture.

2.1.2. Mechanical Thinning

With grain and ordered domain microstructures suitable to the present work, the specimen disks were next thinned mechanically by a two stage polishing and dimpling process. Polishing was largely performed using a semiautomatic MultiPrep™ polishing system from Allied High Tech Products, with Crystalbond™ 509 thermal adhesive for specimen mounting and cold water to rinse debris from the polishing platter. To provide a flat reference surface for later thinning steps, a thickness of approximately 10-30 μm was first removed from the specimen disks using a 9 μm diamond lapping film. The specimen disks were then turned over and polished to half the original thickness (typically a depth of 100-150 μm) with a succession of 30, 9, 3, and 1 μm diamond lapping films. (Polishing stages with the 30 μm and 9 μm films were performed at 60 rpm with a 200 g load, while smaller grits were performed at 30 rpm with a 50 g load.) This finely polished surface was finished by hand on a MetaServ® 250 grinder-polisher from Buehler using a

50 nm alumina suspension on a cloth pad. Special care was taken to clean the specimen disks and polishing fixture of grit and debris between stages using deionized water, with the specimen disks further cleaned by sonication in acetone and isopropanol before each thickness measurement.

The polished specimen disks, now 100-150 μm thick, were further thinned using a Model 656 Dimple Grinder from Gatan. In the present work, specimen disks were mounted using the same thermal adhesive as for polishing and dimpled from the less polished surface. Dimpling began with a 15 mm diameter phosphor bronze grinding wheel and 4-6 μm CBN paste, thinning the specimen to a center thickness of 30-40 μm over approximately 30 minutes. This was followed by dimpling with a pair of 15 mm diameter felt polishing pads, the first coated in the same 4-6 μm CBN paste and the second in a 0-2 μm CBN paste. (All dimpling stages were carried out with a 10 g load and a medium wheel speed.) Although Gatan recommends a final dimpled thickness of less than 10 μm [6], specimens prepared to that standard proved very fragile; the dimpled specimen disks were thus thinned to 15-25 μm. While the specimens were too thin for sonication, care was still taken to clean the specimen disk and mounting fixture between dimpling stages using deionized water, ethanol, and a gentle swabbing with cotton.

2.1.3. Ion Milling

With the bulk of the treated material removed, the specimen disks were finally thinned to electron transparency. Electropolishing techniques were ultimately rejected in favor of ion milling for this stage of preparation, because both acetic-chromic acid [7] and cyanide [8] chemistries capable of etching copper and gold at comparable rates raised safety concerns relative to the well-developed ion milling instruments available in the CMM facility. For the milling times used in the present work (1-4 hours), typical forms of damage include the amorphization of surface layers and the introduction of point defects and accompanying dislocation loops [5].

Ion milling of the specimen disks was carried out in a Model 691 Precision Ion Polishing System (PIPS) from Gatan. The PIPS system is a dual gun mill offering Ar^+ ions at accelerating voltages of 0.1-6.0 keV and individually adjustable incident angles up to ±10°, relative to the specimen surface. Onboard electronics allow the mill to be run in either continuous or modulated modes, and an assortment of specimen posts allow milling to be limited by surface and direction. Foils for the current study were milled simultaneously from the dimpled and polished surfaces to prevent redeposition of sputtered material and to ensure that electron transparent regions fell outside any remaining damage layers from polishing and dimpling. Milling proceeded in three stages: 1) to thin the dimpled center to the point of breakthrough (7°/-5°, 5 keV); 2) to widen or create additional breakthroughs if only a small number of grains would be sampled by the first (5°/-3°, 2.5 keV); and 3) remove surface damage from the preceding stages (5°/-3°, 0.5 keV).

Of the three stages, the second proved most critical for balancing testable, electron transparent area and mechanical stability in the final foils. The large grain sizes produced by earlier heat treatments were found, as expected, to reduce the number of grains available for imaging. Enhanced milling was observed along grain boundaries, requiring at least some widening of all initial breakthroughs. While conventional wisdom holds that milling should be halted soon after penetration to preserve an ideal, fringed edge, such protrusions were found to bend considerably throughout heating and irradiation. Instead, milling was prolonged during the second stage to deliberately blunt edges, producing saw-tooth edges with reduced thin area but improved mechanical stability. Such edges were found to thicken on the order of 0.15 nm per nm distance from the breakthrough. Because practical limitations on metal sputtering in our PIPS prevented specimen cooling with liquid nitrogen, special care was taken to observe TEM foils for defects loops and thermal disordering before *in situ* experimentation.

2.2. EXPERIMENTAL DESIGN

2.2.1. Alignment

The diffraction and imaging studies described in the following sections were conducted using a Model 652 double-tilt, heating stage from Gatan. The temperature measurement of the stage was tested by the IVEM staff to be accurate to ~5 °C. This particular heating holder, however, is known to experience unpredictable shifts in temperature when the secondary, "y", tilt is used. Alignments for both studies thus began with a search for grains oriented near zone axes containing $g = \langle 100 \rangle$ or $g = \langle 110 \rangle$ superlattice reflections, with preference for those with superlattice reflections aligned along the primary, "x", tilt. Such grains proved ideal for irradiations at temperature, as minor bending of the specimen could be countered by adjusting only the primary tilt. Once a suitably oriented grain was located and the zone axis aligned, the foil was tilted normal to the desired superlattice vector to produce a systematic row, shown in Figure 2.1, of fundamental

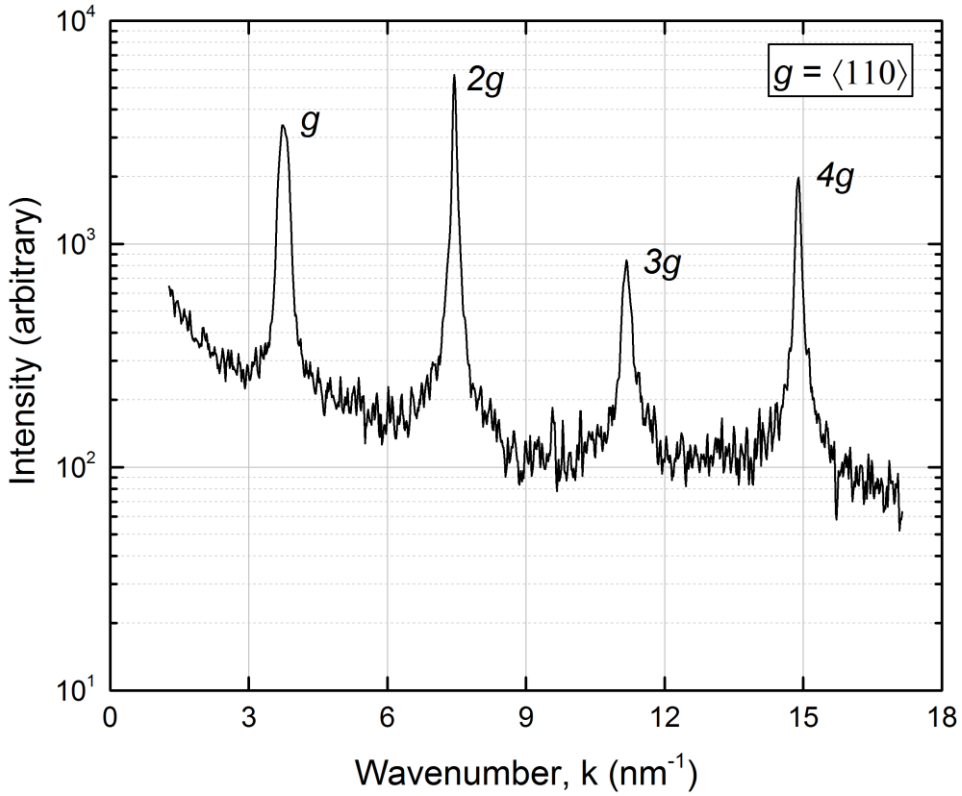

Figure 2.1: Diffracted intensities along a $g = \langle 110 \rangle$ systematic row at 370 °C.

(even g) and superlattice (odd g) reflections. Foils for dark-field observation were then tilted by small amounts to account for local bending of the imaged area, while foils for electron diffraction analysis required additional alignment.

The foils used for electron diffraction analysis were further aligned using a two-step tilting procedure akin to setting the popular weak-beam imaging condition. First, the specimen was tilted to excite the $2g$ fundamental reflection (i.e. aligning the reflection and the transmitted beam with the $2g$ Kikuchi lines). This was followed by shifting the transmitted beam to the $-1.5g$ position using the dark-field beam tilt. The resulting alignment placed the $2g$ fundamental and $3g$ superlattice reflections at positions of equal excitation error [5], as observed by their location within the original $2g$ Kikuchi lines. It is sufficient here to note that this condition removes orientation based considerations from a comparison of the relative intensities of the $2g$ and $3g$ reflections, making these ideal for the type of long range order analysis described in the previous

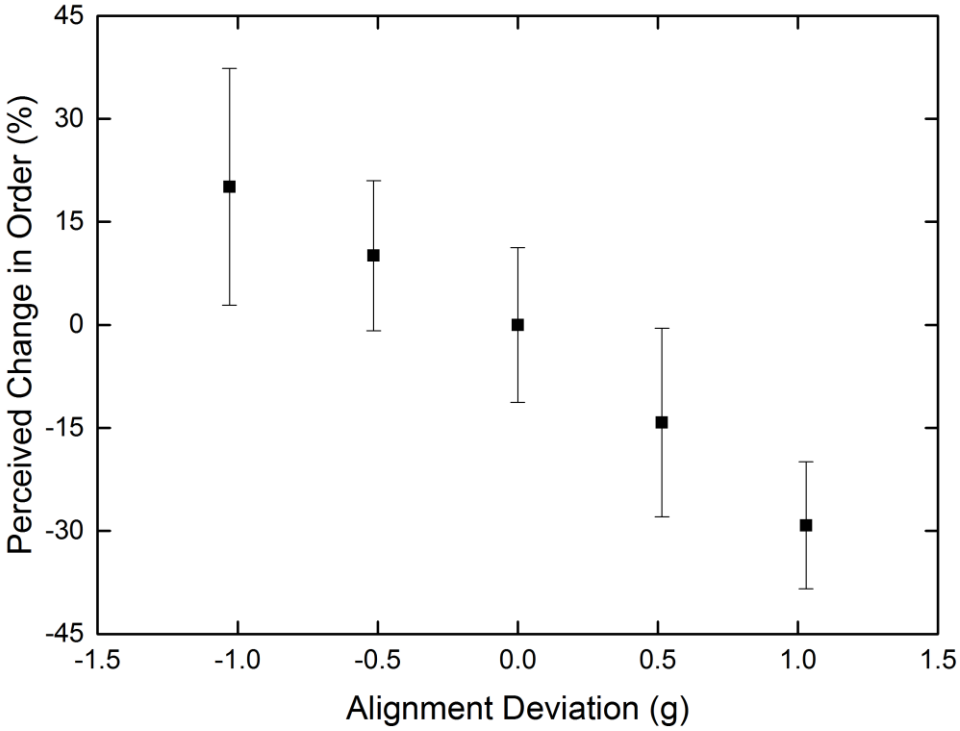

Figure 2.2: Deviation in perceived S as a function of deviation from the $2g$-$3g$ alignment.

chapter. The relative deviation in such measurements as a function of misalignment is presented in Figure 2.2 based on room temperature measurements of ordered foils. While the deviations shown here are large, it is important to note that all experiments in the present work were kept carefully aligned within $\pm 0.50g$ in the extremes and within $\pm 0.25g$ ideally.

2.2.2. Irradiation

The present *in situ* ion irradiations were carried out using 500 keV Ne^+ at the IVEM facility. Neon was selected to provide: 1) best comparison to previous works [1, 2]; 2) higher production of freely migrating point defects relative to heavier ions (e.g. Kr^+) [9]; and 3) significantly higher dose rates than He^+ beams. The 500 keV accelerating voltage was chosen to create a nearly homogeneous distribution of collisions across the thickness of our specimen foils, as illustrated by the SRIM [10] calculation plotted in Figure 2.3. The beam current was measured using an annular

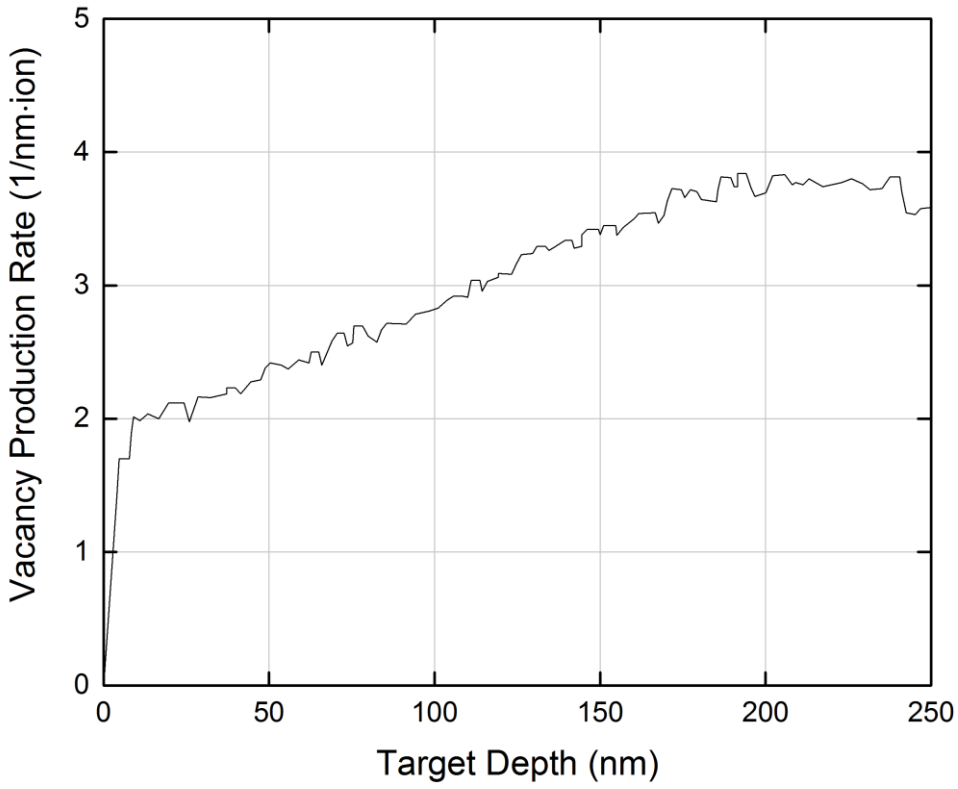

Figure 2.3: Profiles of vacancy production per collision vs. depth in foil, as predicted by the SRIM software package using a modified Kinchin-Pease formula.

Faraday cup before entering the Hitachi 9000 TEM at an angle of 30° relative to the electron column. This shallow entry angle and the 1.5 mm diameter beam formed by the Faraday cup provided a window of 10°-40° primary tilt for the alignments described above. Dose rates, $\dot{\phi}$, for the present work ranged between 1×10^{-5} and 5×10^{-4} dpa/s (3.3×10^{10} and 1.5×10^{12} ions/cm^{2}s).

2.2.3. Post-Processing

While dark-field recordings were immediately available for analysis, further processing was required to extract long range order information from recorded electron diffraction spectra. Recordings were first rendered frame-by-frame as image sequences using the Adobe After Effects software package [11]. These image sequences were then feed into a custom MATLAB [12] script (included as Appendix A.1) for digitization, background subtraction, and peak area calculation.

2.3. DIFFRACTION ANALYSIS OF DISORDER

2.3.1. Thermal Behavior of Cu_3Au

The accuracy of our diffraction method was checked by measuring the temperature dependence of the long range order parameter, S, of Cu_3Au and comparing these results with prior works. Measurements of such equilibrium states of order are presented in Figure 2.4 for each of the main irradiation temperatures tested, alongside X-ray diffraction based measurements (Cowley [13] and Warren [14]) and theoretical models (Cowley [15] and Bragg [16, 17]) from the literature. Data from the present work are consistent with these prior studies and are seen to generally agree with the model put forward by Cowley. Measurements by electrical resistivity (Sykes [18] and Lee [1]) over the same range of temperatures are shown in Figure 2.5 for comparison. While both diffraction and resistivity based tests reproduce the expected downward trend in S on approaching

the order-disorder transition, resistivity based values are seen to more sharply decay just below T_c compared to diffraction measurements.

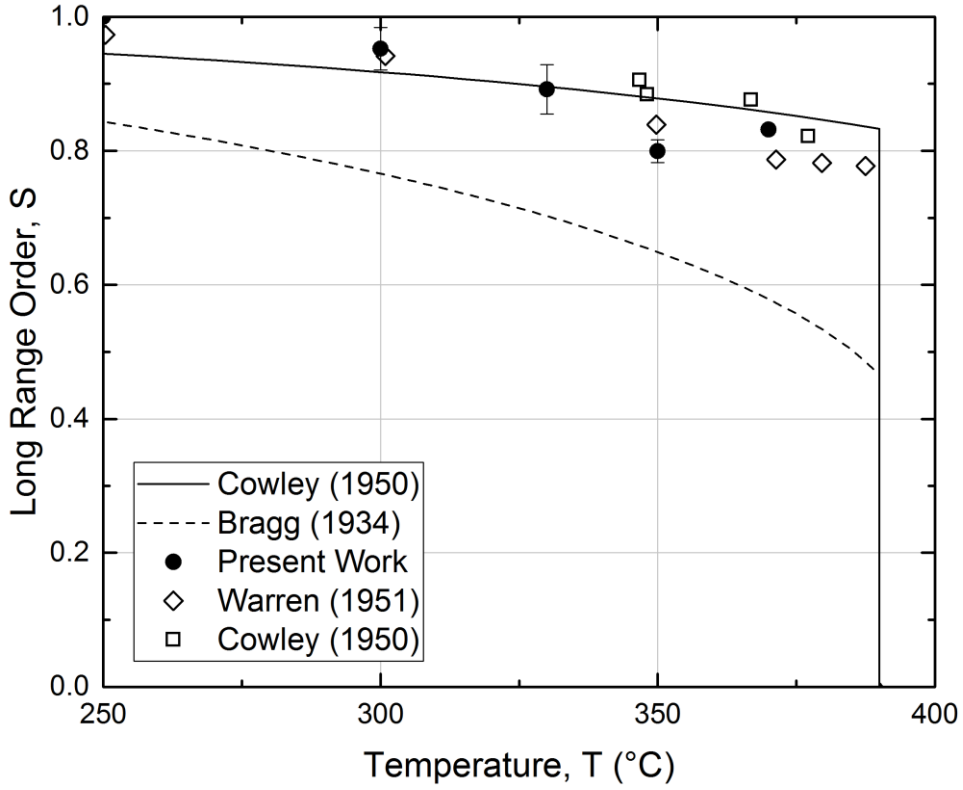

Figure 2.4: Equilibrium long range order as a function of temperature, measured by electron (present) and X-ray diffraction (Cowley and Warren). Curves for the theories of order described by Bragg and Cowley are provided for reference.

The observed discrepancy between equilibrium order measurements using electrical resistivity and those using diffraction techniques is especially important for the present work, as such differences result in over or underestimation of disordering rates, $dS/Sd\phi$, when comparing techniques. This effect is best demonstrated by comparing the resistivity data of Lee with the theoretical model described by Cowley. Taking the Cowley model for S as our point of reference, the measured order reported by Lee can then be described by $S_m = Sf(S)$, where $f(S)$ is some unknown scaling function. The ratio, R, by which the measured disordering rate over or underestimates that of the reference S can then be derived as follows,

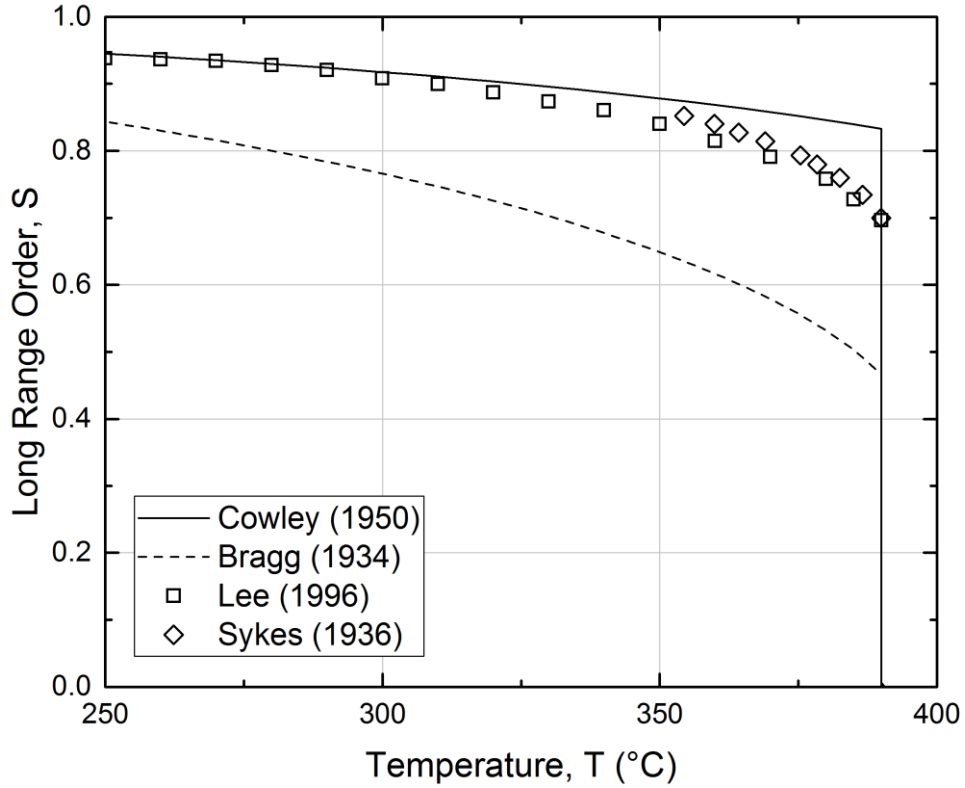

Figure 2.5: Equilibrium long range order as a function of temperature, as measured by Lee and Sykes using electrical resistivity. Curves for the theories of order described by Bragg and Cowley are provided for reference.

$$\frac{dS_m}{d\phi} = f(S)\frac{dS}{d\phi} + S\frac{df(S)}{d\phi} \tag{2.1a}$$

$$\frac{dS_m}{d\phi} = \frac{dS}{d\phi}\left[f(S) + S\frac{df(S)}{dS}\right] \tag{2.1b}$$

$$\frac{dS_m}{S_m d\phi} = \frac{dS}{Sd\phi}\left[1 + S\frac{f'(S)}{f(S)}\right] \tag{2.1c}$$

$$R = \frac{dS_m}{S_m d\phi}\left[\frac{dS}{Sd\phi}\right]^{-1} = 1 + S\frac{f'(S)}{f(S)} \tag{2.1d}$$

This relationship is particularly powerful, as the dependence of R on S necessarily results in a dependence on temperature, with $R \to 1$ as $T \to 0$ K. Further, Equation 2.1d was found to be essentially independent of the exact form chosen for $f(S)$. For the data presented by Lee, fitting a

simple quadratic equation for the scaling function revealed an estimated five-fold increase in the overestimation of disordering between low temperatures and T_c. While this effect is on the order of the anomalous increase in disordering reported by Lee, we are prevented from drawing a direct conclusion by the sensitivity of Equation 2.1d to the shape of both measured and reference curves immediately below T_c. The above exercise further emphasizes the need for alternative techniques when characterizing order-disorder behavior in this volatile range of temperatures.

2.3.2. Radiation Induced Disordering of Cu_3Au

The reduction of long range order with irradiation dose is shown in Figure 2.6 for several irradiation temperatures. (The curves in Figure 2.6 are taken from tests of two foils cut from the same bulk Cu_3Au and identically prepared.) As in previous works, this disordering behavior was found to depend strongly on the irradiation temperature, with specimens irradiated closer to T_c possessing lower steady states of order and decaying to them more quickly. This subsection will

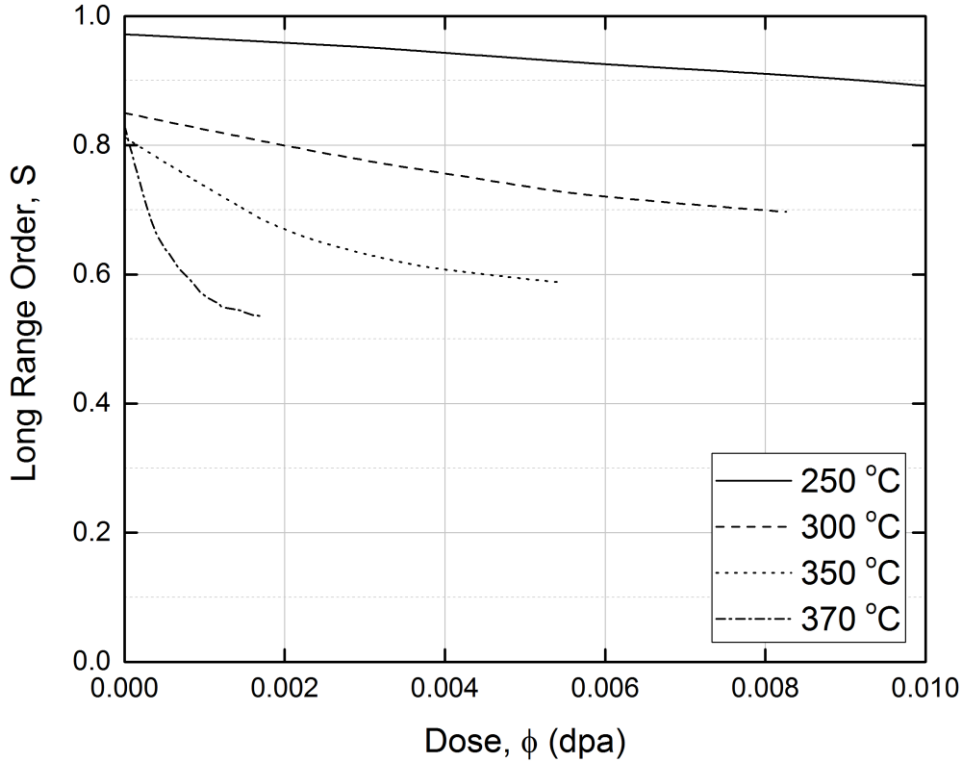

Figure 2.6: Traces of specimen long range order with dose at various irradiation temperatures.

be devoted to the analysis of this loss of chemical order during Ne^+ irradiation, with particular focus on initial disordering (i.e. doses below ~10^{-5} dpa) and the steady state degree of order.

Initial disordering rates were deduced for each irradiation by fitting the slopes of disordering curves, such as those shown in Figure 2.6. These rates are shown in Figure 2.7 as a function of irradiation temperature and clearly display a rapid increase on approaching T_c. This behavior is unexpected as the ballistic term in Equation 1.31 is almost independent of temperature [19], and the diffusive terms of the same result in reordering, rather than disordering. Further testing of the same specimen foil at four times the irradiation dose rate resulted in much the same trend, as shown alongside the lower dose rate in Figure 2.8. Such insensitivity to dose rate allows for three key deductions regarding the behavior: 1) that it is not significantly affected by ion beam heating in the current experimental design; 2) that it is not dependent on some critical proximity to the transition between sink and recombination limited regimes of defect production; and 3) that

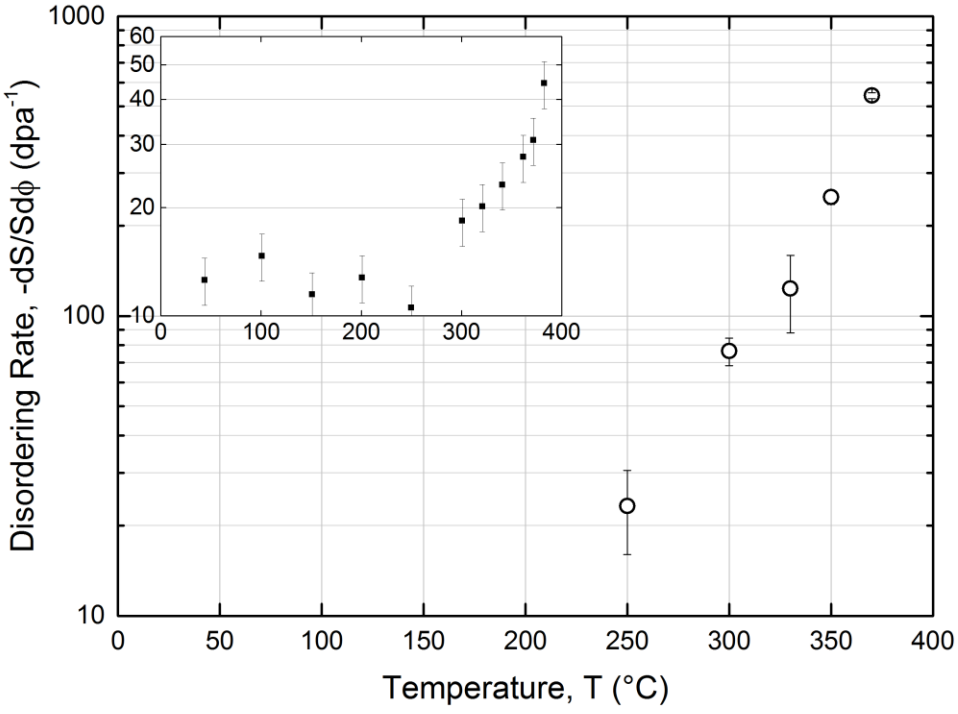

Figure 2.7: Normalized initial disordering rates vs. irradiation temperature for 500 keV Ne^+. Inset data taken from the work of Lee using 700 keV Ne^+.

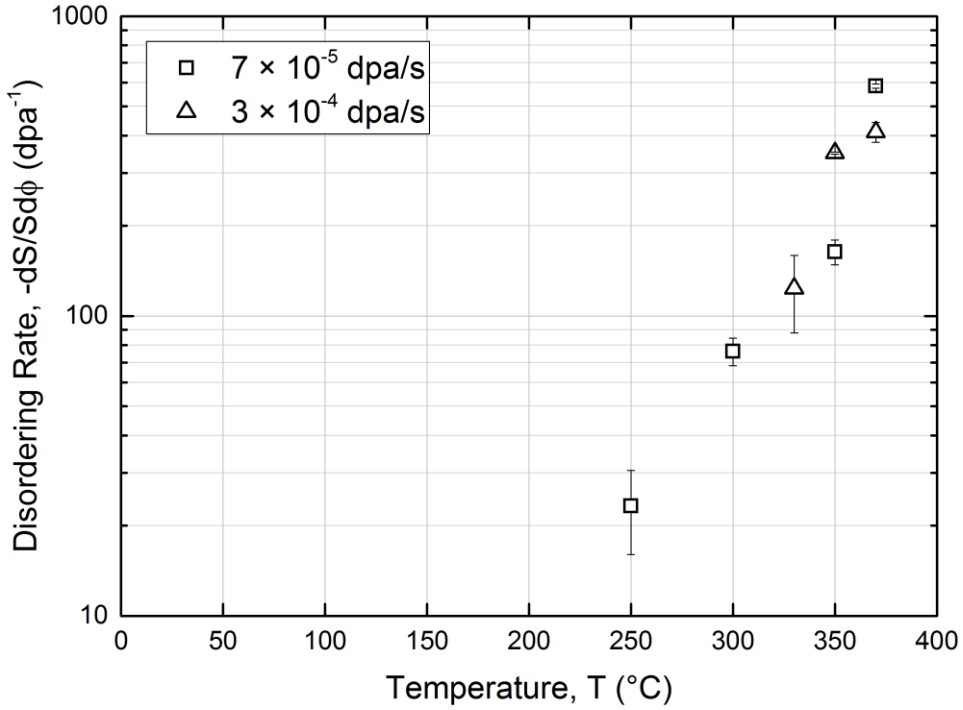

Figure 2.8: Normalized initial disordering rates vs. irradiation temperature for 500 keV Ne^+. Data for high and low dose rates have been separated to highlight the insensitivity to beam current.

the behavior is specific to the individual disordering events and not their interactions with one another. A similar, more shallow trend was observed by Lee using resistivity, shown inset in Figure 2.7, and a first attempt at explaining this behavior can be found in the same. Here, I will summarize these arguments and consider additional possibilities.

Confining the observed behavior to isolated events leaves only two reasonable mechanisms for the rapid increase in initial disordering with temperature, collision cascades and the migration of point defects out from them. Collision cascades could generate high rates of initial disorder, and molecular dynamics simulations have observed temperature dependence in the size of thermal spikes [20]. Such increases, however, are thought to be continuous and gradual with temperature and not particularly sensitive to T_c given the much higher temperatures inside the spike. The behaviors of mobile point defects, in contrast, are known to be strongly temperature dependent. In a separate work, Lee, *et al.* [21] investigated the effects of temperature and chemical order on

radiation enhanced diffusion (RED) in Cu_3Au and found the contribution of such defects increasingly significant beyond 250 °C. Further, *in situ* studies by Daulton, *et al.* [22] have found strong evidence of temperature dependence in cascade collapse for Cu, seemingly in agreement with *ex situ* studies of fcc metals in the literature [23, 24]. Together, these findings point to increases in both mobility and concentration of freely migrating point defects above ~250 °C, in good agreement with the onset of anomalous temperature dependence in disordering.

Having settled on point defect migration as our candidate mechanism, it is now necessary to explore the ways in which mobile defects can introduce disorder to the driven alloy. Migrating vacancies diffuse through the material at random under equilibrium conditions, and excess disorder introduced by the jump of one vacancy can be compensated by ordering jumps elsewhere. This balance is disturbed by the introduction of radiation damage. Local excess concentrations of defects lead to net fluxes from source cascades to defect sinks, releasing an excess free energy per defect,

$$\Delta F_v(T) = kT \log\left(\frac{C_v^{cas}}{C_v^{eq}(T)}\right) \tag{2.2}$$

where C_v^{cas} is local vacancy population of the cascade and C_v^{eq} is the equilibrium vacancy population at the given temperature (see Equation 1.8). The jumps of such non-equilibrium defects, while locally random, do not need to counter others elsewhere in the alloy and thus may introduced excess disorder using the free energy in Equation 2.2 as a driving force.

The extent to which radiation induced defects can contribute to disordering is thus dependent on the free energy penalty, ΔF_S, for introducing non-equilibrium disorder to the alloy. This energy can be derived by expansion of the free energy of the ordered state (see Equations

1.26) about the equilibrium state of order, S_{eq}. As discussed in the previous chapter, the first derivative of the free energy is always zero at the equilibrium state of order, requiring a second order expansion of the form,

$$\Delta F_s(\Delta S, T) = \frac{\partial^2 F_{mix}}{\partial S^2}\left(S_{eq}, T\right)\frac{(\Delta S)^2}{2} \tag{2.3}$$

where ΔS is the deviation from equilibrium long range order caused by the introduction of an excess anti-site defect and the second derivative is expressed in terms of the effective interaction volume N_{int} surrounding an isolated cascade,

$$\frac{\partial^2 F_{mix}}{\partial S^2}(S, T) = \frac{N_{int}kT}{16}\left[\frac{9}{1+3S} + \frac{3}{3+S} + \frac{6}{1-S} - 14.64\frac{T_c}{T}\right] \tag{2.4}$$

Translating between changes in S and anti-site population ($\Delta N_{as} = -3N\Delta S/8$ for $L1_2$ structures) and considering the driving force described in Equation 2.2, the maximum contribution to disordering from individual cascades can then be estimated as,

$$\Delta N_{as,max} = \sqrt{\frac{4.5N_{int}N_{v,cas}\left[\log\left(\frac{N_{v,cas}}{N_{cas}}\right) + \frac{E_{v,f}}{kT}\right]}{\frac{9}{1+3S_{eq}} + \frac{3}{3+S_{eq}} + \frac{6}{1-S_{eq}} - 14.64\frac{T_c}{T}}} \tag{2.5}$$

where $N_{v,cas}$ is the number of vacancies produced by a collision cascade, N_{cas} is the volume of that cascade, and $E_{v,f}$ is the vacancy formation energy. Numerical solutions of Equation 2.5 are presented in Figure 2.9 and account for significantly more anti-site defects than needed for the observed effect. We can thus conclude that sufficient free energy exists within the cascades to drive the anomalous increases in disordering near T_c reported here and in the work of Lee.

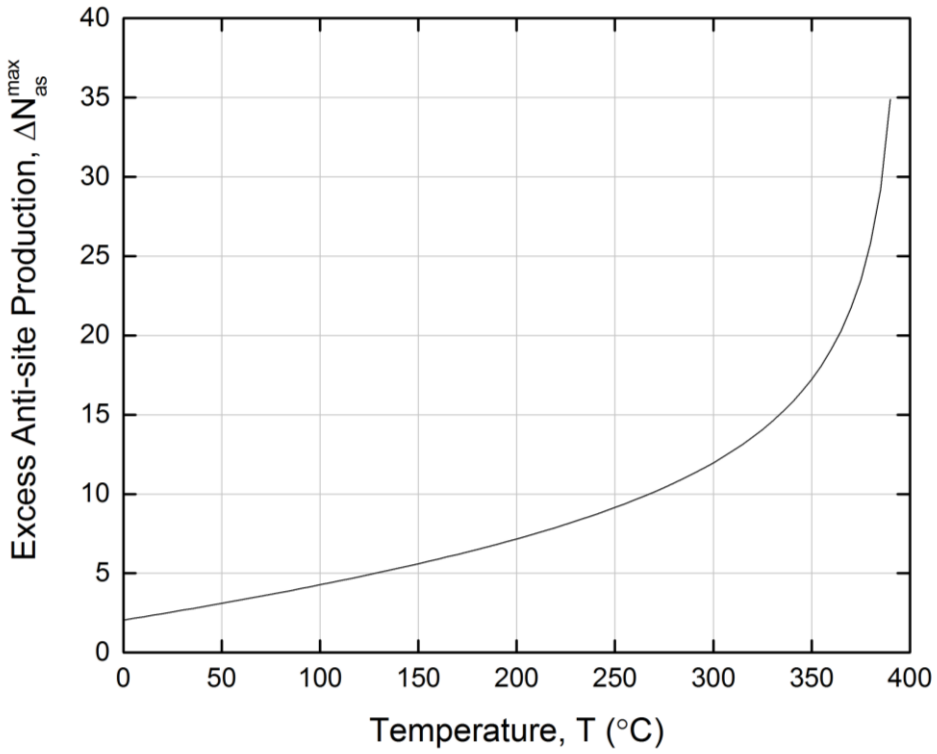

Figure 2.9: New anti-site defects per cascade as a function of temperature. Values are normalized by the expected anti-site production from the collision cascades alone, estimated at five anti-sites per Frenkel defect.

While the above calculations resolve our concerns with the free energy of disordering, the temperature dependence of solutions to Equation 2.5 is too weak to account for the slope of the observed effect. Rather, the sharp temperature dependence is a result of the impact of chemical order on vacancy diffusion. At low temperatures, the unbalanced defect fluxes and available free energy for disordering have no practical influence on alloy behavior, as high energy penalties restrict vacancy exchanges to the Cu sublattices of the alloy. With increasing temperature, however, vacancies gain access to the Au sublattice, and disordering may proceed as described. This critical step can be seen in changes to thermal reordering [9, 25] and diffusion on the Au sublattice [21] above ~200 °C. While Lee fit this diffusional effect for He^+ irradiation with a relationship proportional to $1 - S$, the present data was best fit proportional to $(1 - S)^2$. This

difference in behavior is not unexpected, as N_{int} in Equation 2.4 is itself dependent on $1 - S$ for Ne^{+} irradiation but constant for He^{+}.

2.4. DARK-FIELD IMAGING

2.4.1. Characterization of Disorder in Cu_3Au

In conjunction with the electron diffraction study described above, experiments were performed to explore the effects of irradiation temperature and dose rate on the ordered microstructure of Cu_3Au. Damage to the chemical order of the alloy was recorded in video form using superlattice dark-field imaging. As structural damage to the foils (e.g. dislocation loops) is not a focus of the present work, such features were differentiated using dark-field imaging of fundamental reflections and excluded from the following discussions. The initial tests described in this section focused on variations in damage from 300 °C to 375 °C and observed two broad categories of damage: transient and persistent.

"Type 1" damage consists of a localized loss of diffracted intensity associated with small clusters of disorder, typically under 20 nm in size. At all temperatures investigated, these regions were observed to form instantaneously and then dissolve more slowly with time. Although we lack the certainty in the thickness of our foils necessary for much detailed analysis, this form of damage appears consistent with previous works of Jenkins, *et al.* [26-30] on the size and nature of cascade damage in Cu_3Au. An example of this form of damage is shown in Figure 2.10 in the form of a grey, speckled contrast.

"Type 2" damage involves the modification of anti-phase boundaries, either by creation of new anti-phase domains, shown in Figure 2.11, or by warping existing boundaries from smooth to jagged contrast. These alterations to the ordered microstructure were comparable in size to Type

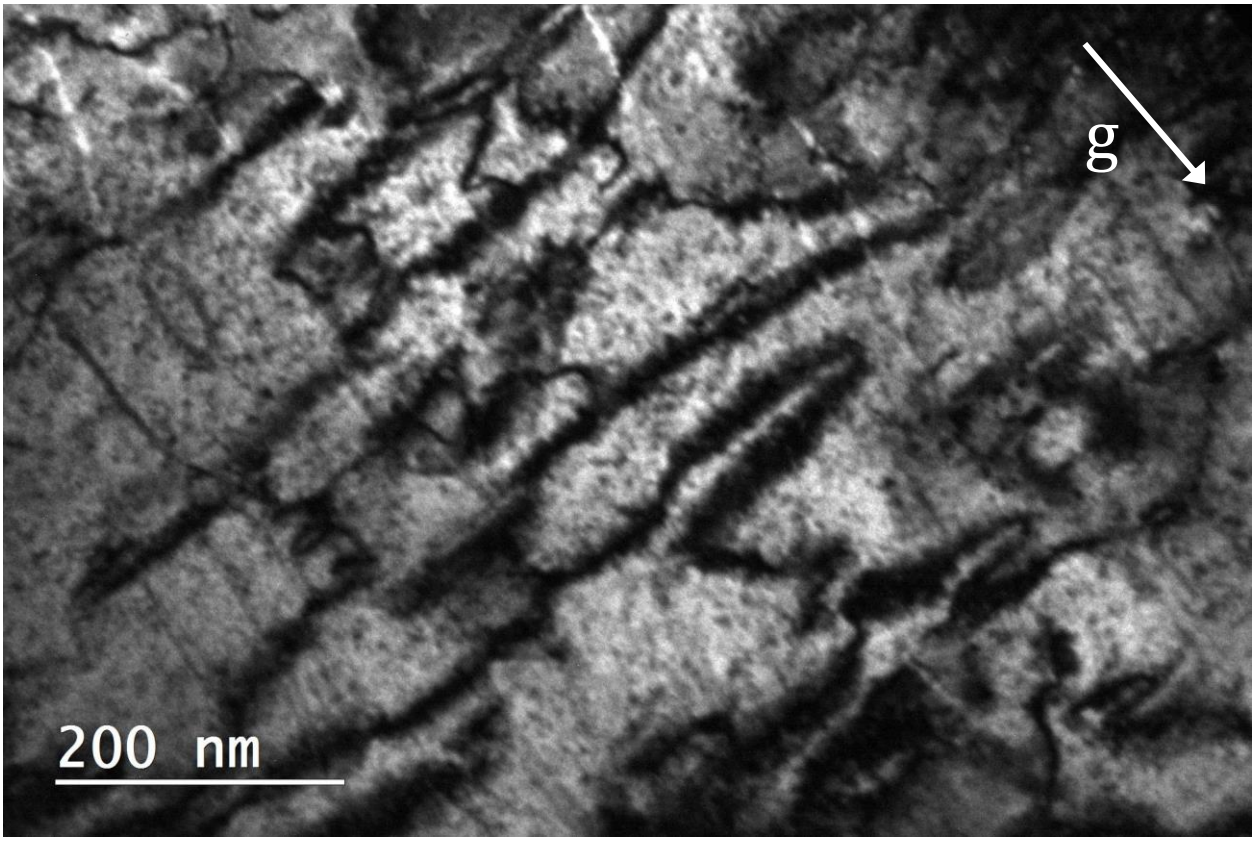

Figure 2.10: Dark-field, $g = \langle 110 \rangle$, micrograph of ordered Cu_3Au foil irradiated at 350 °C and 9.4×10^{-5} dpa/s. Dark anti-phase boundaries can be seen dividing bright ordered domains. The speckled contrast is transient damage seen to dissolve with time.

1 damage, but were observed to develop gradually with increasing irradiation dose. This form of damage was also observed to be more stable than Type 1, persisting in the absence of irradiation and even annealing at higher temperatures as in Figure 2.12. The most striking result, however, was the dependence of this damage on irradiation conditions. Unlike the universal occurrence of Type 1, Type 2 damage was observed only at sufficiently low temperatures or sufficiently high dose rates. This behavior suggests a competition between the production of disorder, driven by irradiation, and the thermal reordering of the alloy, controlled by vacancy mobility. Such a competition could be described in terms of a to date unreported critical anti-site concentration.

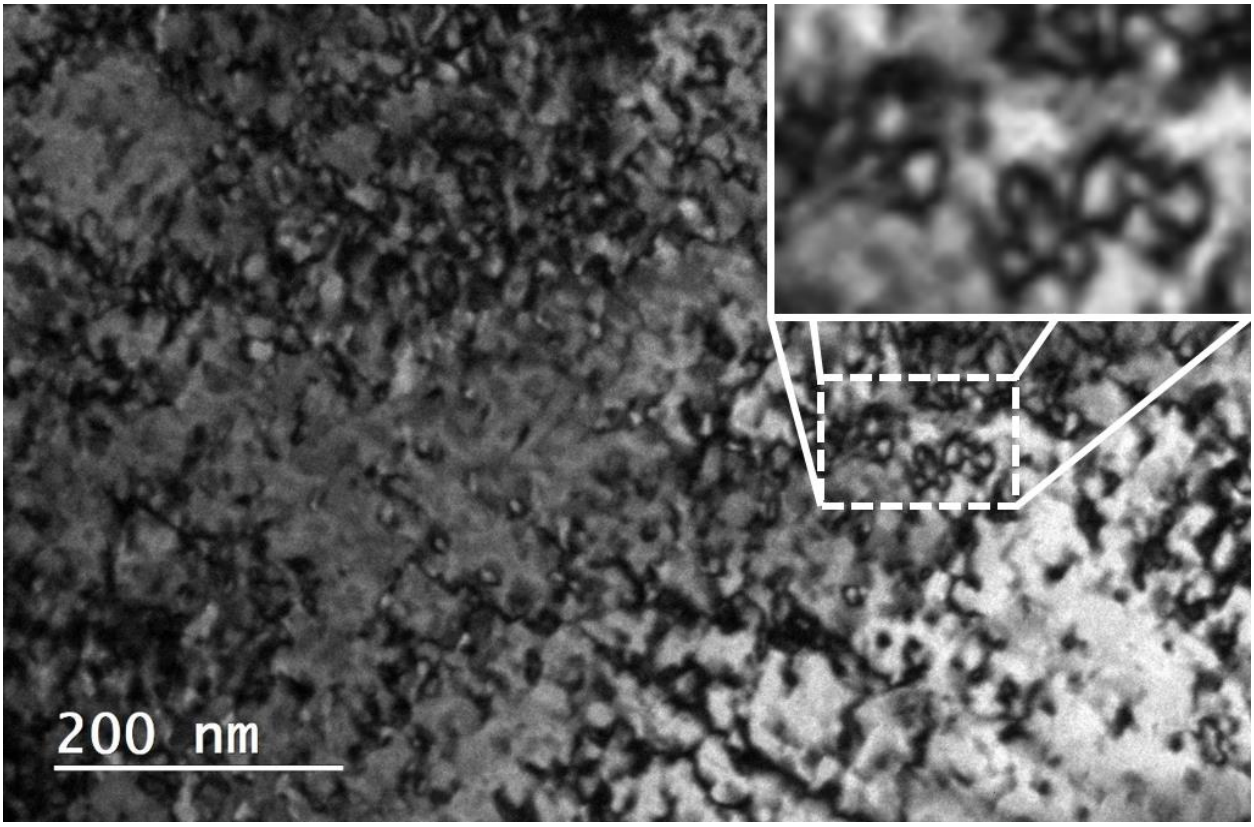

Figure 2.11: Dark-field, superlattice micrograph of ordered Cu_3Au foil irradiated at 350 °C and 1.1×10^{-4} dpa/s. The sharp anti-phase boundaries of the initial foil have been significantly blurred by the creation of small new domains, highlighted in the inset, although much of the original ordered microstructure will be recovered by post-irradiation annealing at 370 °C.

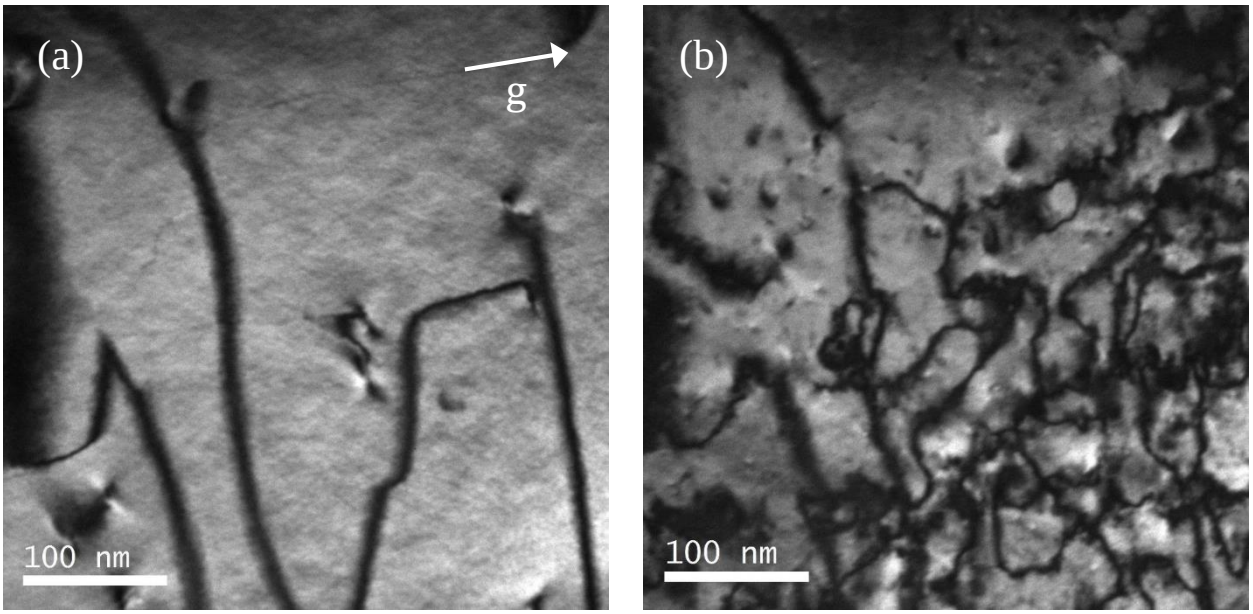

Figure 2.12: Dark-field, $g = \langle 110 \rangle$, micrographs of an ordered Cu_3Au foil (a) at 375 °C prior to irradiation and (b) following irradiation at 335 °C and 7.5×10^{-5} dpa/s and ~20 minutes annealing at 375 °C. Note the refinement of the final domain structure and the more curved anti-phase boundaries characteristic of newly grown domains.

2.4.2. Critical Behavior of the Ordered Microstructure

To better test this critical behavior, a systematic investigation of the evolution of the ordered microstructure was performed, using irradiation temperature and dose rate as control parameters. Foils were first heated to 350 °C and the ion beam switched on at a set dose rate. The ordered microstructure was then recorded as a function of time, again using dark-field, superlattice imaging. At 20 minute intervals, the specimen was cooled between 10 °C and 20 °C, while maintaining the constant (±10%) dose rate, and the microstructure again recorded. This time step was selected to achieve at least 1.5 times the steady state dose determined by Lee for Ne^+ irradiations above 300 °C. Cooling continued in this manner until the irradiation temperature reached 300 °C or imaging contrast was lost due to accumulated damage, and the entire procedure was repeated for dose rates between 1.9×10^{-5} dpa/s and 1.9×10^{-4} dpa/s (6.3×10^{10} ions/cm^{2}s and 6.3×10^{11} ions/cm^{2}s). Observations of damage behavior throughout these systematic tests are marked in Figure 2.13 according to irradiation temperature and dose rate, and a rough boundary for the appearance of Type 2 damage is provided as a guide to the eye.

In addition to confirming the temperature dependence noted during our initial characterization of Type 2 damage, these observations provide the first direct measure of Type 2 damage as a function of dose rate. This dose rate dependence agrees generally with steady state order measurements of Lee [1] for 1 MeV He^+ irradiations at varying dose rates but constant temperature. These measurements show a distinct change in the relationship between steady state order and dose rate, with increasing dose rate at each temperature. Although this change matches our estimated boundary for Type 2 damage quite well at 340 °C, see Figure 2.14, more in depth analysis is prohibited by the difference in irradiating particle and the limited overlap between our irradiation conditions and those other temperatures, 360 °C and 380 °C, tested by Lee.

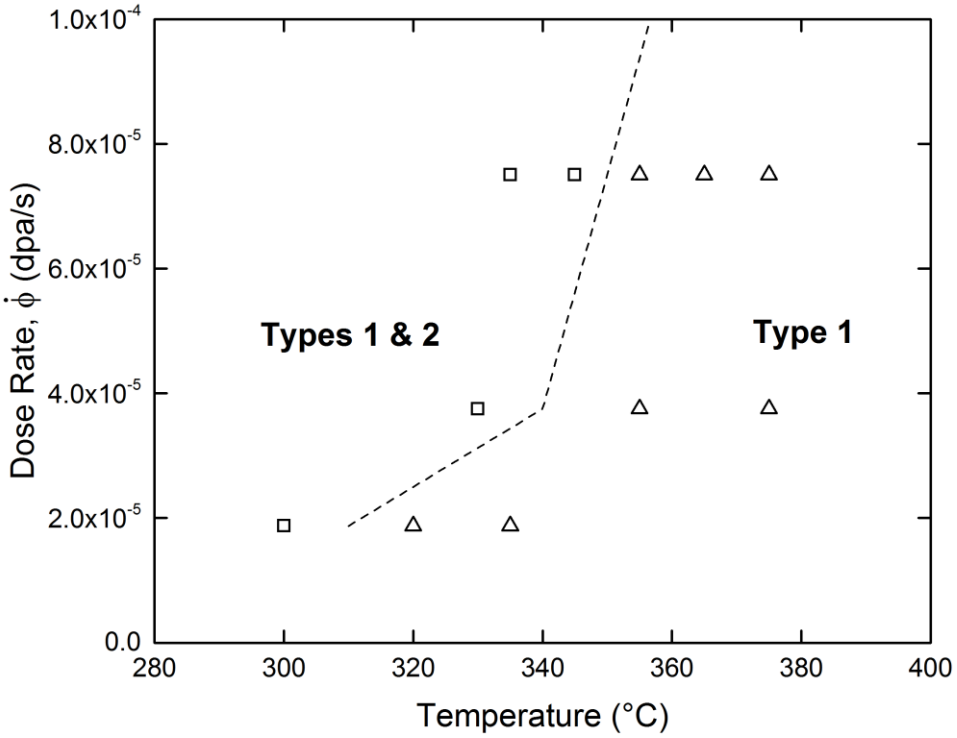

Figure 2.13: Observed forms of damage as a function of irradiation temperature and dose rate.

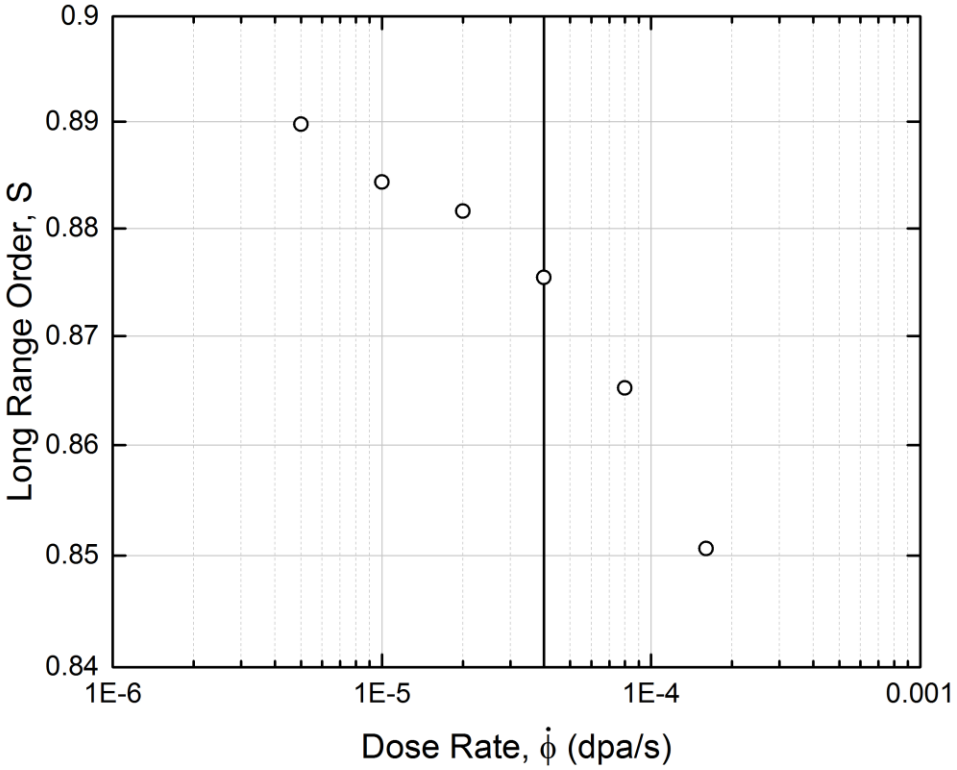

Figure 2.14: Log-log trend in steady state order, S, with irradiation dose rate, $\dot{\phi}$, as measured by Lee [1] for 1 MeV He^+ irradiation at 340 °C. The vertical line marks $\dot{\phi} = 4 \times 10^{-5}$ dpa/s, the estimated boundary at this temperature for the appearance of Type 2 damage. The boundary seems to coincide with a marked change in the trend.

2.5. CONCLUSIONS

This study of radiation induced disordering was carried out in response to reports of anomalous, temperature dependent disordering in Cu_3Au. *In situ* electron diffraction was explored as an alternative technique for measuring long range order, given concerns with systematic overestimation of disordering by resistivity. Although sensitive to the effects of mechanical bending and the resulting misalignment, diffraction measurements found a similar, if steeper, trend in the initial disordering rate of Cu_3Au foils irradiated at temperatures approaching the critical order-disorder temperature, T_c. The dose rate independent nature of these findings helped identify mobile radiation induced point defects as the likely mechanism for the observed disorder, while free energy calculations verify that the driving force supplied by local vacancy excesses within collision cascades is more than sufficient for the disordering measured.

Further study of Cu_3Au under prolonged irradiation revealed that radiation induced damage takes two principle forms. The first, associated with small clusters of disorder, was observed by dark-field, superlattice imaging to appear spontaneously and dissolve with time, while the second represented more stable, even persistent, alterations to the ordered microstructure of the foil. This latter form of damage is dependent on irradiation temperature and dose rate, being observed only at sufficiently low temperatures or sufficiently high dose rates. This behavior was explained in terms of a critical point defect concentration within the foil, although the exact role of the defects remains unclear.

2.6. REFERENCES

[1] Y. S. Lee, "Atomic transport mechanisms in irradiated Cu_3Au," Doctor of Philosophy, Physics, University of Illinois at Urbana-Champaign, Urbana, Illinois, 1996.

[2] E. A. Lang, "Radiation Damage and Radiation Induced Order-Disorder Transformations in Cu_3Au," Master of Science, Materials Science and Engineering, University of Illinois at Urbana-Champaign, Urbana, Illinois, 2000.

[3] *Center for Microanalysis of Materials*. Available: http://mrl.illinois.edu/facilities/center-microanalysis-materials/

[4] *Intermediate Voltage Electron Microscopy (IVEM)-Tandem Facility*. Available: http://www.ne.anl.gov/ivem/

[5] D. B. Williams and C. B. Carter, *Transmission Electron Microscopy: A Textbook for Materials Science*, 2 ed. New York: Springer Science+Business Media, 2009.

[6] Gatan, "Technical Note 9201: Dimpling ductile materials," ed, 2016.

[7] R. M. Fisher and M. J. Marcinkowski, "Direct observation of antiphase boundaries in the $AuCu_3$ superlattice," *Philosophical Magazine,* vol. 6, pp. 1385-1405, 1961.

[8] P. B. Hirsch, "Periodic and Ordered Structures," in *Electron Microscopy of Thin Crystals,* ed: Krieger Pub Co, 1965, p. 563.

[9] L. C. Wei, E. Lang, C. P. Flynn, and R. S. Averback, "Freely migrating defects in ion-irradiated Cu_3Au," *Applied Physics Letters,* vol. 75, p. 805, 1999.

[10] J. Ziegler, "Stopping and Range of Ions in Matter (SRIM)," SRIM-2013 ed, 2013.

[11] "Adobe After Effects," 13.7.2 ed: Adobe Systems, 2016.

[12] "MATLAB," R2016b ed: MathWorks, 2016.

[13] J. M. Cowley, "X-Ray Measurement of Order in Single Crystals of Cu_3Au," *Journal of Applied Physics,* vol. 21, p. 24, 1950.

[14] D. T. Keating and B. E. Warren, "Long-Range Order in β-Brass and Cu_3Au," *Journal of Applied Physics,* vol. 22, p. 286, 1951.

[15] J. M. Cowley, "An Approximate Theory of Order in Alloys," *Physical Review,* vol. 77, pp. 669-675, 1950.

[16] W. L. Bragg and E. J. Williams, "The effect of thermal agitation on atomic arrangement in alloys. I," *Proceedings of the Royal Society of London. Series A: Mathematical, Physical and Engineering Sciences,* vol. 145, pp. 699-730, 1934.

[17] W. L. Bragg and E. J. Williams, "The effect of thermal agitation on atomic arrangement in alloys. II," *Proceedings of the Royal Society of London. Series A: Mathematical, Physical and Engineering Sciences,* vol. 151, pp. 540-566, 1935.

[18] C. Sykes and F. W. Jones, "The atomic rearrangement process in the copper-gold alloy Cu_3Au," *Proceedings of the Royal Society of London. Series A, Mathematical and PhysicalSciences,* vol. 157, pp. 213-233, 1936.

[19] T. Diaz de la Rubia, R. S. Averback, H. Hsieh, and R. Benedek, "Molecular dynamics simulation of displacement cascades in Cu and Ni: Thermal spike behavior," *Journal of Materials Research,* vol. 4, pp. 579-586, 1989.

[20] H. Hsieh, T. Diaz de la Rubia, R. S. Averback, and R. Benedek, "Effect of temperature on the dynamics of energetic displacement cascades: A molecular dynamics study," *Physical Review B,* vol. 40, pp. 9986-9988, 1989.

[21] Y. S. Lee, C. P. Flynn, and R. S. Averback, "Thermal and radiation-enhance diffusion in Cu_3Au," *Physical Review B,* vol. 60, pp. 881-889, 1999.

[22] T. L. Daulton, M. A. Kirk, and L. E. Rehn, "In-situ transmission electron microscopy study of ion-irradiated copper: Temperature dependence of defect yield and cascade collapse," *Philosophical Magazine A,* vol. 80, pp. 809-842, 2000.

[23] T. M. Robinson and M. L. Jenkins, "Heavy-ion irradiation of nickel and nickel alloys," *Philosophical Magazine A,* vol. 43, pp. 999-1015, 2006.

[24] M. Wilkens, in *International Conference on the Fundamental Aspects of Radiation Damage in Metals,* Gatlinburg, Tennessee, 1975, pp. 98-112.

[25] L. C. Wei, Y. S. Lee, R. S. Averback, and C. P. Flynn, "Antistructure and point defect response in the recovery of ion irradiated Cu_3Au," *Physical Review Letters,* vol. 84, pp. 6046-6049, 2000.

[26] C. A. English, M. L. Jenkins, and M. A. Kirk, "Characterization of displacement cascade damage in Cu_3Au produced by fusion-neutron irradiation," *Journal of Nuclear Materials,* vol. 103 & 104, pp. 1337-1342, 1981.

[27] C. A. English and M. L. Jenkins, "Characterization of displacement cascade damage produced in Cu_3Au by fast-particle irradiation," *Journal of Nuclear Materials,* vol. 96, pp. 341-357, 1981.

[28] M. L. Jenkins, K.-H. Katerbau, and M. Wilkens, "Transmission electron microscopy studies of displacement cascads in Cu_3Au: I. The diffraction contrast of disordered zones," *Philosophical Magazine,* vol. 34, pp. 1141-1153, 1976.

[29] M. L. Jenkins and M. Wilkens, "Transmission electron microscopy studies of displacement cascads in Cu_3Au: II. Experimental investigation of cascades produced by Cu ions," *Philosophical Magazine,* vol. 34, pp. 1155-1167, 1976.

[30] M. L. Jenkins, N. G. Norton, and C. A. English, "Transmission–electron–microscopy studies of displacement cascades in Cu_3Au Cascades produced by 100–200 keV Cu^{+w} ions," *Philosophical Magazine A,* vol. 40, pp. 131-136, 1979.

CHAPTER 3

DISORDERING BEHAVIOR IN A SIMULATED 2D LATTICE

As discussed in the preceding chapter, *in situ* transmission electron microscopy (TEM) of Cu_3Au under light ion irradiation revealed unexpected alterations to the ordered microstructure of the alloy for sufficiently low irradiation temperatures or sufficiently high dose rates. This persistent form of damage is thought to occur when critically large, local anti-site concentrations collapse to form new ordered domains. Continuous nucleation of new domains would reduce the average domain size, while their formation along existing anti-phase boundaries could promote domain growth or boundary roughening by merging with neighboring domains. By analogy to previous studies of self-organization reactions for systems undergoing precipitation [1-3] and chemical ordering [1, 4-7], it is interesting to study how this dynamical competition affects the evolution of ordered domains, possibly resulting in domain patterning. In this chapter, we use kinetic Monte Carlo (KMC) simulations to investigate the roles of atomic interactions, vacancy diffusion, and radiation induced atomic replacements on ordered domain formation and stability. For simplicity, a two-dimensional model system is simulated in place of Cu_3Au. This choice allows us to consider the effects of several disordering mechanisms on large systems, without extended computing time, and to simplify the analysis of the results.

3.1. SIMULATION METHODS

3.1.1. Kinetic Monte Carlo Simulations

Atomic configurations for the present work were constructed by arranging equal numbers of A and B atoms on a rigid, square lattice with periodic boundary conditions in all directions. These equiatomic AB alloys were treated similarly to the two-dimensional Ising model [8], with A and B atoms taking the place of switchable magnetic spins and site interactions considered over both first and second nearest neighbor shells. In addition to equilibrium and disordering induced anti-site defects, which will be discussed further below, point defects in our configurations included a conserved population of vacant sites. These vacancies were permitted to exchange with neighboring atoms according to thermally activated diffusion. While vacancies in three-dimensional alloys like Cu_3Au exchange with only first nearest neighbors, first and second nearest neighbor exchanges were included here to prevent vacancy trapping at low temperatures, when diffusion in highly ordered configurations would require the creation of one or more anti-site defects if restricted to first nearest neighbor exchanges. Further, we used additional simulations at elevated temperatures, $T > 0.8T_c$, to confirm that these additional exchanges do not significantly affect the observed steady states. While this result is imposed by detailed balance under equilibrium conditions, no such guarantee applies under imposed disordering, and the result there is thus reassuring.

The KMC simulations were adapted from a model, developed by Enrique and Bellon [9], in which atomic migration occurs by two mechanisms: 1) thermally activated exchange between atoms and neighboring vacancies; and 2) fixed rate exchange between random, distant atoms. The first mechanism is responsible for thermally activated diffusion, while the second captures some components of disordering introduced by atomic recoils during irradiation. Frequencies for

thermally activated exchange were calculated using standard rate theory and a broken bond accounting [10],

$$f_{th} = \upsilon \cdot \exp\left(\frac{-\Delta E_{vx}}{kT}\right) \tag{3.1a}$$

$$\Delta E_{vx} = E_x^{sp} - J_1\left(\sum_m \sigma_{mx} + \sum_{n\neq x} \sigma_{nv}\right) - J_2\left(\sum_o \sigma_{ox} + \sum_{p\neq x} \sigma_{pv}\right) \tag{3.1b}$$

where υ is the attempt frequency, assumed here to take a constant value of 10^{14} s^{-1} for both first and second neighbor exchanges; E_x^{sp} is the saddle point energy; labels m and o indicate the first and second nearest neighbors of site x; labels n and p indicate the first and second nearest neighbors of vacancy v; and the σ_{ij} terms are pair occupancy functions that take a set value depending on the species of neighbors i and j (traditionally 0 or ±1). The ordering energies, J_s, in Equation 3.1b are,

$$J_s = 2\epsilon_{ab}^{(s)} - \left(\epsilon_{aa}^{(s)} + \epsilon_{bb}^{(s)}\right) \tag{3.2}$$

where $\epsilon_{ij}^{(s)}$ terms represent species specific pair interactions between s shell nearest neighbor sites i and j. These interactions, detailed later, were chosen to produce chemically ordered equilibrium structures.

To simplify later analysis and improve calculation efficiency, we set $\sigma_{ab} = 1$ and all other $\sigma_{ij} = 0$ for the present work. We note that this does not limit the thermodynamics of the system, as only the overall values of the J_s terms are relevant to the equilibrium states. For the kinetic evolutions of the simulated alloys, however, the relative strength of A-A and B-B interactions can, separate from the ordering energies, modify coarsening kinetics near equilibrium [11] and alter

steady state selection in non-equilibrium systems [12]. The simulations were further simplified by forbidding associative jumps for vacancies, and thus the formation of divacancies and larger clusters. This was done to prevent such defects from dominating microstructural evolution in the absence of defect sinks, in contrast to real systems where they would quickly annihilate at sinks.

While previous works with this model used predefined distributions to vary the distance of radiation induced atomic relocations, the present work constrained relocations to first nearest neighbors only. The reasoning behind this choice was two-fold. First, competition between medium to long range relocations and diffusive effects have already been shown to drive patterning of alloy composition [2] in fcc systems, making further study in our simplified alloys unnecessary. Second, the use of neighbor exchanges was thought to provide the best comparison with diffusional disordering mechanisms to be discussed below. These relocations were carried out at a constant rate of replacement, Γ_{rp} (atoms^{-1}s^{-1}), by randomly selecting one atom and exchanging it with a first nearest neighbor of the other species (i.e. A-B exchanges). While computationally efficient, it should be noted that this procedure does not guarantee the creation of anti-site defects with each replacement event; in fact, the probability of anti-site production decreases along with decreasing long range order of the alloy.

Time for the KMC simulations was tracked according to the residence-time algorithm (RTA) [13, 14]. The transition for each simulated step was selected at random and in proportion to its relative frequency, with the time then incremented by,

$$\Delta t = -\frac{\ln(u')}{\sum f_i} \tag{3.3}$$

where u' is a uniform random number (0,1] and $1/\sum f_i$ is the residence time of the current state including atom-vacancy exchanges and atomic relocations. For simulations with defect-assisted

migration of atoms, as in the current work, measured times are often sensitive to the possible trapping of vacancies in the lattice. This can occur, for example, when vacancy-atom interactions bind the defects strongly to the interfaces of minority species precipitates, preventing the diffusion of that species through the lattice and slowing coarsening. These effects can be compensated for by further scaling, using approaches such as that proposed by Soisson, *et al.* [15]. We note, however, that this scaling does not affect the steady states of the simulated alloys, which is the main focus of the present work.

As described in the previous chapter, the net flux of vacancies from collision cascades to defect sinks has been proposed as a cause for anomalies in the disordering of Cu_3Au under light ion irradiation observed by Lee [16] and Lang [17]. To investigate this mechanism further, the effects of a net vacancy flux were tested on the simulated alloys in addition to the disorder introduced by fixed rate atomic relocations. This flux was controlled by adding a bias energy, μ, to ΔE_{vx} for atom-vacancy exchanges in the positive *x* direction, while the same energy μ was subtracted from transitions in the opposite direction. The resulting flux was linear for small values of μ, before saturating above $|\mu| \lesssim 2kT$ as the number of unbiased exchanges per time step fell to zero.

3.1.2. Characterization of Order

Short and long range order parameters were central to analysis of the simulated alloys. The short range order parameter, s, was defined as,

$$s = \frac{n_{ab} - 2zX_aX_b}{n_{ab}^{(0)} - 2zX_aX_b} \tag{3.4}$$

where n_{ab} and $n_{ab}^{(0)}$ are the number of A-B first nearest neighbor pairs in the current and perfectly ordered states, respectively; z is the coordination number of the first nearest neighbor shell, here 4; and X_a and X_b are the fractions of A and B atoms in the alloy, respectively. This form of s is analogous to the parameters defined by Bethe [18] and Warren-Cowley [19], s_1, and given in Equations 1.20 and 1.21 and highlights the distinction between perfectly ordered sites, $s(\boldsymbol{r}_i) = 1$, and anti-site defects, $s(\boldsymbol{r}_i) = -1$, when s is computed for individual lattice sites. Calculating the long range order parameter, S, for the simulated alloys required the structure factor intensity around the superlattice wavevector, $\boldsymbol{k}_s$,

$$I = \left\langle \left| N^{-1} \sum_j \left(n_j - X_a\right) \exp\left(2\pi i \boldsymbol{k}_s \cdot \boldsymbol{r}_j\right) \right|^2 \right\rangle \tag{3.5}$$

where N is the number of lattice sites, n_j takes a value of 1 if site j at position $\boldsymbol{r}_j$ is occupied by an A atom and 0 otherwise [13], $\boldsymbol{k}_s = \left\langle \frac{1}{2a}, \frac{1}{2a} \right\rangle$ for the ordered structure studied here, and the bracket denotes circular averaging to half the first Brillouin zone. Intensity measurements for the perfectly ordered lattice, I_0, and the random background, I_b, were then used to determine the current order parameter from I,

$$S = \sqrt{\frac{I - I_b}{I_0 - I_b}} \tag{3.6}$$

In addition to S, the division of the lattice among ordered variants was analyzed using a net magnetization, M, calculated by assigning values of 1 or -1 to atoms according to the ordered variant their positions best matched. These "spins" were then summed over the lattice and normalizing by the population of atoms. The importance of this magnetization comes from our

desire to accurately determine the equilibrium order-disorder transition temperature, T_c, for simulated alloys. This was carried out using an analysis of the fourth order cumulant of M developed by Binder [20, 21],

$$U_L = 1 - \frac{\langle M^4 \rangle}{3\langle M^2 \rangle^2} \tag{3.7}$$

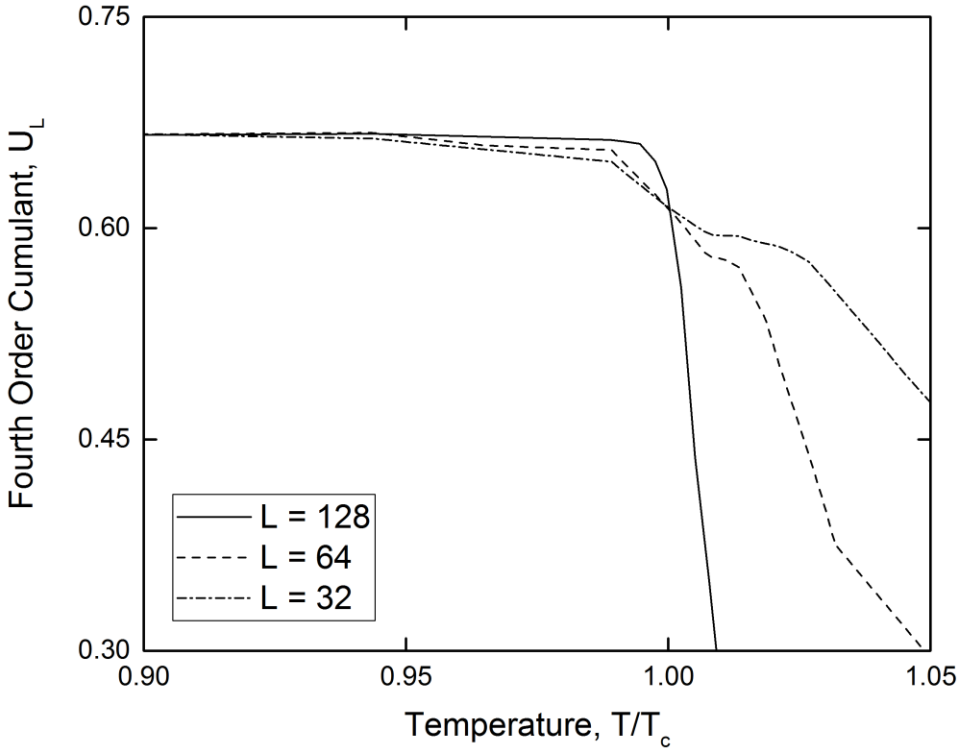

Figure 3.1: Fourth order cumulant of the long range order S versus temperature for several system sizes. The size independent crossing is used to find T_c, by which temperatures are scaled.

This relationship is observed to decrease from its low temperature value, $U_L = \frac{2}{3}$, toward zero starting just below the order-disorder transition. This descent is faster and starts at higher temperatures for larger system sizes, L, leading to a size independent crossing at $T = T_c$, as exemplified by Figure 3.1. Although powerful, testing increasingly large L and reducing noise for accurate determination of the crossing require considerable computing time. The above procedure was therefore only applied to the alloys with the most extreme ratios of neighbor interactions, $R =$

0 and $R = 0.45$, described in detail in the following section. For the other simulated alloys, T_c was approximated as the temperature at which $S = 0.8$ for the largest available L, which was at least 128 for the alloys investigated here. The resulting error of the approximation, ~15%, is not expected to alter the disordering behavior discussed below, as effects were tested for temperatures $0.7T_c$ to $1.1T_c$.

3.1.3. Energetic Parameters

Three distinct ground states, shown in Figure 3.2, exist for the two dimensional, square lattice with first and second nearest neighbor interactions. For the present work, we will avoid the phase separated, "ferromagnetic", ground state and focus on the mixed phases occurring when $J_1 < 0$. These phases are differentiated by the relative strength of the neighbor interactions, $R = J_2/J_1$, and undergo chemical order-disorder transitions with increasing temperature. For $R < 0.5$,

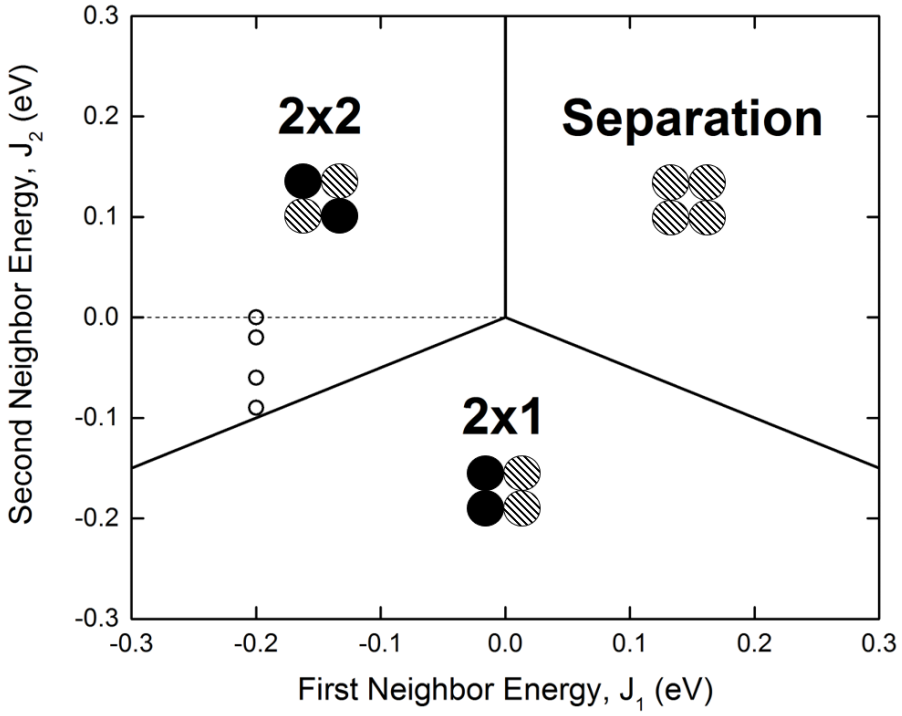

Figure 3.2: Ground state diagram for the two-dimensional square lattice. Open circles mark energetic parameters tested in the present work.

A and B atoms are organized at low temperatures to maximize A-B bonding among first nearest neighbors. This leads to a 2x2, "antiferromagnetic", structure with interlocking A and B sublattices. $R > 0.5$, on the other hand, promotes second nearest neighbor A-B bonds at low temperature, resulting in a 2x1, "superantiferromagnetic", structure with parallel A and B sublattices. As with the $L1_2$ structure of Cu_3Au discussed in past chapters, ordered variants (two for 2x2; four for 2x1) and anti-phase boundaries play a significant role here, especially near the degenerate state $R = 0.5$.

When selecting energetic parameters for the current simulations, care was taken to find an alloy with equilibrium order-disorder behavior comparable to the first order transition in Cu_3Au. Although first order transitions have been reported for a wide range of 2x1 alloys near the opposite $R = 0.5$ boundary [22] as well as for similar two dimensional alloys under imposed fields [23], equilibrium transitions in these systems are generally second order, decaying gradually from perfect order to random solution. Our attention was ultimately drawn to the region surrounding $R = 0.5$ by the work of Kalz, *et al.* [24], which revealed a first order transition for 2x1 phases approaching the boundary. The high fraction of A-A and B-B bonds between first nearest neighbors in these 2x1 alloys, however, made them poor surrogates for testing disorder and focus was thus directed to the little investigated 2x2 alloys just above $R = 0.5$. The order-disorder behavior for such an alloy, $R = 0.45$, is shown in Figure 3.3. While we could not identify an R value resulting in a first order transition, the sharpness of the second order transition for this alloy made it a suitable candidate for testing, and the results presented here are based on the $R = 0.45$ alloy unless otherwise stated.

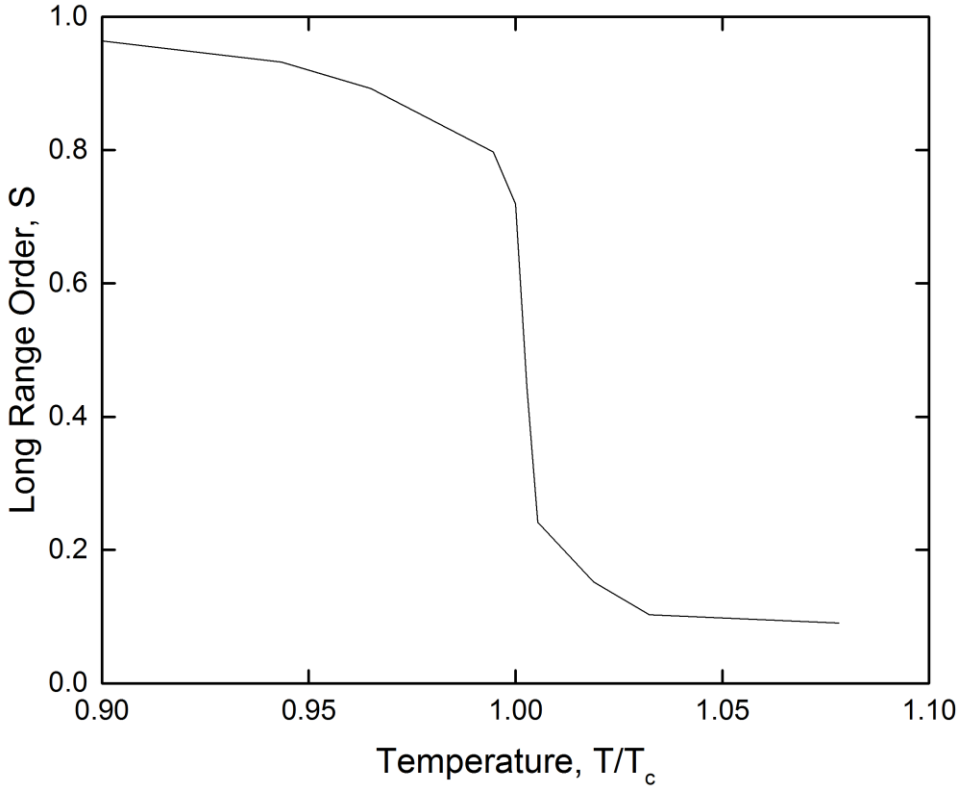

Figure 3.3: Long range order as a function of temperature for a simulated alloy with $J_1 = -0.20$ eV and $J_2 = -0.09$ eV. Temperatures are scaled to the equilibrium order-disorder transition temperature T_c.

3.2. NANOSCALE PATTERNING OF ORDER

3.2.1. Nature and Critical Behavior of Disorder

The simulated alloys displayed a variety of equilibrium and driven forms of disorder. In the absence of imposed disordering mechanisms, equilibrium chemical order was observed to decrease gradually with increasing temperature as isolated anti-site defects accumulated in the alloys. The magnitude of this disordering reflected the order of the transitions at T_c, with the $R = 0.45$ alloy remaining more highly ordered than the other alloys with second order transitions. As temperatures neared T_c, some clustering of anti-site defects was observed, and small anti-phase domains formed for the $R = 0.45$ alloy. Because these systems were characterized by minor amounts of disorder in otherwise well-ordered lattices, we will refer to this kind of behavior as "single domain" when comparing driven disordering in the following sections.

Given the upward trend in disordering rates for Cu_3Au under irradiation near T_c, see Section 2.3, initial disordering rates for the simulated alloys were measured as a function of temperature. These measurements were taken by calculating S every 1,000 Monte Carlo steps (atom-vacancy exchanges and forced relocations) from the time the imposed disordering was applied until the alloys reached steady state. Normalized disordering rates, $-dS/Sdt$, were then determined by fitting progressively longer initial portions of the trace, ending the fit when the result differed from the initial slope by $> 10\%$. Such disordering rates are presented in Figure 3.4 for the $R = 0.45$ alloy under a constant bias on vacancy-atom exchange. The disordering rates show a similar, upward temperature dependence to that seen experimentally on approaching T_c, but the current KMC method prevents measurement of the constant, low-temperature disordering rate necessary for direct comparison.

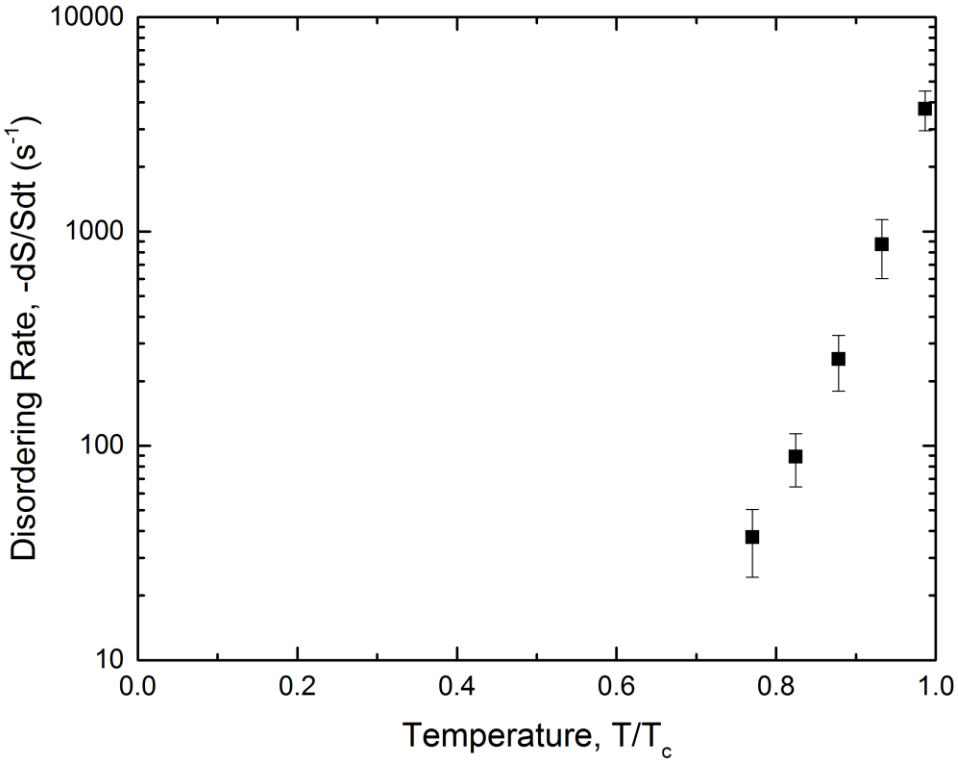

Figure 3.4: Simulated initial disordering rates at a constant, bias on vacancy exchange, μ.

The observation of temperature and dose rate dependent domain nucleation in Cu_3Au under prolonged irradiation, see Section 2.4, prompted a similar investigation into the effects of increasing imposed disordering rates on our simulated alloys. Initial testing of these steady states was carried out using a simple, fast method by which perfect 2x2 were exposed to a given temperature-disordering rate condition for a fixed period of time, with periodic recording of the order parameters. Once finished, the S, M, and s traces were inspected manually and unfinished runs restarted from their saved final states. By conducting many such runs in parallel at a fixed temperature but increasing rates of disorder, we could easily discern key departures between steady state and equilibrium ordered microstructures. While crude, these investigations revealed considerable differences in the evolution of steady states between the alloys. As with their equilibrium order-disorder transitions, the alloys with R values of 0, 0.1, and 0.3 displayed a smooth transition from perfect 2x2 order to disorder, as shown in Figure 3.5 for the $R = 0$ alloy. This is distinctly different from the behavior observed for the $R = 0.45$ alloy, shown in Figure 3.6.

For low values of the bias μ or the relocation rate $\dot{\phi}$, the $R = 0.45$ alloy retained the single domain ordered microstructure observed at equilibrium with only excess anti-site defects or a few additional, small anti-phase domains. At sufficiently high disordering rates, however, increasing numbers of anti-phase domains divide the alloy. While these anti-phase domains decrease in size with increasing disordering rate, as expected, they remain surprising well ordered, often containing no anti-site defects at all. This microstructure is similar to those reported previously by Ye, *et al.* [1, 4-7] for patterning of order in three-dimensional $L1_0$ and $L1_2$ alloys, but must arise from different physical causes as domains there were seen to nucleate within the large disordered regions of displacement cascades. Further increases in disordering rate beyond this "multi-domain" state resulted in complete disordering of the ordered microstructure.

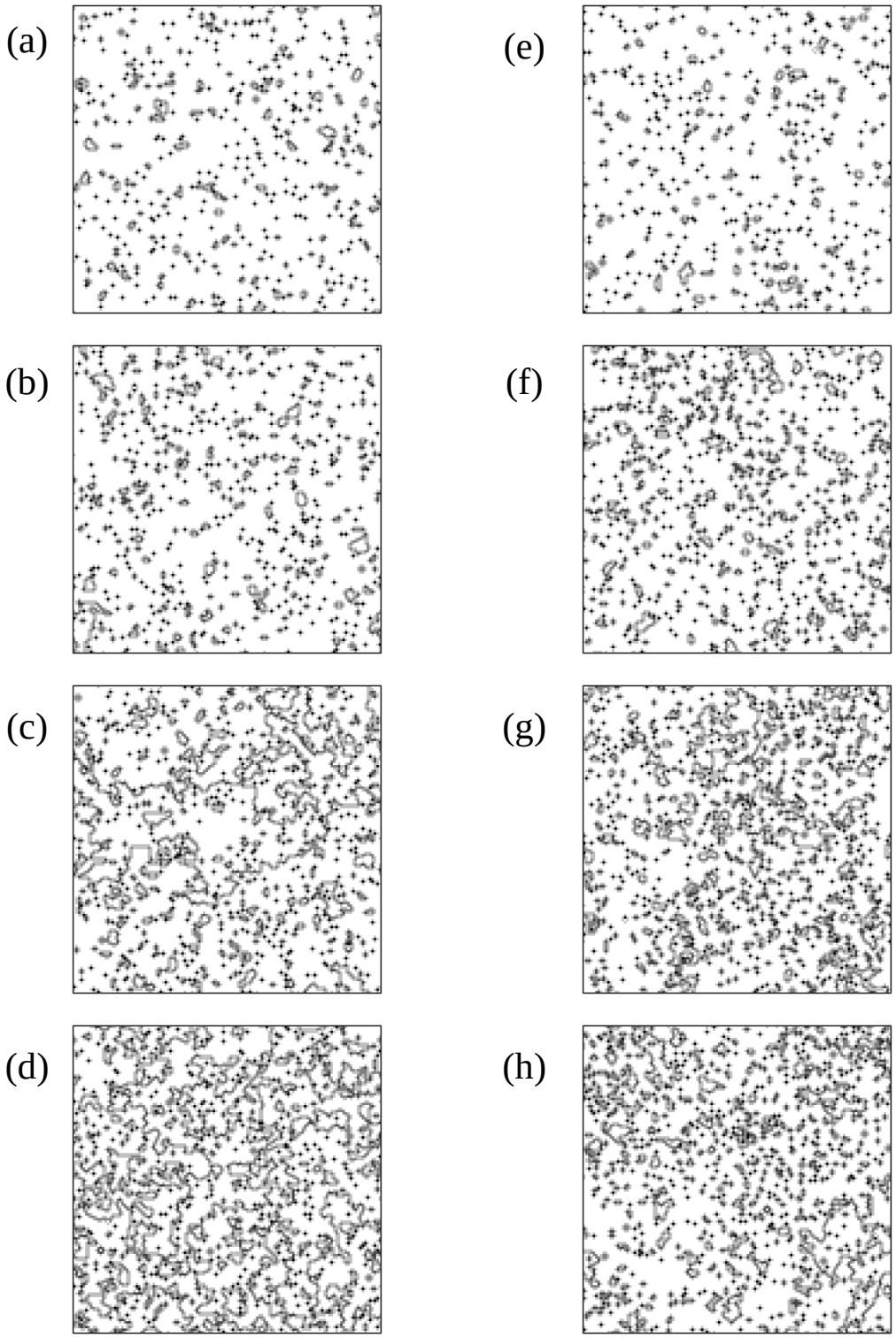

Figure 3.5: Atomic configurations of the $R = 0$ alloy under imposed disordering at $0.9T_c$, shaded according to s at each site Configuration (a) to (d) show disordering at bias values, $|\mu|/kT_c$, of 0, 0.5, 0.75, and 1. Configurations (e) to (h) show disordering at replacement rates, Γ, at 0, 1×10^8, 1.5×10^8, and 2×10^8 s^{-1}.

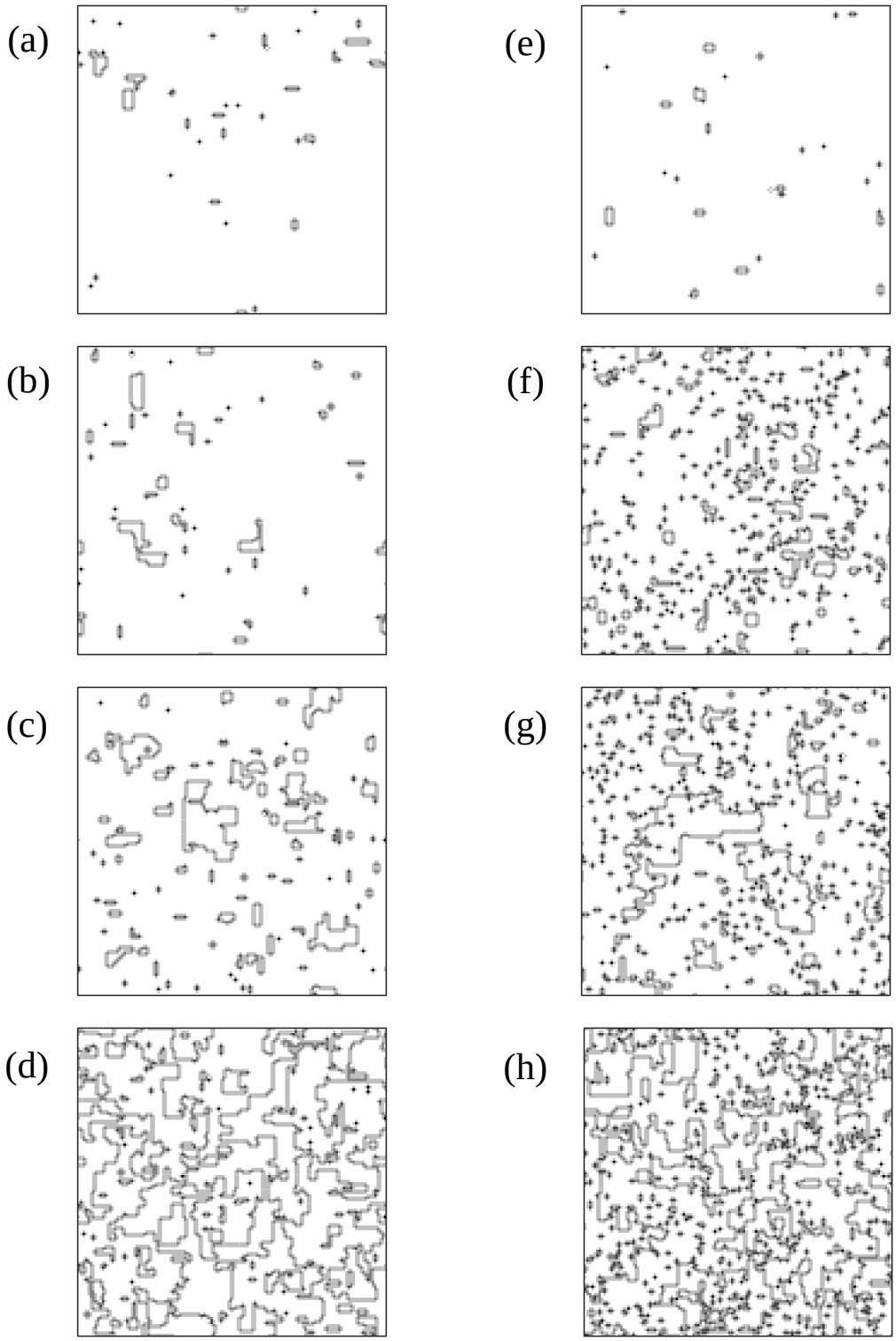

Figure 3.6: Atomic configurations of the $R = 0.45$ alloy under imposed disordering at $0.9T_c$, shaded according to s at each site Configuration (a) to (d) show disordering at bias values, $|\mu|/kT_c$, of 0, 0.5, 0.75, and 1. Configurations (e) to (h) show disordering at replacement rates, Γ, at 0, 4×10^3, 6×10^3, and $8\times10^3 s^{-1}$.

The disordering behaviors described above were next investigated systematically to observe a broader range of temperatures and imposed disordering rates, as well as to verify the existence and determine the features of critical disordering in the $R = 0.45$ alloy. To ensure that measurements of order represented true steady states of the system, care was taken to begin simulations from both a fully ordered 2x2 lattice and a fully disordered random solution. These tests were carried out by alternating between two saved configurations of the system, allowing each to evolve for some time, and then testing the convergence of the systems with a 10% significance level *t*-test (based on Welch [25]) of the hypothesis: $\langle S \rangle_1 = \langle S \rangle_2$. Once this convergence test was passed, the configurations were saved for later inspection and the pooled statistics of S recorded as the steady state. Statistics reported here for the steady state of M and s are those of the configuration beginning as a perfect 2x2 lattice, measured after convergence.

These systematic tests confirmed our earlier observations of disordering for alloys with low R values, as represented by the behavior of the $R = 0$ alloy in Figure 3.7 and Figure 3.8. Here, maps of S, M, and s versus the temperature and imposed disordering condition, reveal a relatively broad and smooth transition from the 2x2 ordered steady state to a random system. While some small anti-phase domains are observed at higher rates of imposed disorder, the lack of a sharp break between measured M and s for these states suggests that the domains are more like those seen under equilibrium conditions: statistical variations rather than a distinct feature of the ordered microstructure. The most striking features of these tests come when comparing the observed behavior to that of the $R = 0.45$ alloy, shown in Figure 3.9 and Figure 3.10.

Here, the steady state values of M and s reveal a sharp difference between the evolution of the long and short range order with disordering. While the measured M, Figure 3.9b and Figure 3.10b, drops quickly just beyond the boundary of the single domain microstructure, the measured

s, Figure 3.9c and Figure 3.10c, shows a much more gradual decrease in the local order of individual atoms. This behavior is consistent with the multi-domain microstructure noted above from direct observation of atomic configurations, with the division of the lattice into highly ordered anti-phase domains quickly eliminating the dominance of any one ordered variant yet preserving the ordered bonding of most atoms. As expected, a combination of both behaviors can be seen in the measured S of the alloy, Figure 3.9a and Figure 3.10a, due to the inclusion of some short range order information in the tails of the integrated structure factor peak. Boundaries between the single and multi-domain microstructures, provided in Figure 3.9d and Figure 3.10d, were approximated by direct observation of atomic configurations and were found to roughly follow the $S = 0.4$ contour. The distinction between the multi-domain and random microstructures, on the other hand, proved difficult to determine, as the gradual decrease in domain size leads to subjective comparisons between multi-domain systems with trivially small ordered domains and the random lattice. In place of a set boundary, we thus provide the $S = 0.1$ contour as a guide to the eye for distinguishing the extent of the multi-domain region. This approximation is reasonable given that S values of 0.1 are observed at temperatures as high as $1.2T_c$, where atomic configurations are indistinguishable from the random lattice.

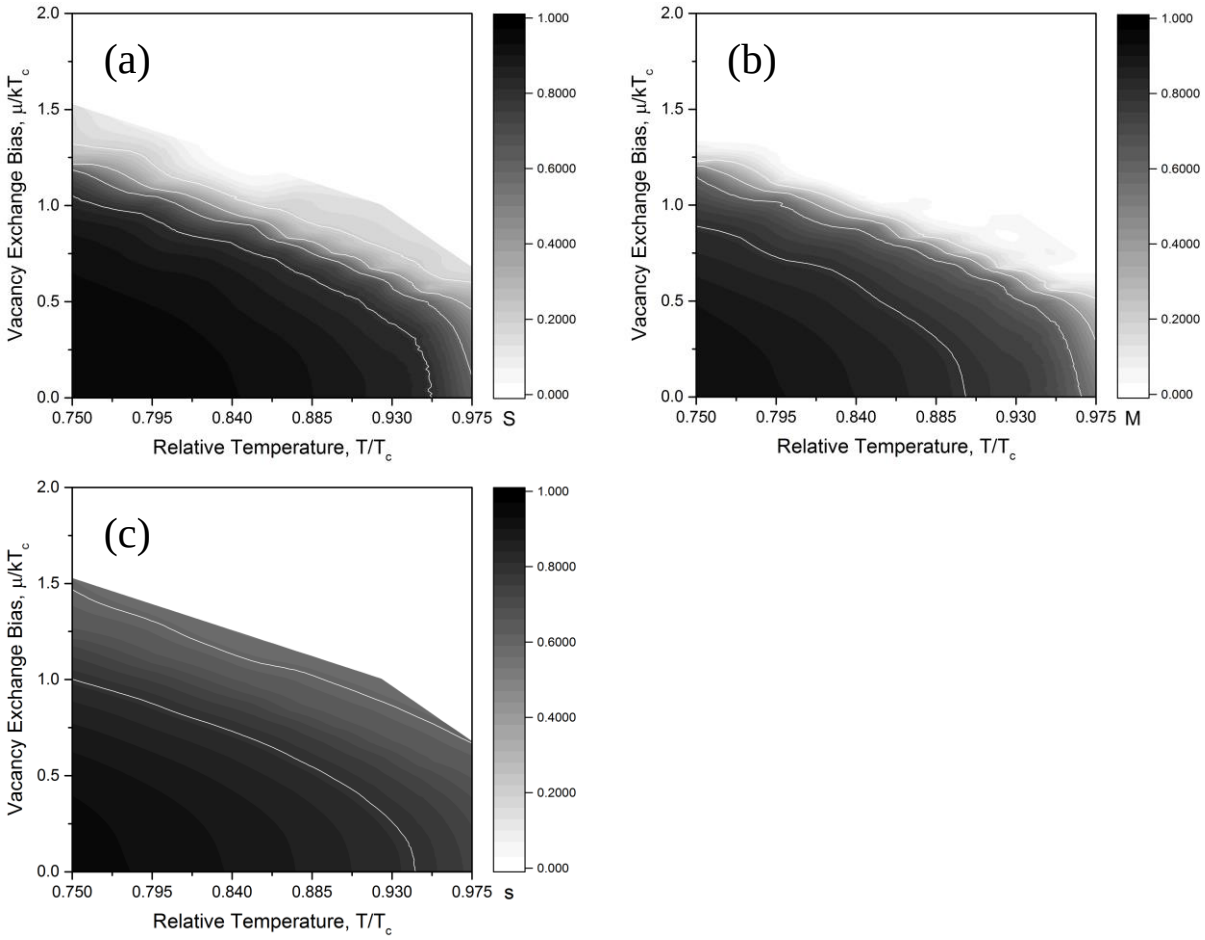

Figure 3.7: Variations in (a) long range order parameter, S; (b) net magnetization, M; and (c) short range order parameter, s across 490 temperature and imposed bias, μ, conditions. White contour lines are added at 20% decreases in the parameters.

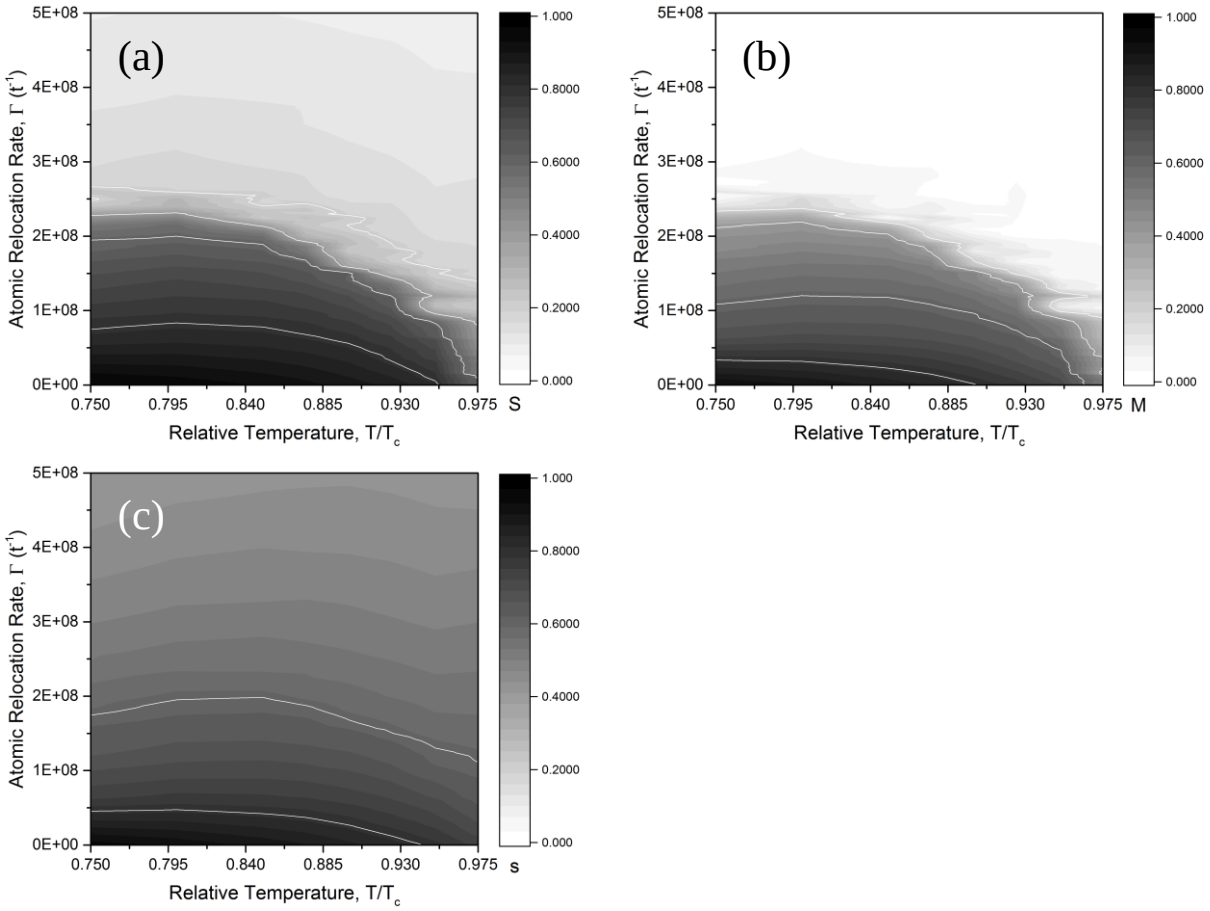

Figure 3.8: Variations in (a) long range order parameter, S; (b) net magnetization, M; and (c) short range order parameter, s, across 540 temperature and imposed atomic relocation rate, $\dot{\phi}$, conditions. White contour lines are added to highlight 20% decreases in the parameters.

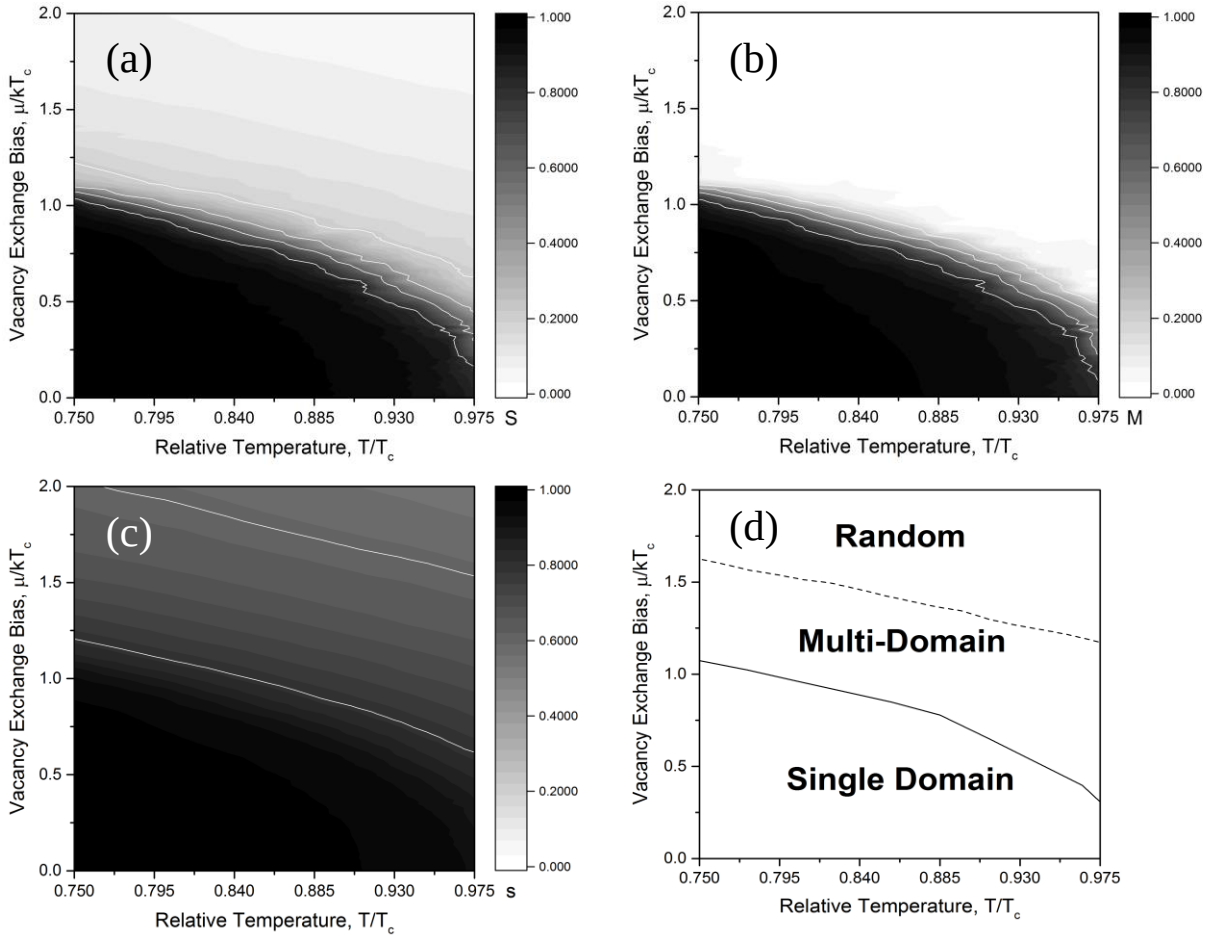

Figure 3.9: Variations in (a) long range order parameter, S; (b) net magnetization, M; and (c) short range order parameter, s across 530 temperature and imposed bias, μ, conditions. White contour lines are added to highlight 20% decreases in the parameters. (d) Boundaries between observed single domain, multi-domain, and random microstructures.

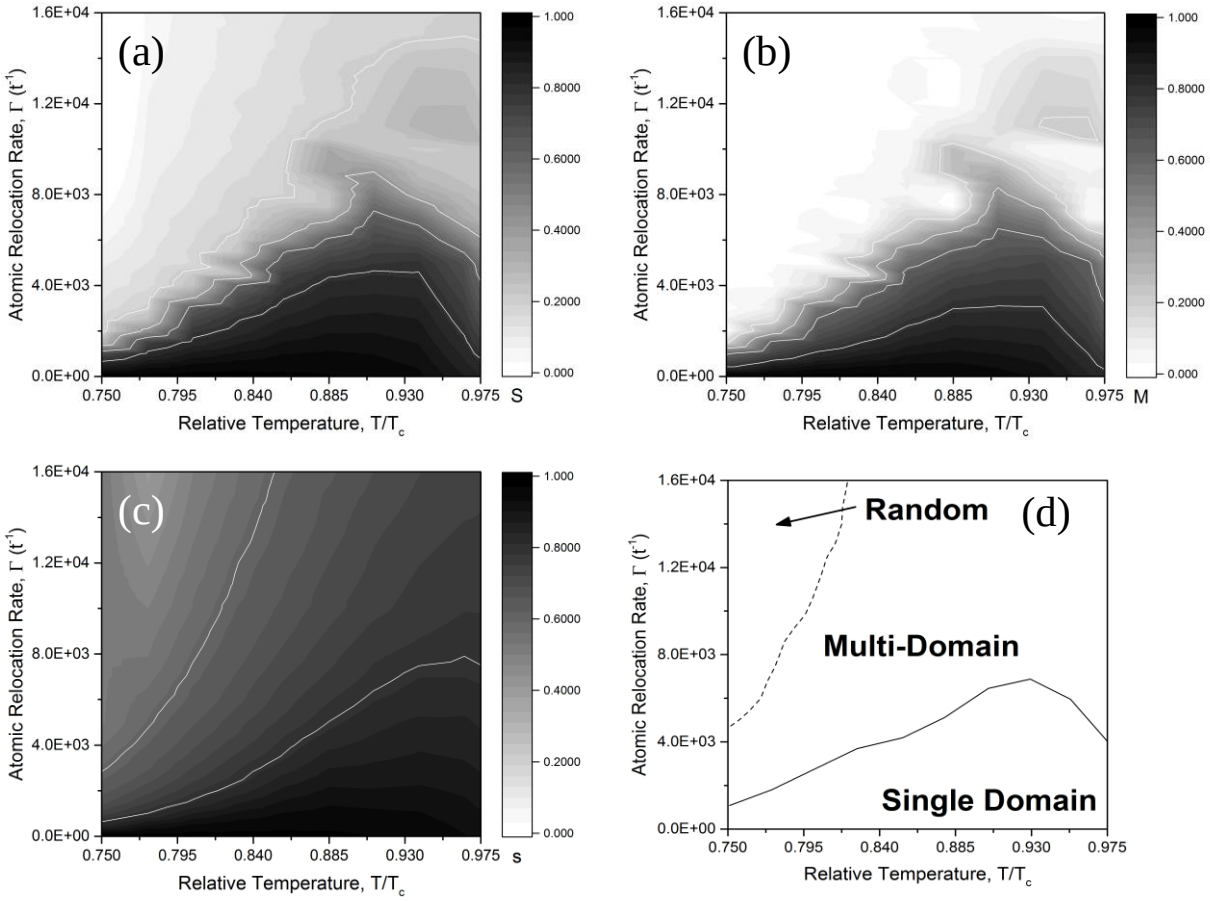

Figure 3.10: Variations in (a) long range order parameter, S; (b) net magnetization, M; and (c) short range order parameter, s, across 340 temperature and imposed atomic relocation rate, $\dot{\phi}$, conditions. White contour lines are added to highlight 20% decreases in the parameters. (d) Boundaries between observed single domain, multi-domain, and random microstructures.

The disordering behaviors of the $R = 0.45$ alloy were further studied to determine the order of the observed transitions between the single and multi-domain microstructures. The order of the transition was probed through a form of hysteresis testing, in which equilibrium ordered and random configurations were held at constant temperatures and allowed to evolve with increasing and decreasing imposed rates of disordering, respectively. The time between changes in the imposed rates of disordering was intentionally shortened, in comparison to the systematic study described above, in order to prevent the configurations from reaching the true steady state and thus to widen any perceived hysteresis. Traces of S during two such tests are shown in Figure 3.11 for a system of size $L = 128$ at $0.75T_c$ and $0.95T_c$, showing a clear hysteresis effect at both temperatures. This suggestion of a first order-like transition is consistent with the emergence and evolution of the multi-domain microstructure observed from atomic configurations, originating with the nucleation of ordered, anti-phase domains and propagating through the movement and growth of anti-phase boundary interfaces. Unfortunately, limitations of the current KMC method prevent exploration of this effect below ~$0.6T_c$, and a full understanding of the role of temperature on the transition thus remains elusive.

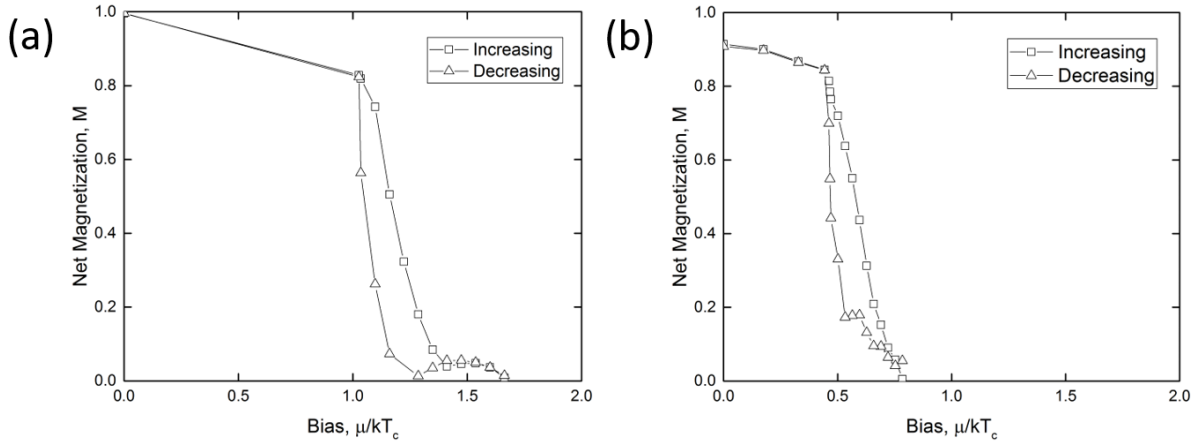

Figure 3.11: Hysteresis tests of a simulated alloy with $J_1 = -0.20$ eV and $J_2 = -0.09$ eV at $0.75T_c$ and $0.94T_c$.

In addition to stabilizing a multi-domain ordered microstructure, the behavior of the $R = 0.45$ alloy raises two important points. First, the behavior seems insensitive to the disordering mechanism used, as can be seen from a comparison of the results obtained with only an imposed bias on atom-vacancy exchanges versus those with only forced atomic relocations, Figure 3.6. Further, we performed simulations where the imposed bias on atom-vacancy exchanges, μ, was switched randomly between positive and negative values, for a given $|\mu|$. These tests with modified μ produced comparable disordering and patterning, seen in Figure 3.12, without a net flux of vacancies. Moreover, the behavior was found to be unique to the $R = 0.45$ alloy among those tested. Alloys with R values of 0, 0.10, or 0.30 displayed only single domain behavior, gradually filling with anti-site defects until completely randomized. Taken together, these points strongly suggest that a critical effect of the $R = 0.45$ energetics gives rise to this interesting patterning behavior, rather than nuances of the disordering mechanism.

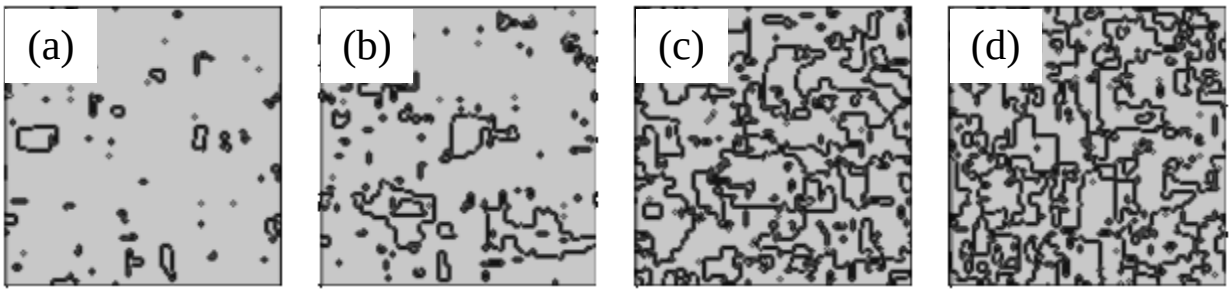

Figure 3.12: Atomic configurations of the $R = 0.45$ alloy under imposed disordering at $0.94T_c$, shaded such that sites where $s = 1$ are bright and $s < 1$ are dark. The bias values, $|\mu|/kT_c$, are (a) 0, (b) 0.3, (c) 0.5, and (d) 0.8.

As patterning of chemical order was observed independent of the disordering mechanism and only for the $R = 0.45$ alloy, we next examine the relationship between anti-site defect energies and R. The excess energy of an isolated anti-site defect, ΔE^{1as}, can be computed for a generic two dimensional, square alloy with first and second nearest neighbor interactions by counting the change in bonds for an anti-site in an otherwise fully ordered neighborhood,

$$\Delta E^{1as} = 4\left[\left(\epsilon_{xx}^{(1)} - \epsilon_{ab}^{(1)}\right) + \left(\epsilon_{ab}^{(2)} - \epsilon_{yy}^{(2)}\right)\right] \tag{3.8a}$$

where x is the species of an anti-site defect located on a y species sublattice site. Using Equation 3.2 and our selection of energetic parameters $\epsilon_{aa}^{(s)} = \epsilon_{bb}^{(s)} = 0$, Equation 3.8a is reduced to,

$$\Delta E^{1as} = 2J_2 - 2J_1 \tag{3.8b}$$

While the excess energy for two such isolated defects is simply $4J_2 - 4J_1$, simple bond counting shows that the excess energy for the same defects as first nearest neighbors is,

$$\Delta E_{nn}^{2as} = 4J_2 - 3J_1 \tag{3.9}$$

Thus, Equation 3.9 predicts an attractive interaction between anti-site defects in all but the $R = 0$ simulated alloy.

Because such anti-site pairs are structurally equivalent to the smallest repeating unit of a (10) anti-phase boundary, the predominant form in the $R = 0.45$ alloy, the boundary energy per unit length can be deduced as,

$$\gamma_{apb}^{(10)} = -\frac{J_1(1 - 2J_2/J_1)}{2a} \tag{3.10}$$

where a is the atomic spacing of the lattice. $\gamma_{apb}^{(10)}$ can thus be shown to vanish with $R \to 0.5$, while ΔE^{1as} in Equation 3.8 remains finite. This dependence has a particularly strong effect on the approximate cost of nucleating new, fully ordered domains,

$$\Delta E_{apd} \propto \gamma_{apb}^{(10)} r - \Delta E^{1as} C_{as}^{ss} r^2 \tag{3.11}$$

where the first term accounts for the addition of anti-phase boundary interface around the new domain of size r, and the second represents excess energy removed by eliminating the

concentration of anti-site defects, C_{as}^{ss}, where the domain forms. Although this crude approximation ignores the continuous production of anti-site defects and neglects the dynamical elimination of the same at pre-existing anti-phase boundaries, it suggests that sufficiently large C_{as}^{ss} is required to initiate nucleation, and that this critical concentration decreases with decreasing $\gamma_{apb}^{(10)}$, as is the case in $R = 0.45$ alloys. This picture is similar to a model proposed by Imry and Ma [26] for finite-sized spin domain formation in random-field Ising models, and it also presents similarities with the well-studied dynamical recovery in plastically strained polycrystals. In the latter case, the excess energy of dislocations is reduced as those with same-signed Burgers vectors organize to form low-energy boundaries through glide and climb. Such cooperative behavior interacts dynamically with continuous plastic deformation to produce a stable grain size at elevated temperatures [27].

3.2.2. Domain Stability

Given the apparent role of anti-phase boundary and anti-site defect energetics in the patterning of the $R = 0.45$ alloy under imposed disordering, we investigated the annealing behavior of ordered, anti-phase domains in our simulated alloys relative to general theories of coarsening and interface movement. The first of these tests focused on equilibrium annealing compared to the coarsening model described by Allen and Cahn [28, 29]. Such behavior is commonly described by,

$$r - r_0 = Ct^m \tag{3.12}$$

where r and r_0 are the current and initial domain radius, respectively, C is a constant, t is the annealing time, and m is a parameter which takes an ideal value of 0.5 in the Allen-Cahn theory. Configurations for the tests were created from a fully ordered, 2x2 lattice by replacing A atoms in

a circular region with B atoms and vice versa. These anti-phase domains were then annealed at $0.75T_c$ without imposed disordering, leading to gradual reductions in domain size and ultimately a single domain microstructure. Anti-phase domains in the $R = 0$ and $R = 0.45$ alloys are shown at various stages of this annealing in Figure 3.13 and Figure 3.14, respectively. The configurations reveal an irregular, protruding shape for the shrunken domains in the $R = 0$ alloy, in contrast to a notable faceting of the domains in the $R = 0.45$ alloy. These differences in appearance can be rationalized in terms of the current simulation method, the use of vacancy-atom exchanges for thermal diffusion gives rise to protrusions and anisotropic annealing, and previously discussed energetics near $R = 0.5$, in particular the relatively small value of $\gamma_{apb}^{(10)}$ for the $R = 0.45$ alloy. Changes in domain area for these alloys are shown in Figure 3.15 and Figure 3.16 as a function of simulated time and show an approximately linear relationship between area ($A \propto r^2$) and time for both alloys, consistent with the Allen-Cahn model. Additional annealing tests were conducted at temperatures as low as $0.5T_c$ without significant changes to the irregularity or faceting of the anti-phase domains and only minor differences in the measured exponent m, 0.53 to 0.51 for $R = 0$ and 0.63 to 0.45 for $R = 0.45$.

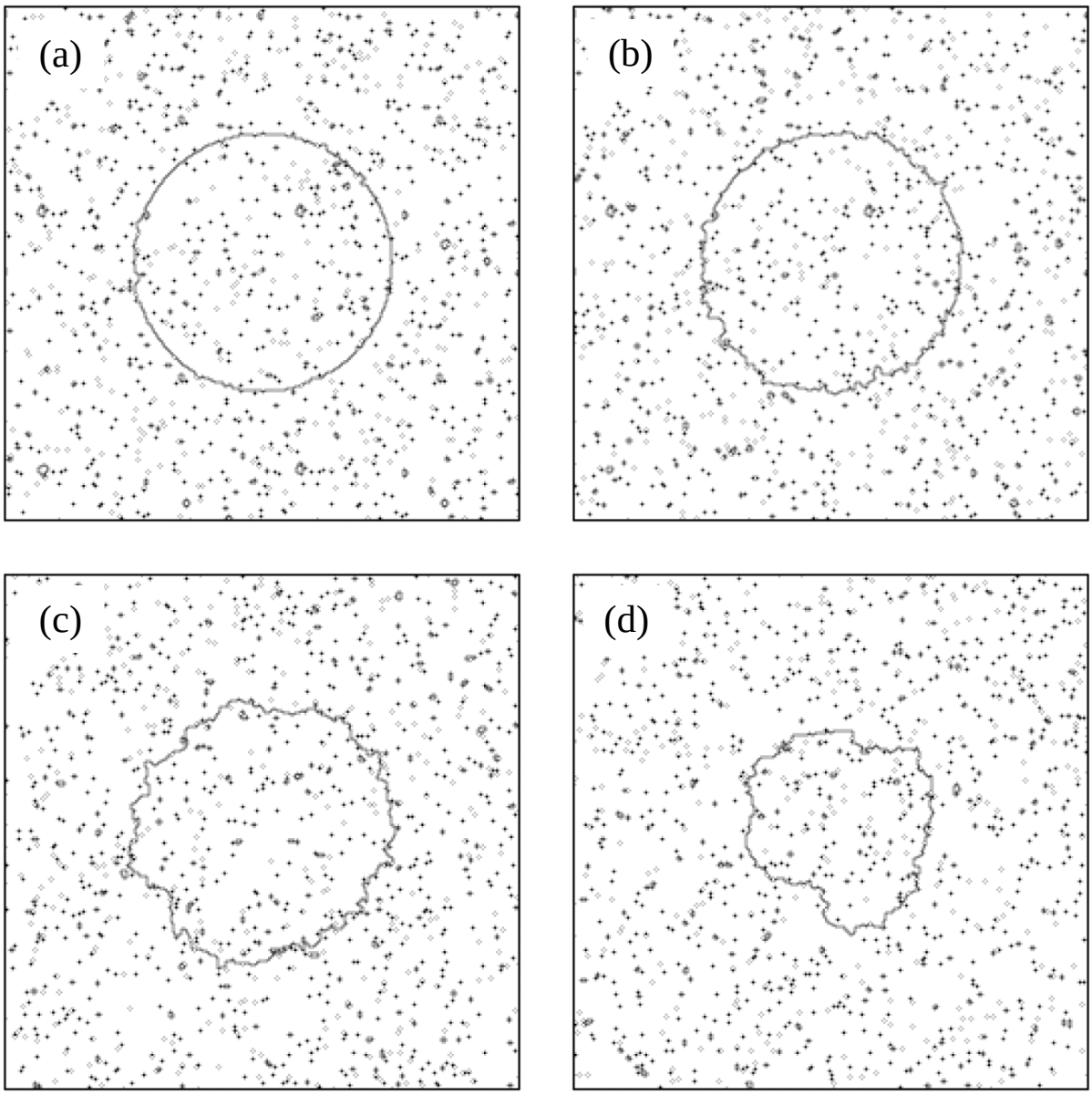

Figure 3.13: Annealing of an imposed anti-phase domain at $0.75T_c$ *for a simulated alloy with* $J_1 = -0.2$ eV *and* $J_2 = 0$ eV. *Configurations were recorded at (a) 0.5, (b) 5, (c) 50, and (d) 500 Monte Carlo steps per site. Shading is done according the of s value at each site, while the numerous spots in the configurations are anti-site defects (black) and excess vacancies (grey) added to the system.*

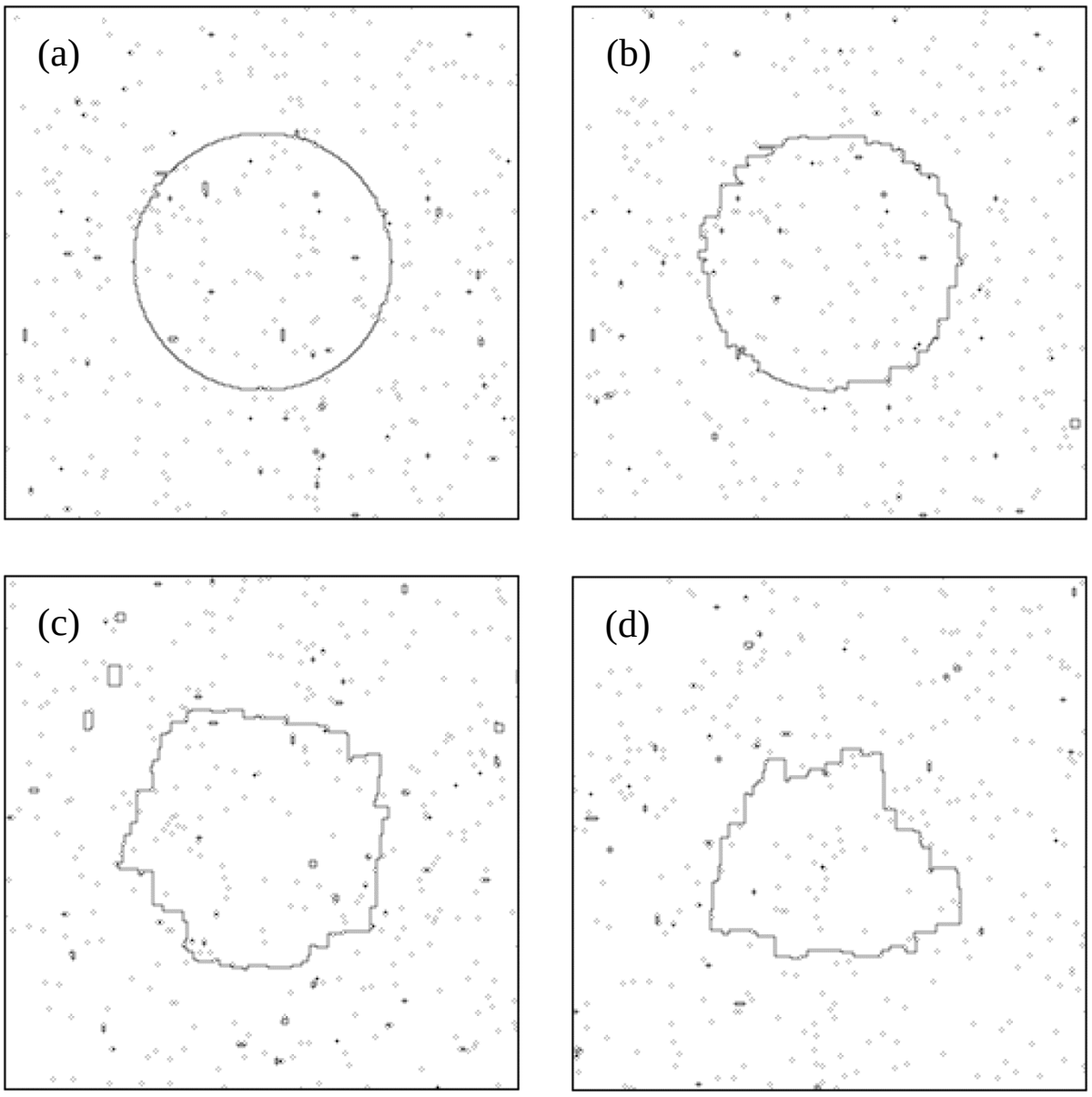

Figure 3.14: Annealing of an imposed anti-phase domain at $0.75T_c$ *for a simulated alloy with* $J_1 = -0.20$ eV *and* $J_2 = -0.09$ eV. *Configurations were recorded at (a) 3, (b) 30, (c) 300, and (d) 3000 Monte Carlo steps per site. Note the early signs of faceting in (b) and the almost square domain in (d). Shading is done according the of s value at each site, while the numerous spots in the configurations are anti-site defects (black) and excess vacancies (grey) added to the system.*

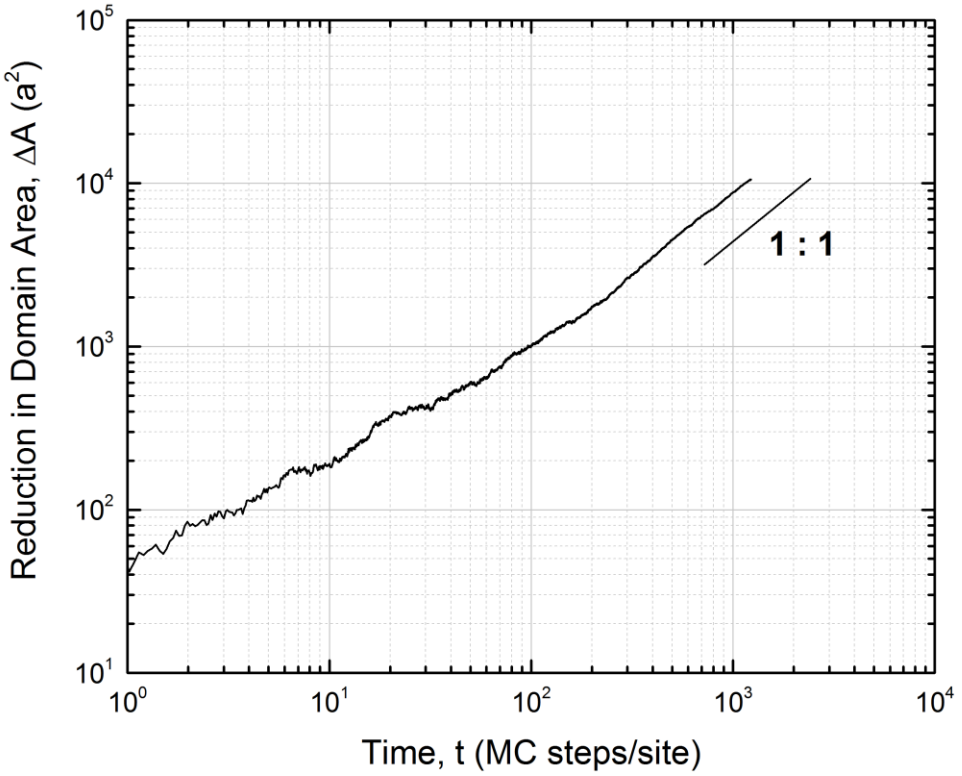

Figure 3.15: Reduction in test domain area with annealing time for the $R = 0$ alloy at $0.75T_c$. Time is given in terms of Monte Carlo steps per lattice site, and a slope of 1 is included for reference.

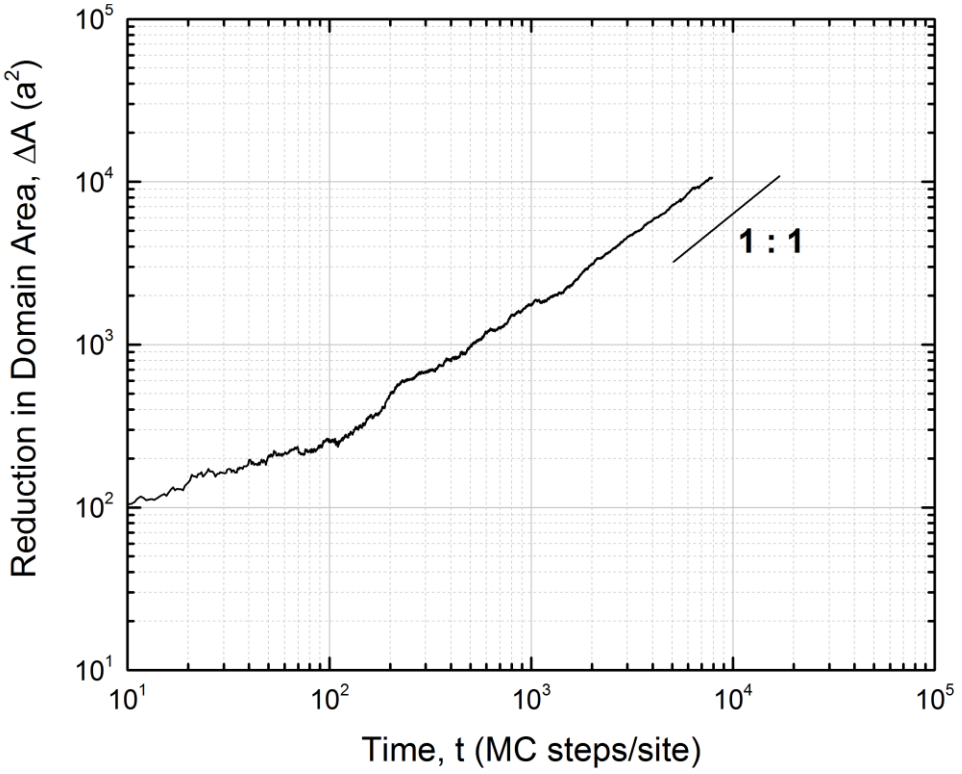

Figure 3.16: Reduction in test domain area with annealing time for the $R = 0.45$ alloy at $0.75T_c$. Time is given in terms of Monte Carlo steps per lattice site, and a slope of 1 is included for reference.

Additional simulations were performed to determine the dependence of anti-phase boundary migration on anti-site defect concentrations. As with the annealing tests described above, configurations were created by switching the ordered variant of a select region of the lattice. Here, however, the circular shape was replaced by a rectangular anti-phase domain running from one y periodic boundary to the other, $\lesssim 0.5L$ in width, and centered at $x = 0.5L$. Excess anti-site defects for the test were then added to the configuration to create symmetric gradients, ∇X_{as}, in their concentration, crossing the anti-phase boundaries and peaked at $x = 0.5L$. This band-like anti-phase domain was annealed while forcibly maintaining ∇X_{as}, allowing us to measure the impact on anti-phase boundary velocity through changes in domain area with time. While this measurement is straightforward, care was taken to address two principle concerns. As for the previous annealing tests, the measured displacement of the anti-phase boundaries was averaged over many simulations to remove any possible anomalies from particular arrangements of vacancies or anti-site defects. Further, boundary velocity calculations were limited to the first ~10% of displacement measurements in order to avoid confounding the effects of ∇X_{as} with those of increasing boundaries roughness. Average boundary velocities for the $R = 0.45$ alloy at $0.75T_c$ are presented in Figure 3.17 as a function of ∇X_{as}. While there is a clear increase in average boundary velocity with increasing ∇X_{as}, the expected linear regime is not apparent. This could be an artifact of the systems simulated here, or the range of ∇X_{as} for linear response may simply be too short to be captured in the data collected for the present work.

Taken together, these annealing behaviors help to further explain the origins of patterning in the $R = 0.45$ alloy and, by connection, shed light on the formation of new domains during the *in situ* experiments on Cu_3Au described in the preceding. Tests of circular domains clearly show an adherence to the model described by Allen and Cahn for the range of temperatures studied here,

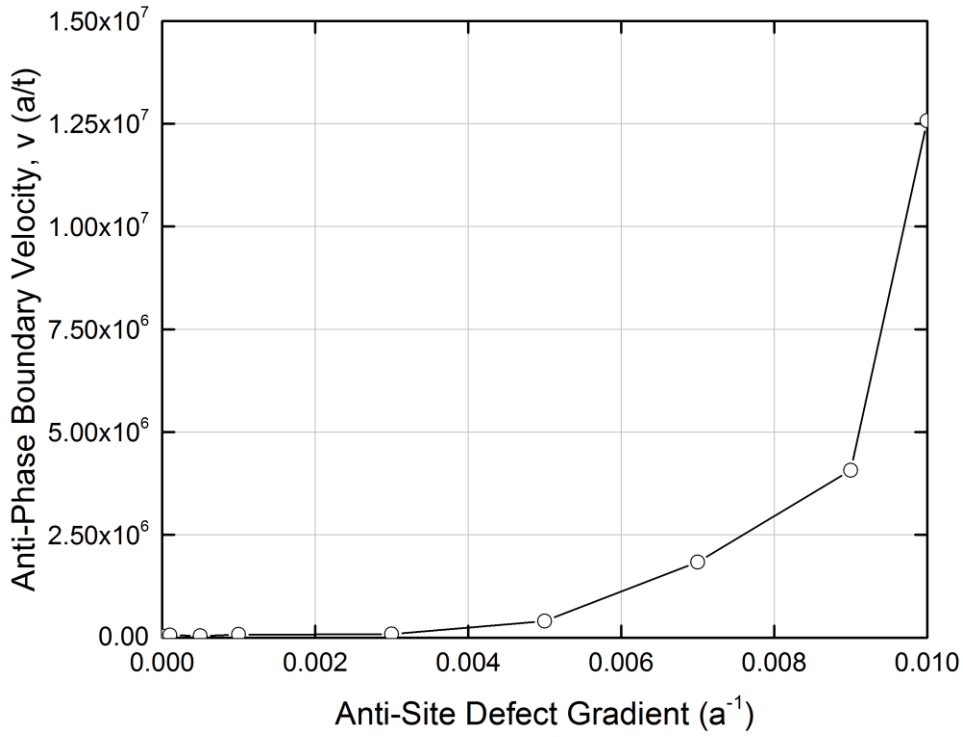

Figure 3.17: Average anti-phase boundary velocity as a function of the gradient in anti-site defect concentration across the boundary.

$0.7T_c < T < 1.1T_c$, despite the often irregular or faceted shapes of the anti-phase domains. This suggests that the competing anti-phase domains of patterned, multi-domain microstructures may be treated according to the same general theories that govern domain and grain boundaries in other systems. Moreover, our tests of anti-phase boundary annealing in the presence of non-equilibrium anti-site defect concentrations provide evidence of a sensitivity to gradients in anti-site concentration, drawing the boundaries into neighboring, less ordered domains. This point is best understood by considering the role of vacancies in anti-phase boundary migration. When such a boundary divides two highly ordered domains, vacancies must reorganize atoms along the boundary through complex chains of vacancy-atom exchanges – a process that is inefficient and reversible under most conditions. The addition of anti-site defects near the anti-phase boundary, however, alters this situation: 1) by lowering the effective ordering energy near such defects and allowing the vacancy to more easily create temporary anti-sites without immediately recovering

the same; and 2) by providing atoms which may be drawn directly into the anti-phase boundary without the energetic penalty of breaking A-B bonds to their neighbors.

Based on these findings, we propose an expansion to our rationalization of patterning. Let us take, as an example, a new, fully ordered anti-phase domain formed when a critically large, local concentration of anti-site defects collapses due to the energetics described in the previous section. Under equilibrium conditions, this new domain would anneal away, removing the small, but still existent, interfacial energy of its anti-phase boundary and recovering the single domain microstructure. If the difference in anti-site defect content is sufficient between the domain and its surroundings, however, the effective gradient will bias migration of the anti-phase boundary outward, growing the domain. It is this competition between shrinkage, driven by equilibrium annealing, and expansion, driven by excess anti-site defects generated by imposed disordering, which divides the observed single and multi-domain microstructures, as the imposed disordering rate must be sufficient to create anti-site defects not only for nucleation, but also for growth of new domains. However, this picture of patterning is still missing one important aspect: the reduction in average domain size with imposed disordering beyond the single to multi-domain transition. While newly formed domains are initially free of anti-site defects, their order is reduced as our imposed disordering mechanisms continuously introduce anti-site defects throughout the microstructure. This diminishes the effective gradient in anti-site defect concentration across newer anti-phase boundaries, ultimately eliminating the preferential growth of their domains. The average domain size is thus driven down, as higher imposed rates of disorder lead to greater rates of domain nucleation and shorter periods of accelerated growth.

3.2.3. Comparison to *In Situ* Observations

The patterning of order described in preceding sections is both similar and different to the domain nucleation observed *in situ* for Cu_3Au under Ne^+ irradiation (see Section 2.4). Both phenomena occur only under sufficient disordering at a given temperature, as shown in Figure 2.13 and Figure 3.10, and this critical disordering increases in both cases as defects become more active at higher temperatures. Freshly nucleated anti-phase domains in Cu_3Au, however, are typically ~20 nm in diameter, compared to 10-20 nearest neighbor distances (~5 nm) in the $R = 0.45$ simulated alloy. New domains in Cu_3Au are also found most commonly along previously existing anti-phase boundaries, while those in the simulated alloy appear from the interiors of existing domains. These differences, however, are easily explained by aspects of the experimental and simulation methods employed here. Sufficiently small anti-phase domains, for example, would not be observable using our superlattice, dark-field imaging technique due to their low contrast relative to the foil thickness. The differences in location can similarly be explained by our choice of the 2x2 ordered structure for the simulated alloys: with only two ordered variants, domains nucleating too close to an existing anti-phase boundary would be certain to merge with the neighboring domain. The similarities between our simulations of disordering and *in situ* experimental observations are thus more significant than the cosmetic differences in ordered microstructure and support our initial hypothesis that new domains in Cu_3Au nucleate in response to critically large densities of radiation-induced anti-site defects.

Beyond the origin of domain nucleation, however, these similarities suggest that the ordered microstructure of Cu_3Au could undergo a similar patterning reaction to that observed for the $R = 0.45$ simulated alloy. The key question then is whether anti-phase boundary behavior in

our simulated alloys is applicable to the $L1_2$ structure of Cu_3Au. Recent work by Gorbatov, *et al.* [30] describes the per site energy of ordered Cu_3Au as,

$$E_{ord} = -\frac{3}{16}(2V_1 - 3V_2 + 4V_3) \tag{3.13}$$

and the interfacial energy for the equivalent (100) anti-phase boundary as,

$$\gamma_{apb}^{(100)} = \frac{-V_2 + 4V_3}{a^2} \tag{3.14}$$

where V_i terms represent the $i$the neighbor ordering energy and a is the lattice parameter. Because the first nearest neighbor ordering energy, V_1, in Cu_3Au is known to be a factor ~10 larger than either V_2 or V_3 [19], $\gamma_{apb}^{(100)}$ is likely quite small compared to E_{ord}, and our physical picture of the patterning reaction is thus plausible for Cu_3Au.

Initial disordering rates for the $R = 0.45$ simulated alloy, shown in Figure 3.4, also possess strong similarities to our experimental measurements in Cu_3Au at temperatures approaching T_c (see Section 2.3). While it is thus tempting to draw on these parallels as evidence of common physical processes, further work will be required to provide specific support. Three-dimensional simulations of the $L1_2$ ordered structure are of particular interest in this regard, especially with respect to those ballistic mixing effects which lead to constant disordering at low temperatures.

3.3. CONCLUSIONS

This simulation study was carried out in response to anomalous disordering behavior observed in Cu_3Au under light ion irradiation, including increased rates of initial disordering neat T_c and the formation of new anti-phase domains with certain combinations of dose rate and temperature. Disordering mechanisms were implemented to directionally bias the rates of atom-

vacancy exchanges and to forcibly relocate atoms with their neighbors. Simulations were conducted on alloys with varying ratios of first and second nearest neighbor energies, $R = J_2/J_1$, including 0, 0.1, 0.3, and 0.45. While the behavior of the first three alloys under increasing imposed rates of disorder resembled their order-disorder behavior with increasing temperature, the behavior of the $R = 0.45$ alloy was more complex. At increasing imposed disordering rates, we observed a clear transition of the ordered microstructure from a single domain populated with anti-site defects to a multi-domain structure composed of competing, highly ordered domains. Systematic investigation revealed a continuous boundary in temperature and imposed disordering rate between these two microstructures. Further increases in imposed disordering rate beyond this transition lead to gradually smaller ordered domain sizes, until the ordered microstructure is indistinguishable from a random lattice. The insensitivity of the above behavior to the disordering mechanism used and the appearance of it only in the simulated alloy nearest a ground state boundary, $R = 0.5$, suggest that the energetics of the alloy are the critical factor in these disordering effects. Consideration of the excess energy of isolated anti-site defects and anti-phase boundary interfaces supports this finding, as the interfacial energy of an anti-phase boundary can be shown to decrease to zero when approaching the boundary between ground states. This would provide a significant driving force to replace regions of isolated anti-site defects with highly ordered anti-phase domains, as seen in the multi-domain microstructure.

Further study of these anti-phase boundaries allowed us to refine the above picture. Simulated annealing of anti-phase domains in these alloys suggests that irregularities in domain shape and faceting of boundaries do not cause significant deviations from the model described by Allen and Cahn over the range of temperatures studied here, and thus that anti-phase boundaries can be analyzed at equilibrium along similar lines as grain boundaries. Moving beyond equilibrium

involved annealing these domains in the presence of an imposed gradient of anti-site defects and revealed that anti-phase boundaries migrate more quickly as this gradient increases. Together, these findings and the energetic considerations noted above create a fuller picture of patterning in these alloys. For alloys near the ground state boundary, sufficient local concentrations of anti-site defects may collapse to form small, fully ordered anti-phase domains. The anti-phase boundaries of these domains are then drawn outward as surrounding anti-site defects increase boundary migration versus the equilibrium drive to anneal away. This accelerated domain growth continues until the differences in anti-site defect content are resolved, either by collision with another highly ordered anti-phase domain or by continuous introduction of defects into the domain by our imposed disordering mechanisms. This recurring cycle of nucleation and growth leads to a steady state domain size dependent on the rate of domain nucleation and how quickly the anti-site gradient is diminished, thus explaining the patterned multi-domain states observed and their gradual decay toward a random microstructure with extreme imposed disordering.

3.4. REFERENCES

[1] J. Ye, J.-w. Liu, R. A. Enrique, and P. Bellon, "Compositional and order patterning in driven alloys: the role of external-forcing characteristic lengths," *Scripta Materialia,* vol. 49, pp. 969-975, 2003.

[2] R. A. Enrique and P. Bellon, "Compositional patterning in systems driven by competing dynamics of different length scales," *Physical Review Letters,* vol. 84, pp. 2885-2888, 2000.

[3] K. C. Russell, "Precipitate nucleation during irradiation," in *Phase Stability during Irradiation*, Warrendale, Pa, USA, 1981, pp. 507-519.

[4] J. Ye and P. Bellon, "Nanoscale patterning of chemical order induced by displacement cascades in irradiated alloys. I. A kinetic Monte Carlo study," *Physical Review B,* vol. 70, 2004.

[5] J. Ye and P. Bellon, "Nanoscale patterning of chemical order induced by displacement cascades in irradiated alloys. II. Analytical modeling," *Physical Review B,* vol. 70, 2004.

[6] J. Ye and P. Bellon, "Nanoscale patterning of chemical order induced by displacement cascades in irradiated $L1_0$ alloys: Scaling analysis of the fluctuations of order," *Physical Review B,* vol. 73, 2006.

[7] J. Ye, Y. Li, R. Averback, J.-M. Zuo, and P. Bellon, "Atomistic modeling of nanoscale patterning of $L1_2$ order induced by ion irradiation," *Journal of Applied Physics,* vol. 108, p. 054302, 2010.

[8] E. Ising, "Contribution to the theory of ferromagnetism," *Zeitschrift für Physik,* vol. 31, 1925.

[9] R. A. Enrique and P. Bellon, "Compositional patterning in immiscible alloys driven by irradiation," *Physical Review B,* vol. 63, 2001.

[10] C. P. Flynn, *Point Defects and Diffusion*. Oxford: Clarendon Press, 1972.

[11] J.-M. Roussel and P. Bellon, "Vacancy-assisted phase separation with asymmetric atomic mobility: Coarsening rates, precipitate composition, and morphology," *Physical Review B,* vol. 63, 2001.

[12] S. Shu, P. Bellon, and R. S. Averback, "Complex nanoprecipitate structures induced by irradiation in immiscible alloy systems," *Physical Review B,* vol. 87, 2013.

[13] G. Martin and P. Bellon, "Driven Alloys," *Solid State Physics,* vol. 50, pp. 189-327, 1996.

[14] A. B. Bortz, M. H. Kalos, and J. L. Lebowitz, "A new algorithm for Monte Carlo simulation of Ising spin systems," *Journal of Computational Physics,* vol. 17, pp. 10-18, 1975.

[15] F. Soisson and C.-C. Fu, "Cu-precipitation kinetics in α−Fe from atomistic simulations: Vacancy-trapping effects and Cu-cluster mobility," *Physical Review B,* vol. 76, 2007.

[16] Y. S. Lee, "Atomic transport mechanisms in irradiated Cu_3Au," Doctor of Philosophy, Physics, University of Illinois at Urbana-Champaign, Urbana, Illinois, 1996.

[17] E. A. Lang, "Radiation Damage and Radiation Induced Order-Disorder Transformations in Cu_3Au," Master of Science, Materials Science and Engineering, University of Illinois at Urbana-Champaign, Urbana, Illinois, 2000.

[18] H. A. Bethe, "Statistical theory of superlattices," *Proceedings of the Royal Society A: Mathematical, Physical and Engineering Sciences,* vol. 150, pp. 552-575, 1935.

[19] J. M. Cowley, "An Approximate Theory of Order in Alloys," *Physical Review,* vol. 77, pp. 669-675, 1950.

[20] K. Binder, "Critical Properties from Monte Carlo Coarse Graining and Renormalization," *Physical Review Letters,* vol. 47, pp. 693-696, 1981.

[21] K. Binder, "Monte Carlo simulations of alloy phase transformations," in *Statics and Dynamics of Alloy Phase Transformations*, P. E. A. Turchi and A. Gonis, Eds., ed New York: Plenum Press, 1994, pp. 467-.

[22] S. Jin, A. Sen, and A. W. Sandvik, "Ashkin-teller criticality and pseudo-first-order behavior in a frustrated Ising model on the square lattice," *Phys Rev Lett,* vol. 108, p. 045702, Jan 27 2012.

[23] K. Binder and D. P. Landau, "Phase diagrams and critical behavior in Ising square lattices with nearest- and next-nearest-neighbor interactions," *Physical Review B,* vol. 21, pp. 1941-1962, 1980.

[24] A. Kalz, A. Honecker, S. Fuchs, and T. Pruschke, "Monte Carlo studies of the Ising square lattice with competing interactions," *Journal of Physics: Conference Series,* vol. 145, p. 012051, 2009.

[25] B. L. Welch, "The generalization of 'Student's' problem when several different populations variances are involved," *Biometrika,* vol. 34, pp. 28-35, 1947.

[26] Y. Imry and S.-k. Ma, "Random-Field Instability of the Ordered State of Continuous Symmetry," *Physical Review Letters,* vol. 35, pp. 1399-1401, 1975.

[27] J. Le`pinoux and L. P. Kubin, "The dynamic organization of dislocation structures, A simulation," *Scripta Metallurgica,* vol. 21, pp. 833-838, 1987.

[28] S. M. Allen and J. W. Cahn, "A microscopic theory for antiphase boundary motion and its application to antiphase domain coarsening," *Acta Metallurgica,* vol. 27, pp. 1085-1095, 1979.

[29] J. W. Cahn and S. M. Allen, "A microscopic theory for domain wall motion and its experimental verification in Fe-Al alloy domain growth kinetics," *Le Journal de Physique Colloques,* vol. 38, pp. C7-51-C7-54, 1977.

[30] O. I. Gorbatov, I. L. Lomaev, Y. N. Gornostyrev, A. V. Ruban, D. Furrer, V. Venkatesh, *et al.*, "Effect of composition on antiphase boundary energy in Ni_3Al based alloys: *Ab initio* calculations," *Physical Review B,* vol. 93, 2016.

CHAPTER 4

CONCLUSIONS

In this dissertation we have studied the effects of temperature and disordering rate on the ordered microstructures of real and simulated binary alloys. Electron diffraction and dark-field transmission microscopy experiments were carried out *in situ* under light-ion irradiation of Cu_3Au, while disorder in two-dimensional AB alloys was imposed by biased vacancy diffusion or the forced replacement of atoms. For both studies, disordering near the temperature, T_c, for the equilibrium order-disorder transition was of particular interest, and previously unreported behavior was observed.

Our study of radiation-induced disordering in Cu_3Au was prompted by reports [1, 2] of anomalous, temperature dependent disordering rates near T_c, and a similar, if steeper, trend was reproduced using electron diffraction for Cu_3Au foils irradiated at temperatures approaching the transition. The dose rate independence of these measurements and of the preceding study suggest that mobile but isolated point defects are responsible for increases in $dS/Sd\phi$, and free energy calculations verify that sufficient driving force exists in radiation-induced supersaturations of point defects to account for the observed disordering. While this dissertation verifies that previous reports are not simply artifacts of resistivity measurement, the detailed mechanism for this coupling between defects and disordering remains unexplained.

The steady state of the Cu_3Au foils was studied in addition to the initial disordering described above, using superlattice dark-field imaging to observe damage to the ordered microstructure. Micrographs and video recordings taken under various combinations of irradiation

temperature and dose rate conditions reveal unexpected alterations to this microstructure, in addition to the transient disordered zones reported by Jenkins, *et al.* [3, 4]. These alterations appear to form through the nucleation of small ordered domains within the microstructure, sometimes leading to roughening of existing anti-phase domains. Further, the results suggest that this nucleation process is dependent on the irradiation condition, occurring only at sufficiently low temperature or sufficiently high dose rate. We present a map of this behavior over the irradiation conditions studied and attribute the behavior to the collapse of critically large, local densities of anti-site defects into highly ordered new domains. This process is generally reminiscent of reported patterning of alloy composition [5-7] and order [8-10] under irradiation.

Our study of disordering in two-dimensional, ordered systems was carried out in response to the disordering behaviors of Cu_3Au, discussed above, and specifically to the hypothesis of Lee, *et al.* [2] that the effects could be attributed to unbalanced vacancy fluxes from collision cascades to defect sinks. Kinetic Monte Carlo simulations were thus performed on simplified, two-dimensional ordered alloys, labeled according to the ratio, $R = J_2/J_1$, of their first and second neighbor A-B interactions as 0, 0.1, 0.3, and 0.45. Imposing disorder in these alloys, either through bias on the rates of atom-vacancy exchange or forced replacement of atoms with their neighbors, revealed a significant dependence for disordering behavior on R. Simulations with R values of 0, 0.1, and 0.3 disordered similarly to their second-order transitions with temperature, smoothly transitioning from the 2x2 ordered state to the random state. For the $R = 0.45$ alloy, however, this transition occurs quickly and is marked by a sharp decrease in the "net magnetization" of the system. Atomic configurations from just above this transition reveal a division of the alloy into many competing, but highly ordered, domains. This multi-domain structure then transitions smoothly into the random state by a gradual reduction in domain size.

We show that the interfacial energy of the predominant (10) anti-phase boundaries, $\gamma_{apb}^{(10)}$, is very sensitive to the value of R for a given 2x2 alloy, vanishing at $R = 0.5$. Further simulations of annealing behavior in our simulated alloys reveal reasonable adherence to the behavior described by Allen and Cahn [11, 12], $\Delta L \propto \sqrt{t}$, for all alloys and $T > 0.5T_c$, despite evident faceting of domains in the $R = 0.45$ alloy. Combined with additional KMC simulations showing an acceleration of anti-phase boundary migration with a gradient in vacancy concentration, these findings allow use to create a physical picture of the multi-domain state, based on a cycle of nucleation, accelerated growth, and ultimate stabilization of anti-phase domains. Greater imposed disordering rates, beyond the critical value required to start the cycle, then lead to the gradual decrease in average domain size observed.

We further identify similarities between the onset of domain nucleation in our experimental specimens and simulated alloys. In both cases, nucleation is triggered by sufficiently high rates of disordering at a given temperature, with that rate increasing as defects become more active at elevated temperatures. These similarities support our initial hypothesis that experimentally observed domains result from critically high densities of radiation-induced anti-site defects, as attributed for the $R = 0.45$ simulated alloy. Further examination of the interfacial energy, $\gamma_{apb}^{(100)}$, for the dominant (100) anti-phase boundary in Cu_3Au indicates that the alloy may be subject to the same kind of patterning reaction described above.

For future studies of these disordering effects, we recommend production of microscopy foils along the more stringent specifications given by Jenkins, *et al.* [3, 4] for damage contrast studies in Cu_3Au. Such specimens would minimize projection effects between domains under prolonged irradiations, giving a much improved view of any patterned structure. If such structures

are observed *in situ*, two- and three-dimensional atomistic simulations, in the vein of those preformed here, could be paired with imaging for quantitative analysis and modeling of the patterning reaction.

4.1. REFERENCES

[1] E. A. Lang, "Radiation Damage and Radiation Induced Order-Disorder Transformations in Cu_3Au," Master of Science, Materials Science and Engineering, University of Illinois at Urbana-Champaign, Urbana, Illinois, 2000.

[2] Y. S. Lee, "Atomic transport mechanisms in irradiated Cu_3Au," Doctor of Philosophy, Physics, University of Illinois at Urbana-Champaign, Urbana, Illinois, 1996.

[3] M. L. Jenkins, K.-H. Katerbau, and M. Wilkens, "Transmission electron microscopy studies of displacement cascads in Cu_3Au: I. The diffraction contrast of disordered zones," *Philosophical Magazine*, vol. 34, pp. 1141-1153, 1976.

[4] M. L. Jenkins and M. Wilkens, "Transmission electron microscopy studies of displacement cascads in Cu_3Au: II. Experimental investigation of cascades produced by Cu ions," *Philosophical Magazine*, vol. 34, pp. 1155-1167, 1976.

[5] R. A. Enrique and P. Bellon, "Compositional patterning in systems driven by competing dynamics of different length scales," *Physical Review Letters*, vol. 84, pp. 2885-2888, 2000.

[6] R. A. Enrique and P. Bellon, "Compositional patterning in immiscible alloys driven by irradiation," *Physical Review B*, vol. 63, 2001.

[7] R. A. Enrique, K. Nordlund, R. S. Averback, and P. Bellon, "Nonequilibrium self-organization in alloys under irradiation leading to the formation of nanocomposites," *Nuclear Instruments and Methods in Physics Research Section B: Beam Interactions with Materials and Atoms*, vol. 202, pp. 206-216, 2003.

[8] J. Ye and P. Bellon, "Nanoscale patterning of chemical order induced by displacement cascades in irradiated alloys. I. A kinetic Monte Carlo study," *Physical Review B*, vol. 70, 2004.

[9] J. Ye and P. Bellon, "Nanoscale patterning of chemical order induced by displacement cascades in irradiated alloys. II. Analytical modeling," *Physical Review B*, vol. 70, 2004.

[10] J. Ye and P. Bellon, "Nanoscale patterning of chemical order induced by displacement cascades in irradiated $L1_0$ alloys: Scaling analysis of the fluctuations of order," *Physical Review B*, vol. 73, 2006.

[11] S. M. Allen and J. W. Cahn, "A microscopic theory for antiphase boundary motion and its application to antiphase domain coarsening," *Acta Metallurgica*, vol. 27, pp. 1085-1095, 1979.

[12] J. W. Cahn and S. M. Allen, "A microscopic theory for domain wall motion and its experimental verification in Fe-Al alloy domain growth kinetics," *Le Journal de Physique Colloques*, vol. 38, pp. C7-51-C7-54, 1977.

APPENDIX A

MATLAB DIGITIZATION SCRIPT

```
%% MAIN FUNCTION
function mass_digitizer
% MASS_DIGITIZER A function for digitizing curves across image sequences.

close all;
clear variables global;

global IMAGE;
global ROI;
global PROC;
global PEAK;

%% SETTING UP STRUCTURES
IMAGE=struct('path',[],'name',[],'type',[],'values',[]);
ROI=struct('left',[],'right',[],'bottom',[],'top',[], ...
           'y_type',[],'y_para',[],'y_pos1',[],'y_pos2',[], ...
           'y_val1',[],'y_val2',[],'y_span',[], ...
           'x_type',[],'x_para',[],'x_pos1',[],'x_pos2',[], ...
           'x_val1',[],'x_val2',[],'x_span',[]);
PROC=struc('t_low',[],'t_high',[],'dup_type',[]);
PEAK=struc('p_locs',[],'b_para',[],'x_axis',[]);

%% SELECTING FIRST IMAGE
[IMAGE.name,IMAGE.path,~]=uigetfile({'*.jpg;*.tif;*.png;*.gif', ...
                          'All Image Files';'*.*','All Files'}, ...
                          'Select the first image for calibration');
if isequal(IMAGE.name,0)
    uiwait(msgbox('No image selected. Exiting...','Failure','modal'));
    exit;
end
IMAGE.name=strcat(IMAGE.path,IMAGE.name);
IMAGE.type=strcat('\*',IMAGE.name(end-3:end));
IMAGE_LIST=dir([IMAGE.path,IMAGE.type]);

%% CROPPING TO JUST PLOT
IMAGE.values=imread(IMAGE.name);
figure
imshow(IMAGE.values);
ORIGIN=ginput(1);
ORIGIN=[round(ORIGIN(1)),round(ORIGIN(2))];
BASE_XRANGE=ORIGIN(1):size(IMAGE.values,2);
BASE_YRANGE=1:ORIGIN(2);
IMAGE.values=IMAGE.values(BASE_YRANGE,BASE_XRANGE);
IMAGE.values=im2bw(IMAGE.values,graythresh(IMAGE.values));
imshow(IMAGE.values);

%% DEFINING PLOT BOUNDARIES
```

```
hold on
m1=msgbox('Select the lower-left and upper-right points of the ROI.', ...
          'ROI Selection','modal');
ROI_SET=0;
while isequal(ROI_SET,'Yes, Continue')==0
    CORNERS=zeros(2,2);
    CORNERS(1,:)=ginput(1);
    CORNERS(1,:)=[round(CORNERS(1,1)),round(CORNERS(1,2))];
    d1=plot(CORNERS(1,1),CORNERS(1,2),'.','Color','g','MarkerSize',16);
    CORNERS(2,:)=ginput(1);
    CORNERS(2,:)=[round(CORNERS(2,1)),round(CORNERS(2,2))];
    d2=plot(CORNERS(2,1),CORNERS(2,2),'.','Color','g','MarkerSize',16);
    ROI.top=find(IMAGE.values(1:CORNERS(2,2)+20, ...
            CORNERS(2,1)-20)==0,1,'first');
    ROI.bottom=find(IMAGE.values(CORNERS(1,2)-20:end, ...
              CORNERS(2,1)-20)==0,1,'first')+CORNERS(1,2)-21;
    ROI.left=find(IMAGE.values(CORNERS(1,2)-20, ...
             CORNERS(1,1)-20:CORNERS(1,1)+20)==0,1,'first')+CORNERS(1,1)-21;
    ROI.right=find(IMAGE.values(CORNERS(2,2)+20, ...
              CORNERS(2,1)-20:end)==0,1,'first')+CORNERS(2,1)-21;
    b1=plot([ROI.left,ROI.left,ROI.right,ROI.right,ROI.left], ...
            [ROI.bottom,ROI.top,ROI.top,ROI.bottom,ROI.bottom], ...
            'Color','r','LineWidth',1);
    ROI_SET=questdlg('Is the highlighted ROI correct?', ...
                     'ROI Confirmation','Yes, Continue', ...
                     'No, Retry','No, Cancel','Yes, Continue');
    if isequal(ROI_SET,'No, Cancel')
        uiwait(msgbox('Boundary set aborted by user.','Failure','modal'));
        exit;
    end
    delete([d1,d2,b1]);
end

%% SETTING Y-SCALE
ROI.y_type=listdlg('PromptString','Y-scale type?', ...
                   'SelectionMode','Single', ...
                   'ListString',{'Linear','Power','Log 10', ...
                   'Log e','Custom Log'});
if isempty(ROI.y_type) || isequal(ROI.y_type,'Cancel')
    uiwait(msgbox('Y-scale set aborted by user.','Failure','modal'));
    exit;
elseif isequal(ROI.y_type,2)
    ROI.y_para=inputdlg('Exponent?','Y Power',1,'0.5');
    if isempty(ROI.y_para)
        uiwait(msgbox('Y-scale set aborted by user.','Failure','modal'));
        exit;
    end
    ROI.y_para=str2double(ROI.y_para);
elseif isequal(ROI.y_type,5)
    ROI.y_para=inputdlg('Base?','Y Logarithm',1,'2');
    if isempty(ROI.y_para)
        uiwait(msgbox('Y-scale set aborted by user.','Failure','modal'));
        exit;
    end
    ROI.y_para=str2double(ROI.y_para);
end
m1=msgbox('Select any two Y-axis tick marks (Y1 and Y2).', ...
```

```
          'Y Positions','modal');
Y_SET=0;
while isequal(Y_SET,'Yes, Continue')==0
    [~,y]=ginput(1);
    ROI.y_pos1=round(y);
    y1=plot([1,size(IMAGE.values,2)],[ROI.y_pos1,ROI.y_pos1], ...
            '--','Color','r','LineWidth',1);
    [~,y]=ginput(1);
    ROI.y_pos2=round(y);
    y2=plot([1,size(IMAGE.values,2)],[ROI.y_pos2,ROI.y_pos2], ...
            '--','Color','r','LineWidth',1);
    Y_SET=questdlg('Are the Y-scale marks correct?', ...
                   'Y-scale Confirmation','Yes, Continue','No, Retry', ...
                   'No, Cancel','Yes, Continue');
    if isequal(Y_SET,'No, Cancel')
        uiwait(msgbox('Y-scale set aborted by user.','Failure','modal'));
        exit;
    end
    delete([y1,y2]);
end
y1=plot([1,size(IMAGE.values,2)],[ROI.y_pos1,ROI.y_pos1], ...
        '--','Color','r','LineWidth',1);
y2=plot([1,size(IMAGE.values,2)],[ROI.y_pos2,ROI.y_pos2], ...
        '--','Color','r','LineWidth',1);
ANSWERS=inputdlg({'Y1?','Y2?'},'Y Values',1);
ANSWERS=[str2double(ANSWERS{1}),str2double(ANSWERS{2})];
ROI.y_val1=ANSWERS(1);
ROI.y_val2=ANSWERS(2);

%% SETTING X-SCALE
ROI.x_type=listdlg('PromptString','X-scale type?', ...
                   'SelectionMode','Single', ...
                   'ListString',{'Linear','Power','Log 10', ...
                   'Log e','Custom Log'});
if isempty(ROI.x_type) || isequal(ROI.x_type,'Cancel')
    uiwait(msgbox('X-scale set aborted by user.','Failure','modal'));
    exit;
elseif isequal(ROI.x_type,2)
    ROI.x_para=inputdlg('Exponent?','X Power',1,'0.5');
    if isempty(ROI.x_para)
        uiwait(msgbox('X-scale set aborted by user.','Failure','modal'));
        exit;
    end
    ROI.x_para=str2double(ROI.x_para);
elseif isequal(ROI.x_type,5)
    ROI.x_para=inputdlg('Base?','X Logarithm',1,'2');
    if isempty(ROI.x_para)
        uiwait(msgbox('X-scale set aborted by user.','Failure','modal'));
        exit;
    end
    ROI.x_para=str2double(ROI.x_para);
end
m1=msgbox('Select any two X-axis tick marks (X1 and X2).', ...
          'X Positions','modal');
X_SET=0;
while isequal(X_SET,'Yes, Continue')==0
    [x,~]=ginput(1);
```

```
    ROI.x_pos1=round(x);
    x1=plot([ROI.x_pos1,ROI.x_pos1],[1,size(IMAGE.values,1)], ...
            '--','Color','r','LineWidth',1);
    [x,~]=ginput(1);
    ROI.x_pos2=round(x);
    x2=plot([ROI.x_pos2,ROI.x_pos2],[1,size(IMAGE.values,1)], ...
            '--','Color','r','LineWidth',1);
    X_SET=questdlg('Are the X-scale marks correct?', ...
                   'X-scale Confirmation','Yes, Continue','No, Retry', ...
                   'No, Cancel','Yes, Continue');
    if isequal(X_SET,'No, Cancel')
        uiwait(msgbox('X-scale set aborted by user.','Failure','modal'));
        exit;
    end
    delete([x1,x2]);
end
x1=plot([ROI.x_pos1,ROI.x_pos1],[1,size(IMAGE.values,1)], ...
        '--','Color','r','LineWidth',1);
x2=plot([ROI.x_pos2,ROI.x_pos2],[1,size(IMAGE.values,1)], ...
        '--','Color','r','LineWidth',1);
ANSWERS=inputdlg({'X1?','X2?'},'X Values',1);
ANSWERS=[str2double(ANSWERS{1}),str2double(ANSWERS{2})];
ROI.x_val1=ANSWERS(1);
ROI.x_val2=ANSWERS(2);

%% OPTIONAL - SETTING X CUTOFF FILTERS
X_FILTER_SET=questdlg('OPTIONAL: Limit digitization to a set range of X?',
                      ...
                    'X Filters','Yes','No','Cancel','No');
X_FACTOR=(ROI.x_pos2-ROI.x_pos1)/(ROI.x_val2-ROI.x_val1);
if isequal(X_FILTER_SET,'Yes')
    while isequal(X_FILTER_SET,'Yes, Continue')==0
        PROC.t_low=[];
        PROC.t_high=[];
        ANSWERS=inputdlg({'Optional: Lower X Cutoff?', ...
                          'Optional: Upper X Cutoff?'},'X Filters',1);
        if ~isempty(ANSWERS)
            if ~isempty(ANSWERS{1})
                PROC.t_low=str2double(ANSWERS{1});
                T_POS1=ROI.x_pos1+(PROC.t_low-ROI.x_val1)*X_FACTOR;
                t1=plot([T_POS1,T_POS1],[1,size(IMAGE.values,1)], ...
                        '-','Color','b','LineWidth',1);
            end
            if ~isempty(ANSWERS{2})
                PROC.t_high=str2double(ANSWERS{2});
                T_POS2=ROI.x_pos1+(PROC.t_high-ROI.x_val1)*X_FACTOR;
                t2=plot([T_POS2,T_POS2],[1,size(IMAGE.values,1)], ...
                        '-','Color','b','LineWidth',1);
            end
        end
        X_FILTER_SET=questdlg('Are the cutoff marks correct?', ...
                              'X Cutoff Confirmation','Yes, Continue', ...
                              'No, Retry','No, Cancel','Yes, Continue');
        if isequal(X_FILTER_SET,'No, Cancel')
            uiwait(msgbox('Digitization aborted by
                        user.','Failure','modal'));
            exit;
```

```
        end
        if exist('t1','var')
            delete(t1);
        end
        if exist('t2','var')
            delete(t2);
        end
    end
elseif isequal(X_FILTER_SET,'Cancel')
    uiwait(msgbox('Digitization aborted by user.','Failure','modal'));
    exit;
end

%% OPTIONAL - SETTING DUPLICATE X DATA REDUCTION
PROC.dup_type=listdlg('PromptString','OPTIONAL: Reduce duplicate X data?',
                        ...
                      'SelectionMode','Single', ...
                      'ListString',{'None','Mean','Min','Max'});
if isequal(PROC.dup_type,'Cancel')
    uiwait(msgbox('Digitization aborted by user.','Failure','modal'));
    exit;
end

%% OPTIONAL - SELECTING DIFFRACTION PEAKS
PEAKS_SET=questdlg('OPTIONAL: Run diffraction peak analysis?', ...
                   'Peak Analysis','Yes','No','Cancel','No');
if isequal(PEAKS_SET,'Yes')
    ANSWERS=inputdlg('How many peaks?','Peak Count',1);
    if ~isempty(ANSWERS)
        PEAK_COUNT=str2double(ANSWERS);
        if PEAK_COUNT>0
            m1=msgbox('Click near the maximum of each peak.', ...
                      'Peak Selection','modal');
            while isequal(PEAKS_SET,'Yes, Continue')==0
                [PEAK.p_locs,Y]=ginput(PEAK_COUNT);
                t1=plot(PEAK.p_locs,Y,'vb');
                PEAKS_SET=questdlg('Are the peak markers correct?', ...
                                   'Peak Confirmation','Yes, Continue', ...
                                   'No, Retry','No, Cancel','Yes, Continue');
                delete(t1);
            end
        else
            PEAKS_SET='No';
        end
    else
        PEAKS_SET='No';
    end
    if isequal(PEAKS_SET,'Yes, Continue')
        PEAK.b_para={0,0,'atq'};
        ANSWERS=inputdlg({'Title', ...
                          'Units', ...
                          'Frame for X=0?', ...
                          'Frame to Unit Conversion?'}, ...
                          'X-Axis Parameters',1, ...
                          {'Dose, $\phi$','dpa','0','1'});
        PEAK.x_axis=ANSWERS;
        PEAK.x_axis{3}=str2double(ANSWERS{3});
```

```
        PEAK.x_axis{4}=str2double(ANSWERS{4});
    end
elseif isequal(PEAKS_SET,'Cancel')
    uiwait(msgbox('Digitization aborted by user.','Failure','modal'));
    exit;
end

%% CORRECTING SCALE POSITIONS TO ROI
delete([y1,y2,x1,x2]);
hold off
ROI.y_pos2=ROI.bottom-ROI.y_pos2;
ROI.y_pos1=ROI.bottom-ROI.y_pos1;
ROI.x_pos1=ROI.x_pos1-ROI.left;
ROI.x_pos2=ROI.x_pos2-ROI.left;
ROI.y_span=ROI.y_pos2-ROI.y_pos1;
ROI.x_span=ROI.x_pos2-ROI.x_pos1;
if ~isempty(PEAK.p_locs)
    PEAK.p_locs(:)=PEAK.p_locs(:)-ROI.left;
end

%% LOOPING ANALYSIS
STEPS=length(IMAGE_LIST);
if ~isempty(PEAK.p_locs)
    DATA_OUT=zeros(STEPS,1+PEAK_COUNT);
end
STEP=0/STEPS;
MESSAGE=sprintf('Processing image %d of %d...',1,STEPS);
w1=waitbar(STEP,MESSAGE);
j=0;
for i=1:STEPS
    %% PREPARING NEW IMAGE
    if i>1
        IMAGE.name=strcat(IMAGE.path,IMAGE_LIST(i).name);
        IMAGE.values=imread(IMAGE.name);
        IMAGE.values=IMAGE.values(BASE_YRANGE,BASE_XRANGE);
        IMAGE.values=im2bw(IMAGE.values,graythresh(IMAGE.values));
        imshow(IMAGE.values);
    end

    %% DIGITIZING IMAGE
    [DIG_X,DIG_Y]=mydigitizer(i);

    %% ANALYSING DIFFRACTION PEAKS
    if ~isempty(PEAK.p_locs) && ~isempty(DIG_X)
        j=j+1;
        DATA_OUT(i,1)=str2double(IMAGE.name(end-8:end-4));
        DATA_OUT(i,2:end)=mypeakareas(i,DIG_X,DIG_Y);
    end

    %% UPDATING PROGRESS BAR
    STEP=i/STEPS;
    MESSAGE=sprintf('Processing image %d of %d...',i+1,STEPS);
    waitbar(STEP,w1,MESSAGE);
end
close(w1);

%% REDUCING DUPLICATE ANALYSIS ENTRIES
```

```
STEPS=j;
if ~isempty(PEAK.p_locs)
    DATA_REDUCED=zeros(STEPS,PEAK_COUNT+5);
    i=1;
    j=1;
    k=1;
    while i<=STEPS
        %% COUNTING DUPLICATE PEAK AREA ENTRIES
        MATCHED=1;
        while i+j<=STEPS && MATCHED==1
            for l=1:PEAK_COUNT
                if abs(DATA_OUT(i+j,l+1)/DATA_OUT(i,l+1)-1)>0.001
                    MATCHED=0;
                end
            end
            if MATCHED==1
                j=j+1;
            end
        end

        %% FINDING AVERAGE DATA FOR RESULTING STEP
        DATA_REDUCED(k,1)=min(DATA_OUT(i:i+j-1,1));
        for l=1:PEAK_COUNT
            DATA_REDUCED(k,l+3)=mean(DATA_OUT(i:i+j-1,l+1));
        end

        %% INCREMENTING COUNTERS
        k=k+1;
        i=i+j;
        j=1;
    end

    %% TRIMMING ARRAY SIZE TO CORRECTED MERGED ROWS
    STEPS=k-1;
    DATA_REDUCED=DATA_REDUCED(1:STEPS,:);

    %% CALCULATING X-AXIS VALUES AND STRUCTURE FACTOR RATIOS
                        X_WHERE=2;
    if isequal(PEAK.x_axis{1}(1:4),'Dose')
        X_WHERE=3;
    end
                        for l=1:STEPS
        DATA_REDUCED(l,X_WHERE)=PEAK.x_axis{4}* ...
                                (DATA_REDUCED(l,1)-PEAK.x_axis{3});
        if PEAK_COUNT>3
            DATA_REDUCED(l,end-1)=sqrt(DATA_REDUCED(l,6)/DATA_REDUCED(l,5));
            DATA_REDUCED(l,end)=sqrt((DATA_REDUCED(l,4)+DATA_REDUCED(l,6))/
                        ...
                                    (DATA_REDUCED(l,5)+DATA_REDUCED(l,7)));
        elseif PEAK_COUNT>1
            DATA_REDUCED(l,end-1)=sqrt(DATA_REDUCED(l,PEAK_COUNT+3)/ ...
                                       DATA_REDUCED(l,PEAK_COUNT+2));
        end
                        end

    %% WRITING REDUCED ANALYSIS DATA TO DISK
    CSV_NAME=strcat(IMAGE.name(1:end-10),' - peaks.csv');
```

```
    CSV_DATA=DATA_REDUCED(~any(isnan(DATA_REDUCED),2),:);
    dlmwrite(CSV_NAME,CSV_DATA,'delimiter',',','precision',10);

    CSV_NAME=strcat(IMAGE.name(1:end-10),' - order.csv');
    CSV_DATA=CSV_DATA(:,[X_WHERE,PEAK_COUNT+4:end]);
    dlmwrite(CSV_NAME,CSV_DATA,'delimiter',',','precision',10);

    %% PLOTTING TRACES OF STRUCTURE FACTOR RATIOS
    FIG_NAME=strcat(IMAGE.name(1:end-10),'-frame.png');
    figure('Name',FIG_NAME);
    hold on;
    plot(DATA_REDUCED(:,1),DATA_REDUCED(:,end-1),'-k');
    plot(DATA_REDUCED(:,1),DATA_REDUCED(:,end),'-.k');
    axis([0 inf 0 2]);
    box on;
    grid on;
    xlabel('Frame','Interpreter','latex');
    ylabel('Relative Long-Range Order, $S^{*}$','Interpreter','latex');
    hold off;
    saveas(gcf,FIG_NAME);

    FIG_NAME=strcat(IMAGE.name(1:end-10),'-xunit.png');
    figure('Name',FIG_NAME);
    hold on;
    plot(DATA_REDUCED(:,X_WHERE),DATA_REDUCED(:,end-1),'-k');
    plot(DATA_REDUCED(:,X_WHERE),DATA_REDUCED(:,end),'-.k');
    axis([0 inf 0 2]);
    box on;
    grid on;
    X_LABEL=strcat(PEAK.x_axis{1},' (',PEAK.x_axis{2},')');
    xlabel(X_LABEL,'Interpreter','latex');
    ylabel('Relative Long-Range Order, $S^{*}$','Interpreter','latex');
    hold off;
    saveas(gcf,FIG_NAME);
end

end



%% DIGITIZER FUNCTION
function [X_REDUCED,Y_REDUCED] = mydigitizer(FRAME_I)
% MYDIGITIZER A function for digitizing single curves.

global IMAGE;
global ROI;
global PROC;
global PEAK;

%% PROCESSING ROI
ACTUAL_IMAGE = IMAGE.values((ROI.top+1):(ROI.bottom-1), ...
                            (ROI.left+1):(ROI.right-1));
% MASK=[1,1,1;1,0,1;1,1,1];
% FILTERED_IMAGE=ordfilt2(ACTUAL_IMAGE,3,MASK);
% PEAKS=ACTUAL_IMAGE > FILTERED_IMAGE;
% imshow(PEAKS);
```

```
%% REMOVING DISCONNECTED COMPONENTS
CC=bwconncomp(~ACTUAL_IMAGE,8);
COMP_SIZES=cellfun(@numel,CC.PixelIdxList);
MAX_COMP=max(COMP_SIZES);
COMP_THRES=0.10*MAX_COMP;
for i=1:length(COMP_SIZES)
    if COMP_SIZES(i)<COMP_THRES
        ACTUAL_IMAGE(CC.PixelIdxList{i})=256;
    end
end
% imshow(ACTUAL_IMAGE);

%% EXTRACTING RAW (X,Y)
[X_RAW,Y_RAW,~]=find(fliplr(ACTUAL_IMAGE')==0);
[X_RAW,SORT_INDEX]=sort(X_RAW,'ascend');
Y_RAW=Y_RAW(SORT_INDEX);

%% SCALING Y DATA
Y_SCALED=zeros(size(Y_RAW));
if isequal(ROI.y_type,1)
    Y_dPIXEL=(ROI.y_val2-ROI.y_val1)/ROI.y_span;
    Y_SCALED(:)=ROI.y_val1+Y_dPIXEL*(Y_RAW(:)-ROI.y_pos1);
elseif isequal(ROI.y_type,2)
    Y_dPIXEL=(ROI.y_val2^(1/ROI.y_para)-
                        ROI.y_val1^(1/ROI.y_para))/ROI.y_span;
    Y_POW_REF=ROI.y_val1^(1/ROI.y_para);
    Y_SCALED(:)=(Y_POW_REF+Y_dPIXEL*(Y_RAW(:)-ROI.y_pos1)).^(ROI.y_para);
elseif isequal(ROI.y_type,3)
    Y_dPIXEL=log10(ROI.y_val2/ROI.y_val1)/ROI.y_span;
    Y_SCALED(:)=ROI.y_val1*10.^(Y_dPIXEL*(Y_RAW(:)-ROI.y_pos1));
elseif isequal(ROI.y_type,4)
    Y_dPIXEL=log(ROI.y_val2/ROI.y_val1)/ROI.y_span;
    Y_SCALED(:)=ROI.y_val1*exp(1).^(Y_dPIXEL*(Y_RAW(:)-ROI.y_pos1));
elseif isequal(ROI.y_type,5)
    Y_dPIXEL=(log(ROI.y_val2/ROI.y_val1)/log(ROI.y_para))/ROI.y_span;
    Y_SCALED(:)=ROI.y_val1*ROI.y_para.^(Y_dPIXEL*(Y_RAW(:)-ROI.y_pos1));
end

%% SCALING X DATA
X_SCALED=zeros(size(X_RAW));
if FRAME_I==1 && ~isempty(PEAK.p_locs)
    SCALE_LOCS=1;
else
    SCALE_LOCS=0;
end
if isequal(ROI.x_type,1)
    X_dPIXEL=(ROI.x_val2-ROI.x_val1)/ROI.x_span;
    X_SCALED(:)=ROI.x_val1+X_dPIXEL*(X_RAW(:)-ROI.x_pos1);
    if SCALE_LOCS==1
        PEAK.p_locs(:)=ROI.x_val1+X_dPIXEL* ...
                       (PEAK.p_locs(:)-ROI.x_pos1);
    end
elseif isequal(ROI.x_type,2)
    X_dPIXEL=(ROI.x_val2^(1/ROI.x_para)-
                        ROI.x_val1^(1/ROI.x_para))/ROI.x_span;
    X_POW_REF=ROI.x_val1^(1/ROI.x_para);
    X_SCALED(:)=(X_POW_REF+X_dPIXEL*(X_RAW(:)-ROI.x_pos1)).^(ROI.x_para);
```

```
    if SCALE_LOCS==1
        PEAK.p_locs(:)=(X_POW_REF+X_dPIXEL* ...
                        (PEAK.p_locs(:)-ROI.x_pos1)).^(ROI.x_para);
    end
elseif isequal(ROI.x_type,3)
    X_dPIXEL=log10(ROI.x_val2/ROI.x_val1)/ROI.x_span;
    X_SCALED(:)=ROI.x_val1*10.^(X_dPIXEL*(X_RAW(:)-ROI.x_pos1));
    if SCALE_LOCS==1
        PEAK.p_locs(:)=ROI.x_val1*10.^ ...
                        (X_dPIXEL*(PEAK.p_locs(:)-ROI.x_pos1));
    end
elseif isequal(ROI.x_type,4)
    X_dPIXEL=log(ROI.x_val2/ROI.x_val1)/ROI.x_span;
    X_SCALED(:)=ROI.x_val1*exp(1).^(X_dPIXEL*(X_RAW(:)-ROI.x_pos1));
    if SCALE_LOCS==1
        PEAK.p_locs(:)=ROI.x_val1*exp(1).^ ...
                        (X_dPIXEL*(PEAK.p_locs(:)-ROI.x_pos1));
    end
elseif isequal(ROI.x_type,5)
    X_dPIXEL=(log(ROI.x_val2/ROI.x_val1)/log(ROI.x_para))/ROI.x_span;
    X_SCALED(:)=ROI.x_val1*ROI.x_para.^(X_dPIXEL*(X_RAW(:)-ROI.x_pos1));
    if SCALE_LOCS==1
        PEAK.p_locs(:)=ROI.x_val1*ROI.x_para.^ ...
                        (X_dPIXEL*(PEAK.p_locs(:)-ROI.x_pos1));
    end
end

%% FILTERING DATA
X_FILTERED=X_SCALED;
Y_FILTERED=Y_SCALED;
if ~isempty(PROC.t_low)
    Y_FILTERED=Y_FILTERED(X_FILTERED>PROC.t_low);
    X_FILTERED=X_FILTERED(X_FILTERED>PROC.t_low);
end
if ~isempty(PROC.t_high)
    Y_FILTERED=Y_FILTERED(X_FILTERED<PROC.t_high);
    X_FILTERED=X_FILTERED(X_FILTERED<PROC.t_high);
end

%% REDUCING DATA
if isequal(PROC.dup_type,1)
    X_REDUCED=X_FILTERED;
    Y_REDUCED=Y_FILTERED;
else
    X_REDUCED=zeros(length(X_FILTERED));
    Y_REDUCED=zeros(length(Y_FILTERED));
    i=1;
    j=1;
    k=1;
    while i<=length(X_FILTERED)
        X_REDUCED(k)=X_FILTERED(i);
        if isequal(PROC.dup_type,2)
            Y_REDUCED(k)=mean(Y_FILTERED(X_FILTERED==X_FILTERED(i)));
        elseif isequal(PROC.dup_type,3)
            Y_REDUCED(k)=min(Y_FILTERED(X_FILTERED==X_FILTERED(i)));
        elseif isequal(PROC.dup_type,4)
            Y_REDUCED(k)=max(Y_FILTERED(X_FILTERED==X_FILTERED(i)));
```

```
        end
        k=k+1;
        while i+j<=length(X_FILTERED) && X_FILTERED(i)==X_FILTERED(i+j)
            j=j+1;
        end
        i=i+j;
        j=1;
    end
    X_REDUCED=X_REDUCED(1:k-1)';
    Y_REDUCED=Y_REDUCED(1:k-1)';
end

%% WRITING FINAL DATA TO DISK
CSV_NAME=strcat(IMAGE.name(1:end-4),'.csv');
CSV_DATA=cat(2,X_REDUCED,Y_REDUCED);
dlmwrite(CSV_NAME,CSV_DATA,'delimiter',',','precision',10);

end


%% PEAK INTEGRATION FUNCTION
function AREAS = mypeakareas(FRAME_I,X,Y)
% MYPEAKAREAS A function for integrating diffraction line scans.
% Requires backcor.m background fitting script by Vincent Mazet.
% http://www.mathworks.com/matlabcentral/fileexchange/27429-background-
      correction

global PEAK;

%% SETTING UP
PEAK_COUNT=length(PEAK.p_locs);
PEAKS=zeros(size(PEAK.p_locs));
for l=1:PEAK_COUNT
    PTEMP=find(X<PEAK.p_locs(l),1,'last');
    if ~isempty(PTEMP)
        PEAKS(l)=PTEMP;
    else
        PEAKS(l)=0;
    end
end
PEAK_WINDOW=(PEAK.p_locs(end)-PEAK.p_locs(1))/(6.0*(PEAK_COUNT-1));

%% FITTING AND SUBTRACTING BACKGROUND
if FRAME_I==1
    [Z,~,~,ORD,S,FCT]=backcor(X,Y);
    PEAK.b_para={ORD,S,FCT};
else
    ORD=PEAK.b_para{1};
    S=PEAK.b_para{2};
    FCT=PEAK.b_para{3};
    [Z,~,~,ORD,S,FCT]=backcor(X,Y,ORD,S,FCT);
    PEAK.b_para={ORD,S,FCT};
end

CSV_NAME=strcat('D:\storage\temp\raw.csv');
CSV_DATA=cat(2,X,Y);
dlmwrite(CSV_NAME,CSV_DATA,'delimiter',',','precision',10);
```

```
Y=Y-Z;
plot(X,Y,'-k');
axis([0 inf 0 inf]);
% set(gca,'yscale','log');

CSV_NAME=strcat('D:\storage\temp\sub.csv');
CSV_DATA=cat(2,X,Y);
dlmwrite(CSV_NAME,CSV_DATA,'delimiter',',','precision',10);

%% INTEGRATING PEAKS
AREAS=zeros(size(PEAK.p_locs));
for l=1:PEAK_COUNT
    if PEAKS(l)~=0
        IDX=abs(X-PEAK.p_locs(l))<PEAK_WINDOW;
        if any(Y(IDX)./Z(IDX)>1)
            AREAS(l)=trapz(X(IDX),Y(IDX));
        else
            AREAS(l)=NaN;
        end
    else
        AREAS(l)=NaN;
    end
end
disp(AREAS)

end
```